ACS APPLIED MATERIALS & INTERFACES

www.acsami.org

Review

Recent Advancements and Challenges for Low-Toxicity Perovskite Materials

Tao Zhu, Yongrui Yang, and Xiong Gong*

Cite This: *ACS Appl. Mater. Interfaces* 2020, 12, 26776–26811

Read Online

ACCESS | Metrics & More | Article Recommendations

ABSTRACT: Lead-based organic–inorganic hybrid perovskite materials have been developed for advanced optoelectronic applications. However, the toxicity of lead and the chemical instability of lead-based perovskite materials have so far been demonstrated to be an overwhelming challenge. The discovery of perovskite materials based on low-toxicity elements, such as Sn, Bi, Sb, Ge, and Cu, with superior optoelectronic properties provides alternative approaches to realize high-performance perovskite optoelectronics. In this review, recent advances in the aspects of low-toxicity perovskite solar cells, photodetectors, light-emitting diodes, and thermoelectric devices are highlighted. The antioxidation stability of metal cation and the crystallization process of the low-toxicity perovskite materials are discussed. In the last part, the outlook toward addressing various issues requiring further attention in the development of low-toxicity perovskite materials is outlined.

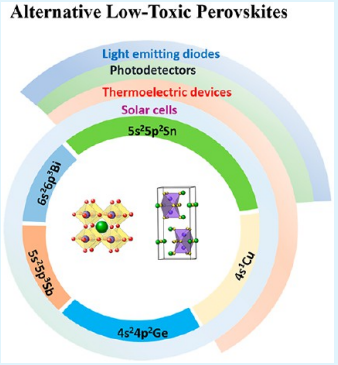

KEYWORDS: *low-toxicity hybrid perovskites, solar cells, photodetectors, light emitting diodes, thermoelectric devices*

1. INTRODUCTION

Perovskite materials with a chemical formula of ABX_3, where A is $CH_3NH_3^{1+}$ (MA^{1+}), $NH_2CH{=}NH_2^{1+}$ (FA^{1+}), or Cs^+; B is Pb^{2+} or Sn^{2+}; and X is Cl^-, Br^-, I^- or their combination, respectively, have been developed for advanced optoelectronic applications because of their superior optoelectronic properties, including suitable and tunable bandgap (1.2–2.3 eV), excellent light absorption coefficient (~1×10^5 cm^{-1}), high photoluminescence quantum yield (PLQY), narrow-band emission, relatively small absorption length, long diffusion length, and low-cost solution processability.[1−14] All these features enable perovskite materials to be good candidates for the applications in solar cells, photodetectors (PDs), light-emitting diodes (LED), and thermal thermoelectric devices.[7,8,15−20] Scheme 1a outlines lead (Pb)-based perovskite materials for the applications in the optoelectronic and thermoelectric devices.

In the past decade, Pb-based perovskite solar cells (PSCs) with power conversion efficiencies (PCEs) boosted from 3.80 to 25.2% and Pb-based perovskite photodetectors (PPDs) with photodetectivities of 1×10^{15} Jones (1 Jones = 1 cm $Hz^{1/2}$ W^{-1}) have been reported.[7,8,15−17] Moreover, an ultrahigh PLQY of 80% and high Seebeck coefficient value of ~1000 μV/K, were reported from Pb-based perovskite single crystals and Pb-based perovskite quantum dots, respectively.[18,19] Despite all these attractive applications in optoelectronic and thermoelectric devices, the toxicity of Pb^{2+} could generate environmental problems during fabrication, utilization, and further disposal,[21] which is considered to be one of bottlenecks for their practice applications.

To address the toxicity of Pb^{2+}, researchers have used environmentally friendly elements, such as Ge^{2+} and Sn^{2+} from group 14 and Bi^{3+} and Sb^{3+} from group 15 of the periodic table, as a substitute for Pb^{2+}, as they have a similar inactive outer-shell s orbit, which is the key to the unique photovoltaic properties of perovskite materials.[22,23] Scheme 1b outlines Pb-free perovskite materials for the applications in the optoelectronic and thermoelectric devices. Among them, Sn-based perovskites exhibit decent optoelectronic properties and show a relatively satisfactory device performance.[24,25] However, the oxidation of Sn^{2+} to Sn^{4+} was a readily spontaneous process, leading to a self-doping processing in the crystals, consequently resulting in poor device performance.[24,26] Many approaches have been attempted to enhance the stability of Sn-based PSCs.[27−30] So far, 9% PCE was observed from PSCs by pure Sn-based perovskite materials.[29]

Bi, Ge, and Sb-based perovskite materials possess superior optical properties, which is essential for photovoltaic applications. Ge is an environmentally free element. It was

Received: February 10, 2020
Accepted: May 20, 2020
Published: May 20, 2020

https://dx.doi.org/10.1021/acsami.0c02575
ACS Appl. Mater. Interfaces 2020, 12, 26776–26811

Scheme 1. Potential Optoelectronic and Thermoelectric Applications Based on (A) Lead Based Perovskite Materials and (b) Low-Toxicity Perovskite Materials

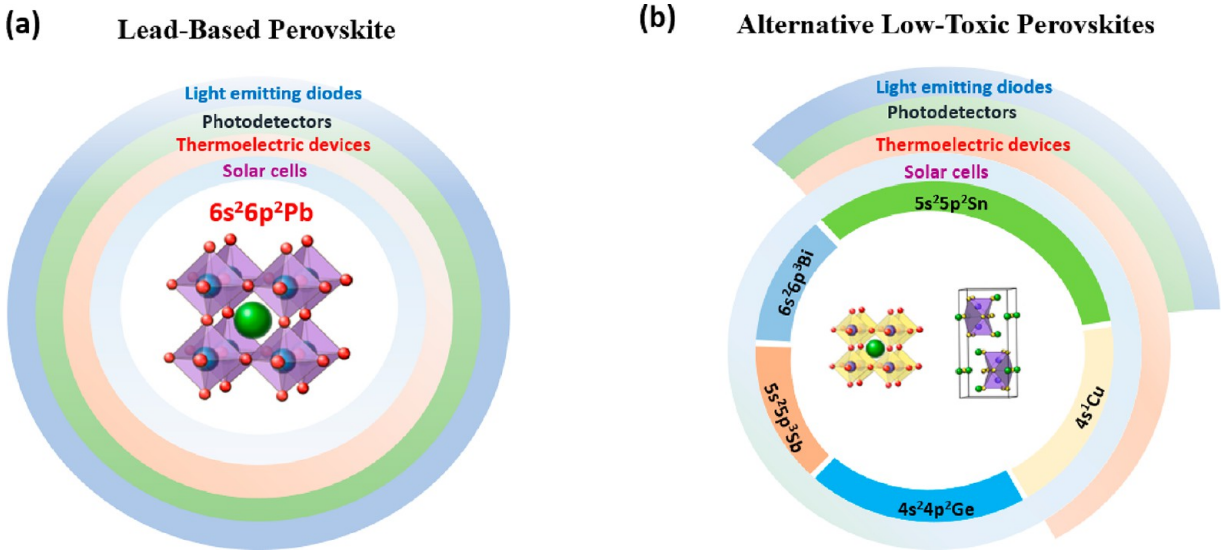

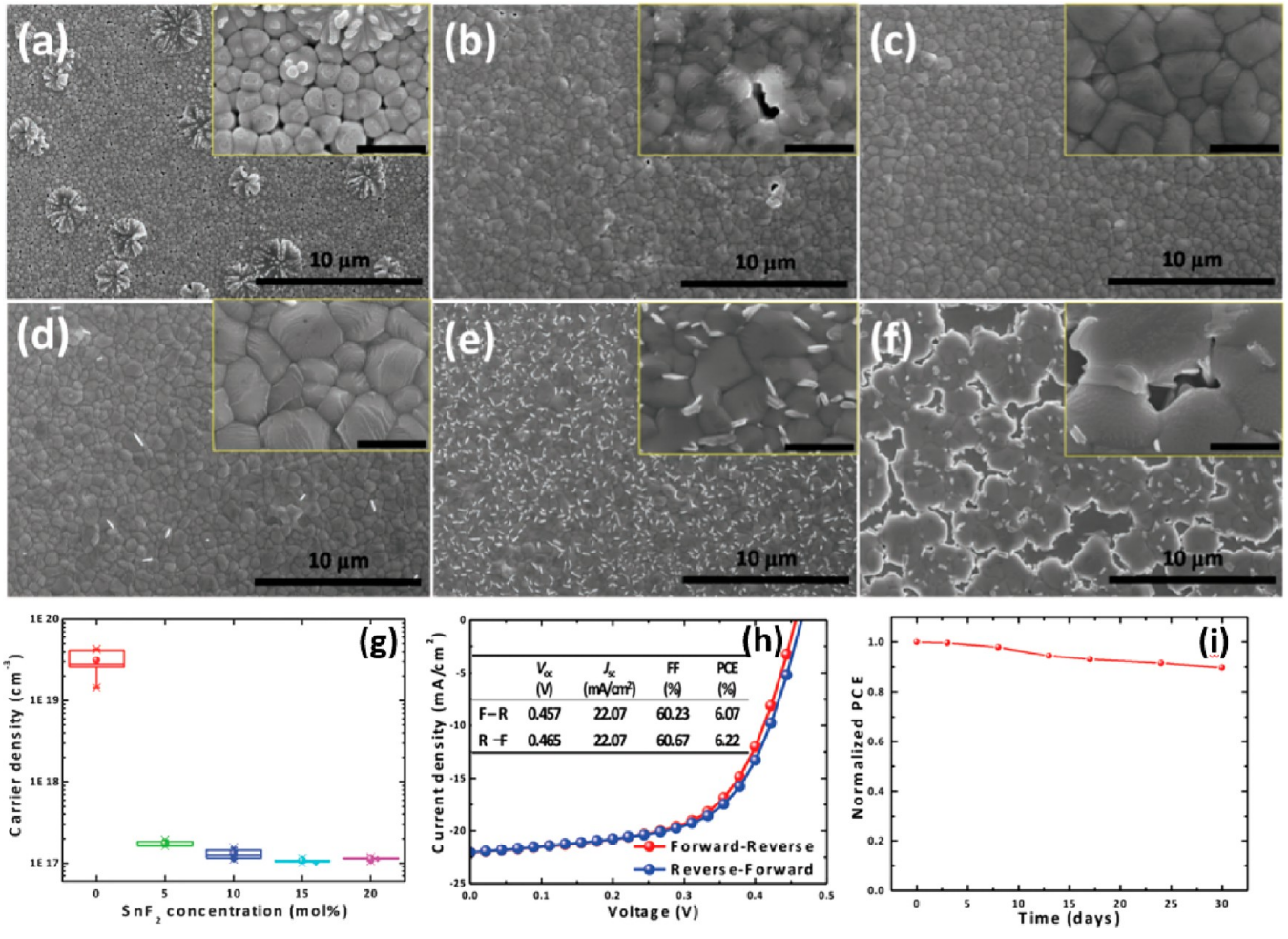

Figure 1. SEM images of $FASnI_3$ perovskite films on PEDOT:PSS with varying concentration of SnF_2: (a) 0, (b) 5, (c) 10, (d) 15, (e) 20, and (f) 30 mol %. Scale bar in all images is 10 μm. The inset in each figure shows their corresponding SEM image at high magnification. The scale bar in the inset is 1 μm. (g) Carrier density versus SnF_2 molar concentration in $FASnI_3$ PVSCs. (h) $J-V$ characteristics under 100 mW cm^{-2} AM1.5G illumination under reverse and forward voltage scans. (i) Stability of encapsulated cell with 10 mol % SnF_2 additives measured in ambient. Reproduced with permission from ref 27. Copyright 2016 Wiley.

https://dx.doi.org/10.1021/acsami.0c02575
ACS Appl. Mater. Interfaces 2020, 12, 26776−26811

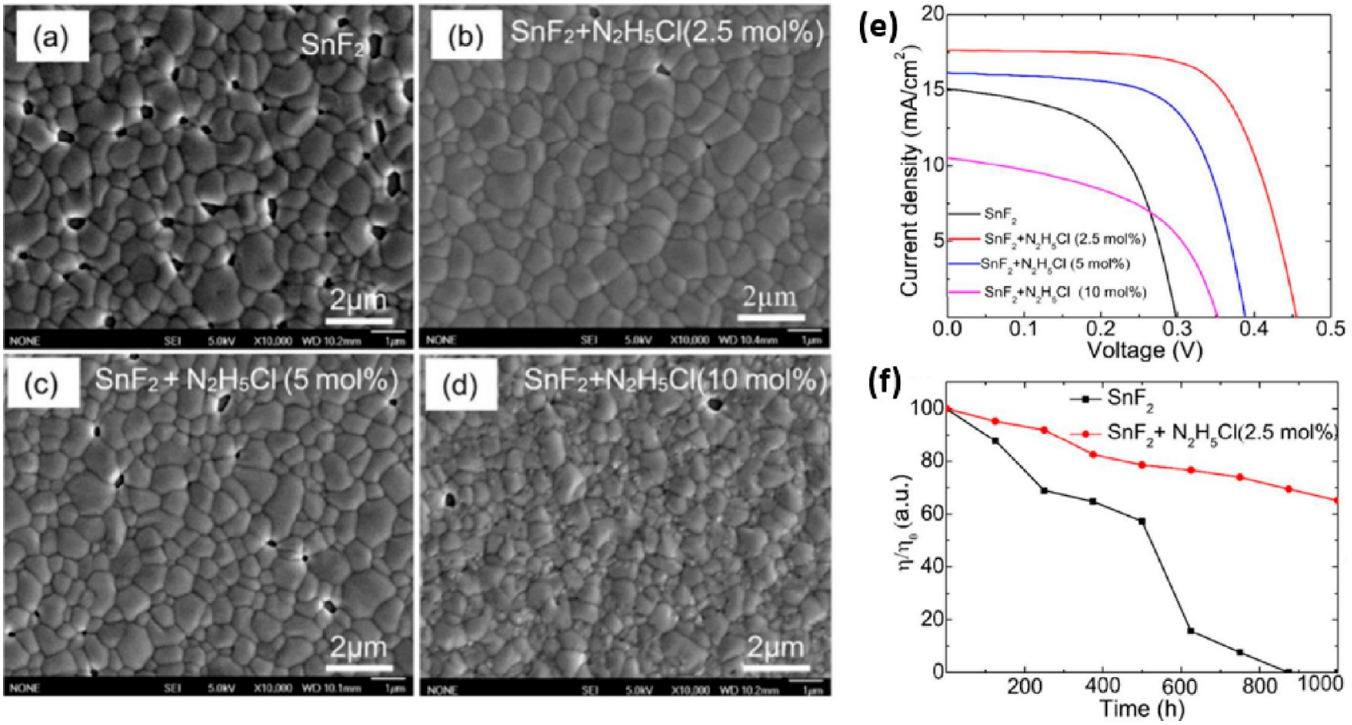

Figure 2. SEM images of $FASnI_3$ films: (a) SnF_2, (b) SnF_2 + 2.5 mol % N_2H_5Cl, (c) SnF_2 + 5 mol % N_2H_5Cl, and (d) SnF_2 + 10 mol % of N_2H_5Cl, (e) $J-V$ curves of SnF_2 and SnF_2 + various concentrations of N_2H_5Cl-based PSCs, and (f) shelf life stability of SnF_2 and SnF_2 + 2.5 mol % N_2H_5Cl added $FASnI_3$-based PSCs. Reproduced with permission from ref 62. Copyright 2018 American Chemical Society.

reported that Ge-based perovskites possess large bandgaps, which could ensure Ge-based PSCs with a high open-circuit voltage (V_{OC}).[31] Sb is less toxic than that of Pb,[32−35] but the photovoltaic properties of Sb-based perovskite materials were rarely reported.[35] Bi is a toxic-free element and Bi^{3+} is isoelectronic with Pb^{2+}. It was expected that Bi-based perovskites with tunable bandgaps are probably more suitable for tandem solar cells.[36−39] In addition to Sn and Bi, Sb and Ge have emerged as other alternatives. Transition metal ions such as Cu^{2+} also exhibit potential for making low-toxicity PSCs.[40,41]

Near-infrared (NIR) PDs by Pb (or Sn)-based perovskites incorporated with other materials and/or Pb (Sn)-based perovskites with tunable bandgaps have been reported.[42−45] In addition, Sn-based perovskite materials exhibit good electrical conductivity, indicating it is a promising candidate for thermoelectric application.[46]

Low-toxicity elements Sn^{2+}, Bi^{3+}, and Sb^{3+}-based perovskites have been alternatively developed as LED materials because of their low toxicity, excellent optical properties, and high PLQY.[47−50] Specifically, all inorganic halide perovskite nanocrystals draw more attention as LED materials because all inorganic halide perovskite materials possess a better stability in common working conditions with light, compared to organic halide perovskite materials.[51] Additionally, compared to bulk perovskite materials, the defect states of perovskite nanocrystals are trap free within the bandgap,[52] resulting in a high PLQY in all-inorganic halide perovskite nanocrystals.

Therefore, it is of great important to overview the low-toxicity perovskite materials and their applications in the optoelectronic and thermoelectric devices. In this short review, we present the photovoltaic (solar cells and PDs), LEDs, and potential thermoelectric studies. We first overview PSCs by low-toxicity perovskite materials in the past decade and then introduce recent progresses of NIR PDs by toxic perovskite materials. In the fourth section, we discuss the low-toxicity perovskite materials in LEDs applications. In the fifth section, Sn-based perovskite materials for approaching thermoelectric devices are reviewed. In the last section, the strategies for further development of low-toxicity perovskite materials are highlighted.

2. LOW-TOXICITY PEROVSKITE MATERIALS FOR PEROVSKITE SOLAR CELLS

2.1. Sn-Based Perovskite Solar Cells. *2.1.1. Additive Engineering.* The main restriction for the application of Sn-based perovskite materials for PSCs is its instability. Sn^{2+} can be easily oxidized to Sn^{4+} as Sn-based perovskites exposed in ambient air. Such an oxidization process was termed as the self-doping process as Sn^{4+} here plays a role as a p-type dopant.[53] Because of the oxidization process, both the charge carrier density and the electrical conductivity of Sn-based perovskite materials were increased, but its semiconductor properties were sacrificed, resulting in poor device performance of PSCs.[54,55] In 2016, Liao et al.[27] reported Sn-based PSCs by $FASnI_3$ thin film processed from $FASnI_3$ precursor solution with SnF_2 as an additive to suppress the oxidation of Sn^{2+}. As indicated in Figure 1a, many pinholes appeared on the surface of perovskite thin film, which was processed from a precursor solution with a smaller amount of SnF_2, and the surface could not be covered underneath the PEDOT:PSS layer. However, some SnF_2 residuum would remain on the top of the perovskite layer if using more than 10 mol % SnF_2 as additives (Figure 1d), leading to an inconsecutive and island-like thin film. Moreover, the addition of SnF_2 substantially decreased the charge carrier density of $FASnI_3$ thin film by approximately two orders magnitude (from 1×10^{19} to 1×10^{17}), resulting in poor device performance of PSCs (Figure 1g). As shown in Figure 1h, a PCE of 6.22% was observed from PSC with an inverted device structure of ITO/PEDOT:PSS/$FASnI_3$/C60/BCP/Ag, where ITO is indium tin oxide, PEDOT:PSS is poly(3,4-ethylenedioxythiophene):polystyrenesulfonate, BCP is 2,9-dimethyl-4,7-dipheny-l1,10-phenanthroline, and Ag is silver, respec-

https://dx.doi.org/10.1021/acsami.0c02575
ACS Appl. Mater. Interfaces 2020, 12, 26776−26811

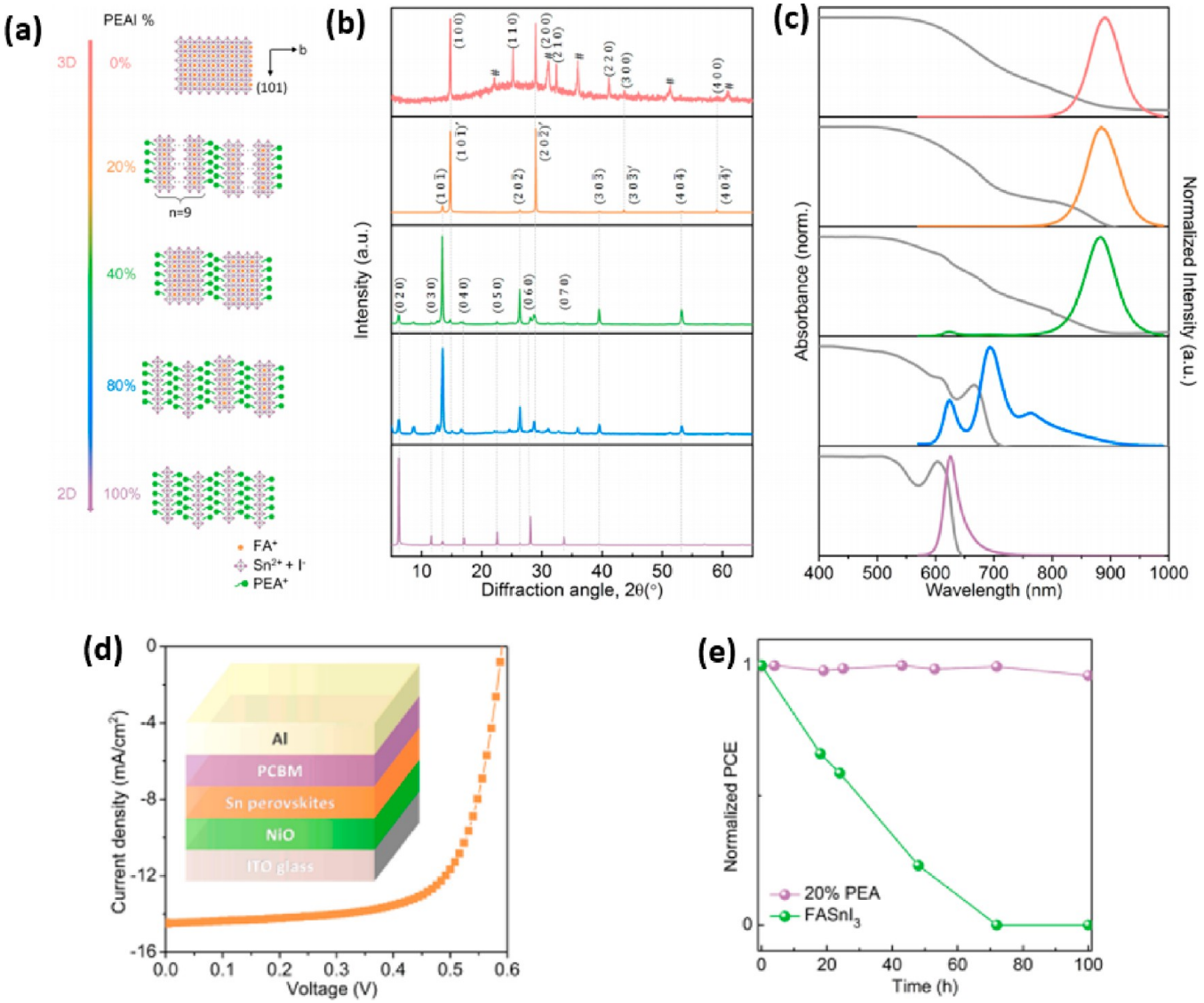

Figure 3. (a) Schematic structures of $FASnI_3$ and $(PEA)_2SnI_4$, and mixed FA-PEA Sn perovskites. The PEA% labels indicate the mole percentage of PEA as a fraction the total organic cation composition; the labels also apply to panels b and c. Letter *n* denotes the average layers of Sn iodide octahedra in nanolayers. (b) XRD spectra for Sn perovskite films with different PEA ratios. The peaks of $FASnI_3$ were indexed in a quasi-cubic system, whereas peaks of other films are indexed in an orthorhombic system. Miller indices followed by a "prime" symbol, like $(10\bar{1})'$, represent lattice planes in crystal domains in which the in-plane lattice parameters approach bulk perovskite ($n > 5$), whereas lattice planes in other grains are indexed without an extra symbol, like $(10\bar{1})$. A # indicates the diffraction peaks of ITO. (c) Normalized absorbance (gray curves, left axis) and photoluminescence (colorful curves, right axis) spectra of the investigated thin films. (d) Device architecture and current density–voltage (J–V) characteristics of the highest performance device. (e) Normalized PCE of the unencapsulated device based on $FASnI_3$ and 20% PEA-doped perovskite film stored in a glovebox for over 100 h. Reproduced with permission from ref 68. Copyright 2017 American Chemical Society.

Table 1. Figures of Merit for Devices with 3D Sn Perovskite and 2D/3D Sn Perovskite Layers under One Sun Condition[a]

device	J_{SC} (mA cm^{-2})	V_{OC} (V)	fill factor (%)	PCE (%)
3D	22.5	0.458	58	6.0
2D/3D	24.1	0.525	71	9.0

[a]Reproduced with permission from ref 29. Copyright 2018 Wiley.

tively. It was found that Sn-based PSCs treated by 10 mol % SnF_2 only showed 5.86% drop in the efficiency after 2700 s, which was shown in Figure 1i. These results indicated that small amounts of SnF_2 in Sn-based perovskite materials are favorable for improving device stability.

Because the pinholes on the surface of perovskite thin film with the addition of SnF_2, the rapid reaction rate of SnI_2 with MAI (or FAI) induce a much faster crystals grow than the formation of the crystal nucleus, resulting in a poor film morphology of perovskite layer.[56] To address these problems, the amount of metal halide needs to be controlled, i.e., using a Lewis acid to adjust the expanded volume of the precursory film during the first step and to tune the rapid reaction rate during the second step.[57,58]

In short, SnF_2 as a convincing and efficient processing additive has been widely used in Sn-based PSCs to suppress the oxidation of Sn^{2+} and enhance the device performance of PSCs.[27] However, excess SnF_2 will remain on the surface of the $FASnI_3$ photoactive layer and induce discontinuity of $FASnI_3$ thin film. Therefore, the amount of SnF_2 will be limited, as it was applied for the fabrication of Sn-based PSCs. Consequently, it is urgent to explore other approaches to increase the stability of Sn-based PSCs.

https://dx.doi.org/10.1021/acsami.0c02575
ACS Appl. Mater. Interfaces 2020, 12, 26776–26811

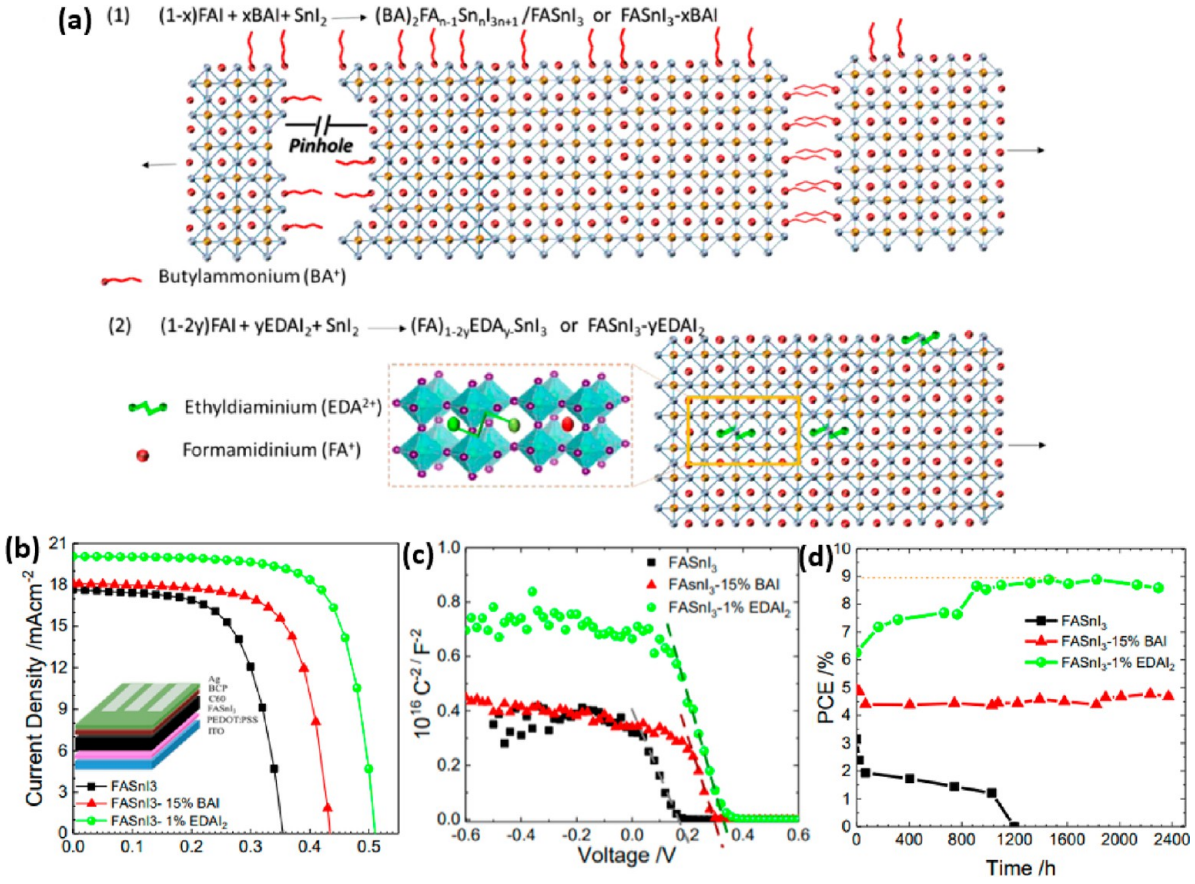

Figure 4. (a) Schematic representations of perovskite crystals in the presence of (1) for BAI and (2) for $EDAI_2$ additives. (b) $J-V$ curve, (c) Mott–Schottky plots, and (d) stability test of PSCs based on $FASnI_3$, $FASnI_3$-15%BAI, and $FASnI_3$-1% $EDAI_2$. Reproduced with permission from ref 56. Copyright 2018 Royal Society of Chemistry.

Other additives for preventing the effect of oxygen and improving the quality of perovskite thin films have also been studied in recent years.[59−63] For instance, hydrazine (N_2H_4) was used as a reducing agent in Sn-based PSCs, as N_2H_4 vapor can keep Sn^{2+} from being oxidized during perovskite crystallization.[59] To further optimize PSCs performance, Kayesh et al.[62] utilized hydrazinium chloride (N_2H_5Cl) as a processing additive with SnF_2 in the precursor solution for preparation of $FASnI_3$ thin films by a one-step method. N_2H_5Cl has advantages over both N_2H_4 and chlorine salts, which can effectively passivate the generation of Sn^{4+} and form intermediary acting as cores and promoting the growth of large crystal grains. The SEM images of $FASnI_3$ thin films are shown in Figure 2a–d. It was clear that 2.5 mol % N_2H_5Cl in the precursor solution was the most suitable concentration for approaching perovskite thin film with the largest grain size. As indicated in Figure 2e, a PCE up to 5.4% with nearly hysteresis-free characteristics from PSCs with an inverted device architecture was reported.[62] In addition, the PCE of PSCs with 2.5 mol % N_2H_5Cl maintained ∼65% of its initial PCE after 1000 h, but the PCE of PSCs with SnF_2 only degraded quickly (Figure 2f). Their work provided a facile way (coadditive) for achieving high-stability Sn-based PSCs.

2.1.2. 2D/3D Mixed Perovskites. Inspired by 2D Pb-based perovskites, researchers started to conduct 2D Sn-based perovskites to address stability issue.[64−67] Liao et al.[68] added phenylethylammonium iodide (PEAI) into the $FASnI_3$ precursor solution to form low dimensional Sn-based perovskites, $(PEA)_2(FA)_{n-1}Sn_nI_{3n+1}$, where n was the amount of $FASnI_3$ layers between PEA bilayers in the unit. In this work, they synthesized perovskites with different n values by optimizing the ratio of PEAI from 0 to 100%. Figure 3 presents the XRD spectra of $(PEA)_2(FA)_{n-1}Sn_nI_{3n+1}$ with different concentrations of PEA, proving the structural transformation from 3D Sn-based perovskites to pure 2D Sn-based perovskite along with increased the PEA ratio. The formation of low dimensional Sn-based perovskites could also be verified by a blue-shifted photoluminescence (PL) spectrum. Moreover, a grazing-incidence wide-angle X-ray scattering (GIWAXS) patterns indicated the formation of the better orientation of crystal grains in 2D Sn-based perovskites. Compared to 3D Sn-based perovskites, low-dimensional perovskites are less sensitive to moisture and oxygen.[69−73] In work reported by Liao,[68] the decomposition enthalpy was calculated. It was found out that the smaller the n value was, the better oxidation resistance the perovskites had. As a result, less Sn^{2+} would be oxidized to Sn^{4+} and the charge carrier concentration was lower than that of 3D Sn perovskites, which was beneficial for the suppression of charge carrier recombination in PSCs., They also found that Sn-based PSCs with a device structure of ITO/NiO_x/Sn-perovskite/PCBM/Al, where Sn-based perovskite with 20% PEA, exhibited a PCE of 5.94%, a V_{OC} of 0.59 V, a J_{SC} of 14.44 mA·cm^{-2} and a FF of 69%, and remained about 96% of original PCE value after 100 h operation as shown in Figures 3d, e.

With a similar strategy, Shao et al.[29] employed PEAI as a processing additive in Sn-based perovskite materials. A PCE of 9% was obtained from PSCs with a planar heterojunction structure, where the photoactive layer was composited of 0.08 M of 2D Sn-based perovskites mixed with 0.92 M of 3D Sn-based perovskites. The detailed device performance parameters were summarized in Table 1. The GIWAXS studies indicated that one-step processed 2D/3D perovskite materials possessed a higher crystallinity and well-ordered orientation of crystal grains. The studies of time-resolved PL and independence of V_{OC} to light intensity measurements demonstrated that superior device performance was majorly attributed to longer charge carrier lifetime and less trap-assisted charge recombination.

Jokar et al.[56] employed organic cations, ethylene diammonium diiodide ($EDAI_2$), and butylammonium iodide (BAI) to passivate the surface defects for approaching uniform surface across perovskite thin

https://dx.doi.org/10.1021/acsami.0c02575
ACS Appl. Mater. Interfaces 2020, 12, 26776−26811

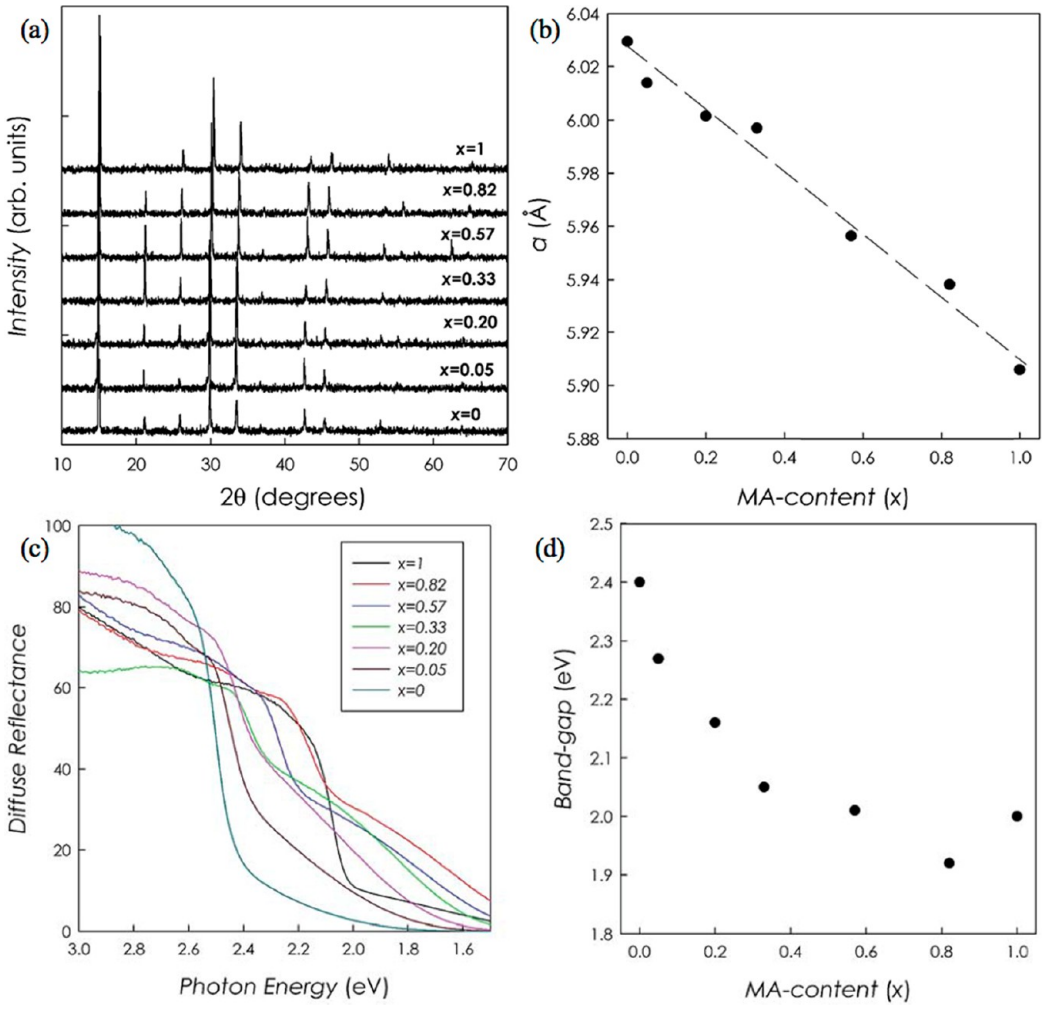

Figure 5. (a) XRD patterns for the samples of the $FA_{1-x}MA_xSnBr_3$ system. The patterns are vertically shifted to clarify viewing; (b) cubic lattice parameter; (c) diffuse reflectance spectra of the $FA_{1-x}MA_xSnBr_3$ solid solution; (d) energy gap trend as a function of *x*. Reproduced with permission from ref 78. Copyright 2017 Royal Society of Chemistry.

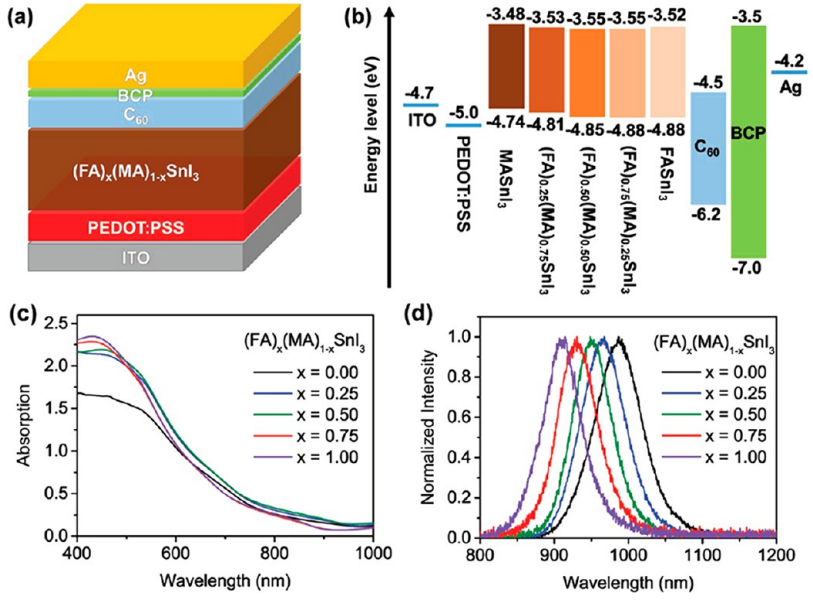

Figure 6. (a) Schematic illustration of the device structure; (b) band alignment diagram; (c) absorption spectra of the different perovskite films on quartz substrates; (d) normalized emissions of the different perovskite films on quartz substrates. Reproduced with permission from ref 81. Copyright 2017 Wiley.

https://dx.doi.org/10.1021/acsami.0c02575
ACS Appl. Mater. Interfaces 2020, 12, 26776−26811

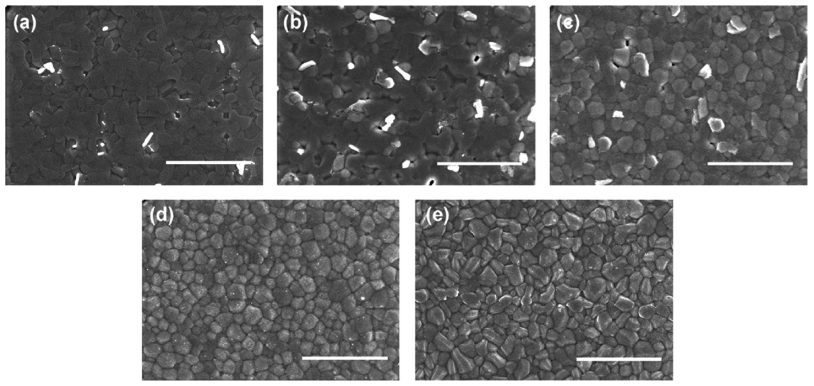

Figure 7. SEM images of a) $MASnI_3$, (b) $FA_{0.25}MA_{0.75}SnI_3$, (c) $FA_{0.50}MA_{0.50}SnI_3$, (d) $FA_{0.75}MA_{0.25}SnI_3$, and (e) $FASnI_3$ films deposited on ITO/PEDOT:PSS substrates (scale bar: 3.0 μm). Reproduced with permission from ref 81. Copyright 2017 Wiley.

Table 2. XPS Intensity of Sn^{4+} as a Function of Ge Content[a]

sample	normalized intensity of Sn^{4+}
x = 0	1.00
x = 0.05	0.44
x = 0.10	0.41
x = 0.20	0.35

[a]Reproduced from ref 86. Copyright 2018 American Chemical Society.

films. As shown in Figure 4a, the function group in $EDAI_2$ had an interaction with perovskite, which decelerated the rate of crystal growth. It was stated that the strain caused by crystal stress in the fresh sample gradually relaxed for several days and reached a better crystal structure.[56] Dramatically different from that of $EDAI_2$, as a processing additive, BAI modified the orientation of crystals, which induced three-dimensional (3D) perovskite to 2*D*/3D mixed perovskite. As indicated in Figure 4b, Sn-based PSCs with a device structure of ITO/NiO_x/active layer/PCBM/Al exhibited a PCE of 4.0% for $FASnI_3$ as the photoactive layer, 5.5% for $FASnI_3$−BAI 15%

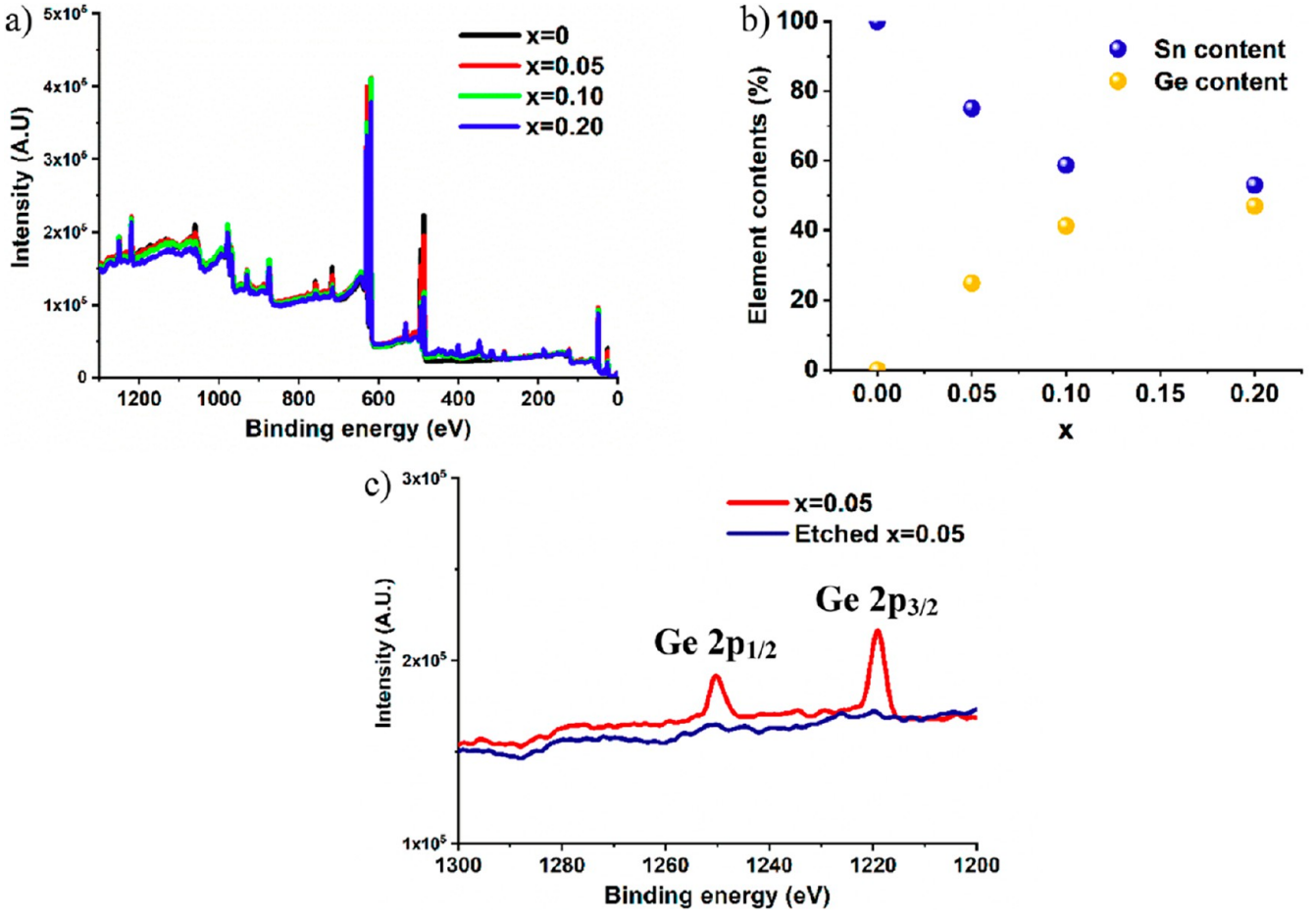

Figure 8. XPS profile for the $FA_{0.75}MA_{0.25}Sn_{1-x}Ge_xI_3$ materials. (a) Wide scan of the different perovskites, (b) the elemental composition of each sample, and (c) comparison of Ge peaks before and after Argon etching. Reproduced with permission from ref 86. Copyright 2018 American Chemical Society.

https://dx.doi.org/10.1021/acsami.0c02575
ACS Appl. Mater. Interfaces 2020, 12, 26776−26811

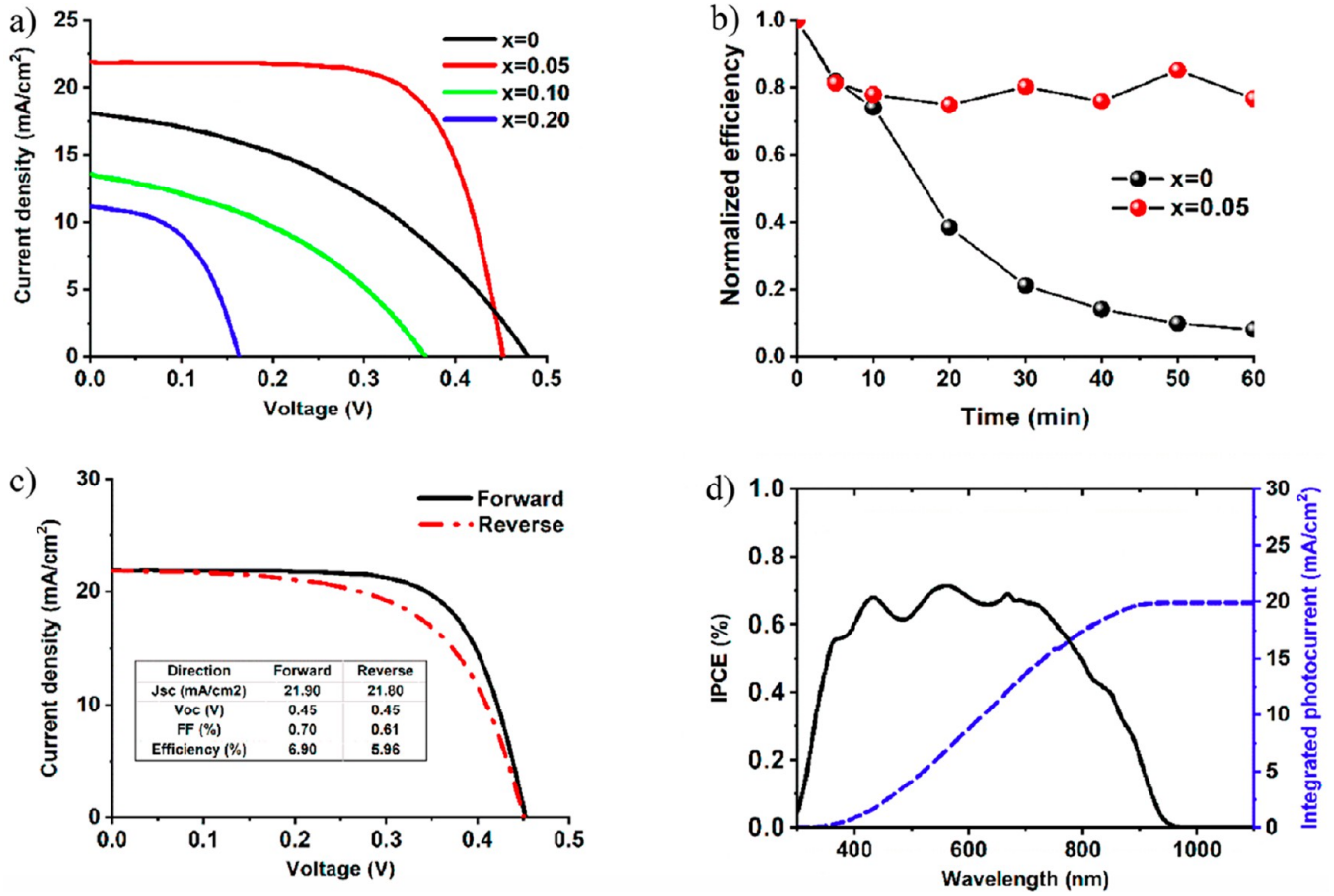

Figure 9. (a) $J-V$ curve of the best-performing devices measured at room temperature under 1 sun illumination in air without encapsulation using a 0.10 cm^2 mask; (b) stability test of the best performing $x = 0$ and $x = 0.05$ solar cells; (c) $J-V$ curve of $x = 0.05$ after 72 h, measured in air without encapsulation, and (d) corresponding IPCE curve. Reproduced with permission from ref 86. Copyright 2018 American Chemical Society.

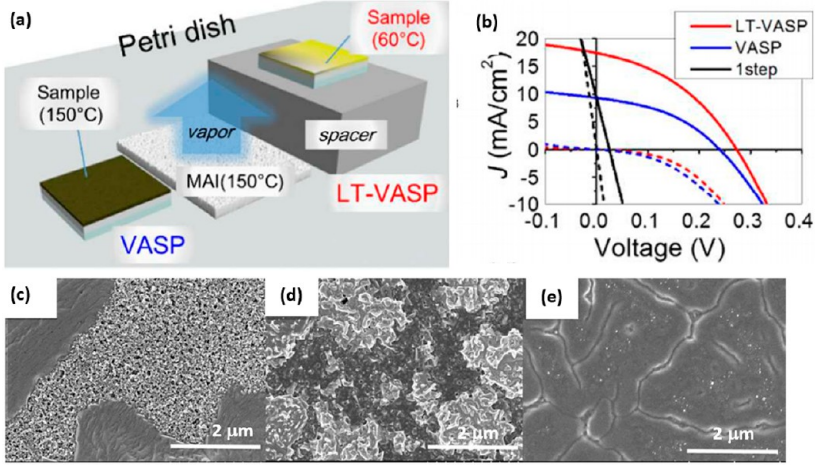

Figure 10. (a) Schematic of VASP and LT-VASP; (b) $J-V$ characteristics of devices fabricated from one-step, VASP, and LT-VASP $MASnI_3$ films; SEM images of film on FTO/TiO_2 substrate: (c) one-step $MASnI_3$, (d) VASP- $MASnI_3$, and (e) LT-VASP- $MASnI_3$. The scale bars indicate 2 μm. Reproduced with permission from ref 94. Copyright 2016 American Chemical Society.

as the photoactive layer, and 7.4% for $FASnI_3$-$EDAI_2$ 1% as the photoactive layer. The Mott–Schottky analysis was used to study the charge carrier densities and the results are shown in Figure 4c. It was found that PSC-based $FASnI_3$-$EDAI_2$ 1% active layer possessed the lowest charge carrier density compared to those of $FASnI_3$ and $FASnI_3$–BAI 15%. These results indicated that fewer defects and less recombination occurred in PSC-based $FASnI_3$-$EDAI_2$ 1% active layer. It was also found that PSCs based on $FASnI_3$–BAI 15% maintained 90% of its initial PCE over 2000 h. Interestingly, PCEs of PSCs based on $FASnI_3$-$EDAI_2$ 1% were even increased from 6.3 to 8.9% after 1462 h (Figure 4d). The enhancement in PCEs was ascribed to the more uniform and smoother surface and less crystal stress induced by $EDAI_2$.

2.1.3. B-Site Composition Engineering. According to hybrid perovskite formula ABX_3, one can modulate the absorption energy interval through B-site and/or X-site substitutions. A-site substitution

https://dx.doi.org/10.1021/acsami.0c02575
ACS Appl. Mater. Interfaces 2020, 12, 26776–26811

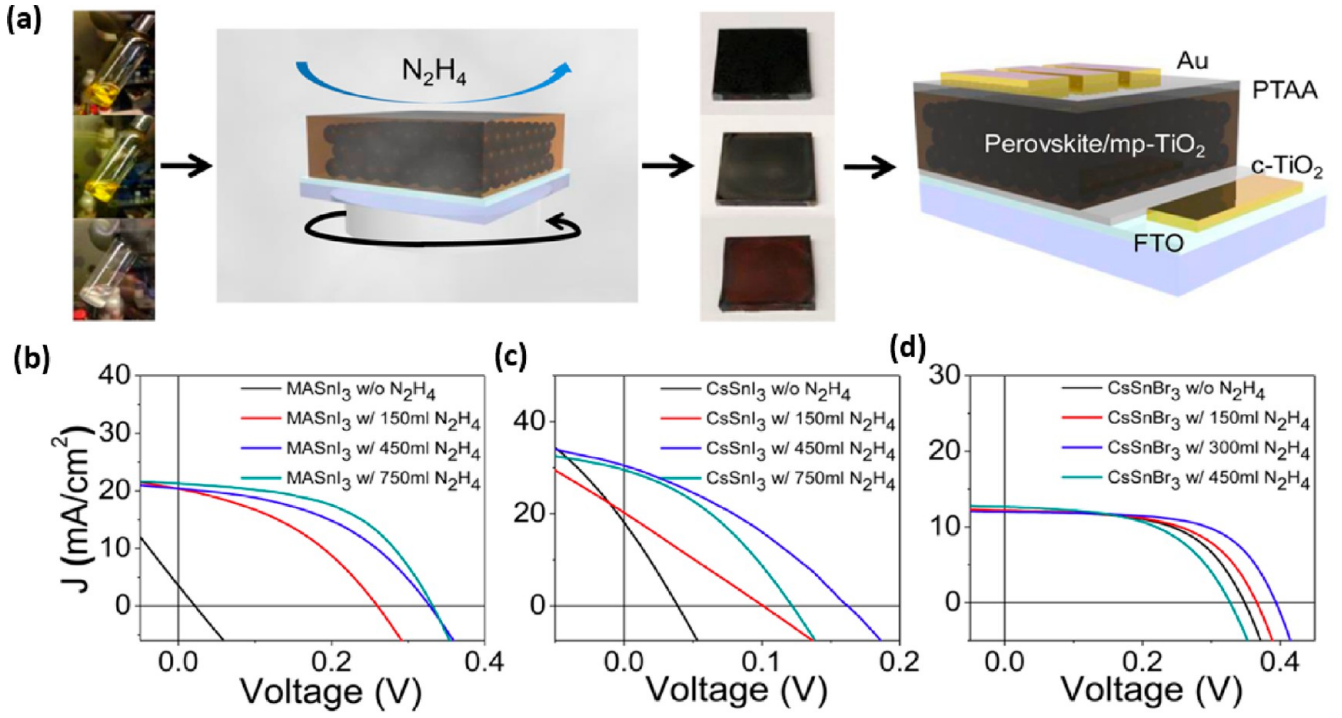

Figure 11. (a) Reducing vapor atmosphere procedure for preparing $MASnI_3$ (top), $CsSnI_3$ (middle), and $CsSnBr_3$ (bottom) perovskite solar cell devices and device structure (glass/FTO/c-TiO_2/mp-TiO_2-perovskite/perovskite capping layer/PTAA/Au); Representative $J-V$ curves for (b) $MASnI_3$ solar cells, (c) $CsSnI_3$ solar cells, and (d) $CsSnBr_3$ solar cells without and with various hydrazine vapor concentrations. Reproduced with permission from ref 59. Copyright 2017 American Chemical Society.

Table 3. Recent Advance of Pure Sn-Based PSCs

perovskite	device structure	J_{SC} (mA/cm^2)	V_{OC} (V)	FF (%)	PCE (%)	ref.
$MASnI_3$	conventional (ETL: TiO_2; HTL: spiro-OMeTAD)	16.8	0.88	42	6.40	55
$FA_{0.75}MA_{0.25}SnI_3$	inverted (HTL: PEDOT:PSS; ETL: C60/BCP)	21.2	0.61	62.7	8.12	81
$FA_{0.75}MA_{0.25}Sn_{0.95}Ge_{0.05}I_3$	inverted (HTL: PEDOT:PSS; ETL: C60/BCP)	19.5	0.42	55.0	4.48	86
$MASnI_3$(N_2H_4 reducing vapor atmosphere)	conventional (ETL: TiO_2; HTL: PTAA)	19.9	0.38	51.7	3.89	59
$CsSnI_3$(N_2H_4 reducing vapor atmosphere)	conventional (ETL: TiO_2; HTL: PTAA)	30.8	0.17	34.9	1.83	59
$CsSnBr_3$(N_2H_4 reducing vapor atmosphere)	conventional (ETL: TiO_2; HTL: PTAA)	14.0	0.37	59.4	3.04	59
$CsSnI_3$(N_2H_4 reducing vapor atmosphere, extra SnI_2 as additive)	conventional (ETL: TiO_2; HTL: PTAA)	25.7	0.38	49.1	4.81	63
$MASnI_3$(Gas–solid reaction by LT-VASP)	conventional (ETL: TiO_2; HTL: PTAA)	17.8	0.27	39.0	1.86	94
$FASnI_3$	inverted (HTM: PEDOT:PSS)	22.07	0.465	60.6	6.22	27
$FASnI_3$ + 20 mol % SnF_2 + 15 mol % BAI	inverted (HTM: PEDOT:PSS)	18.0	0.440	69.4	5.5	56
$FASnI_3$ + 20 mol % SnF_2 + 1 mol % $EDAI_2$	inverted (HTM: PEDOT:PSS)	20.0	0.516	71.6	7.4	56
$FASnI_3$ + 20 mol % SnF_2 + 1 mol % $EDAI_2$ (stored in a glovebox for over 1400 h)	inverted (HTM: PEDOT:PSS)	21.3	0.583	71.8	8.9	56
$FASnI_3$ + 20 mol % SnF_2 + TMA (2-step)	normal/compact SnO_2	21.65	0.31	64.7	4.34	95
$FASnI_3$ + 20 mol % SnF_2 + TMA (2-step)	inverted (HTM: PEDOT:PSS)	22.45	0.47	67.8	7.09	95
$PEA_2FA_{24}Sn_{25}I_{76}$ (2D/3D mixed)	inverted (HTM: PEDOT:PSS)	24.1	0.525	71.0	9.0	39

would induce less impact on absorption property, but affect other perovskite properties such as charge carrier lifetime.[73] Composition engineering can be easily achieved by perovskite solution processing, which has been fully demonstrated in Pb-based perovskite system.[74−77] Thus, it is essential and accessible to investigate the composition engineering of Sn-based perovskite materials. Malavasi et al.[78] first explored $FA_{1-x}MA_xSnBr_3$ system with a wide band gap. As shown in Figures 5a, b, $FA_{1-x}MA_xSnBr_3$ (where x = 0, 0.05, 0.2, 0.3, 0.6, 0.8, and 1.0) possessed similar cubic lattices, but with decreased lattice parameter α as MA contents are increased. The bandgap of mixed-perovskite materials could be defined from the absorption spectra, as shown in Figures 5c, d. A considerable energy variation up to 0.5 eV was observed from $FASnBr_3$ (2.4 eV) to $FA_{0.18}MA_{0.82}SnBr_3$ (1.92 eV), which was in contrast to the results observed from the Pb-based perovskite system. In general, A-site substitution induces less contribution to band energy change.[73] In this case, however, for cubic Sn-based perovskite, the p-electrons from N and C had a contribution to the conduction band (the lowest unoccupied molecular orbital energy level (LUMO)).[79] Furthermore, in a mixed A-site system of $FA_{1-x}MA_xSnBr_3$ cubic lattice, the FA cation induced a different valence band (highest occupied molecular orbital (HOMO)) contributio, resulting in a wide band gap variation, which was also affected by different molecular size between MA and FA.[80]

https://dx.doi.org/10.1021/acsami.0c02575
ACS Appl. Mater. Interfaces 2020, 12, 26776−26811

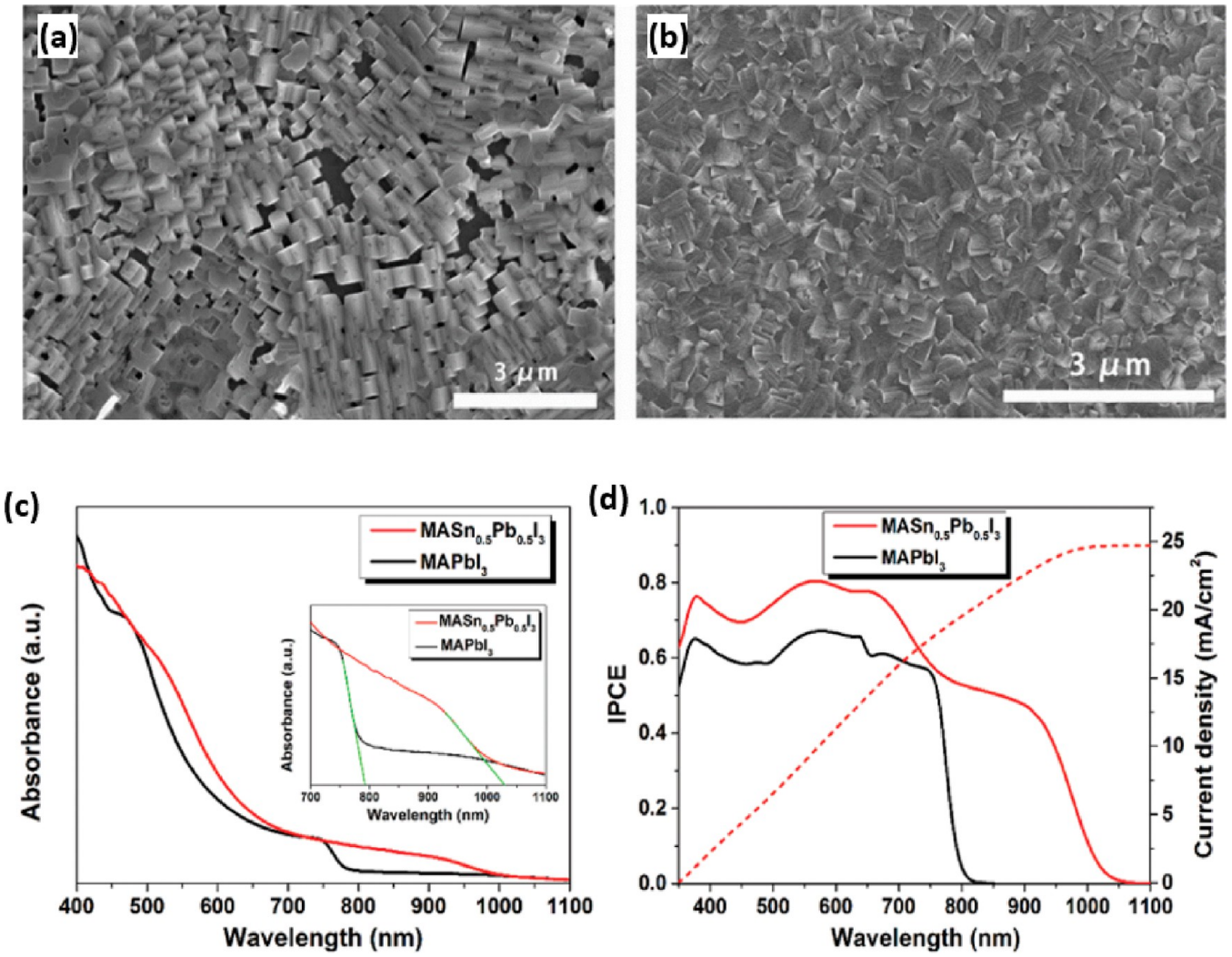

Figure 12. SEM images for (a) $MASnI_3$ perovskite film and (b) $MASn_{0.5}Pb_{0.5}I_3$ perovskite film. All are fabricated by a two-step method. (c) Absorption spectra of the $MASn_{0.5}Pb_{0.5}I_3$ and $MAPbI_3$ films. Inset is magnification of infrared portions. (d) Incident photon-to-electron conversion efficiency (IPCE) spectra of the inverted planar solar cells based on $MASn_{0.5}Pb_{0.5}I_3$ and $MAPbI_3$. Reproduced with permission from ref 101. Copyright 2016 Wiley.

Table 4. Recent Advance of Mixed Sn−Pb-Based PSCs

composition	E_g (eV)	V_{OC}(V)	J_{SC}(mA/cm^2)	FF (%)	PCE (%)	ref
$MAPb_{0.85}Sn_{0.15}I_{3-x}Cl_x$	1.38	0.77	19.5	67	10.1	100
$MASn_{0.5}Pb_{0.5}I_3$	1.18	0.75	26.3	68.8	13.6	101
$MA_{0.5}FA_{0.5}Pb_{0.75}Sn_{0.25}I_3$	1.33	0.78	23.03	79	14.19	82
$FA_{0.75}Cs_{0.25}Sn_{0.5}Pb_{0.5}I_3$	∼1.2	0.74	26.7	71	14.1	77
$(FASnI_3)_{0.6}(MAPbI_3)_{0.4}$	∼1.2	0.795	26.86	70.6	15.08	76
$(FASnI_3)_{0.6}(MAPbI_3)_{0.4}$	1.25	0.853	28.5	72.5	17.6	107

Similar to Malavasi's work, Huang and his co-workers demonstrated 8.12% efficiency from PSCs by Sn-based perovskite with mixed FA and MA components.[81] As shown in Figure 6, $FA_xMA_{1-x}SnI_3$ (with different ratio 0, 0.25, 0.5, 0.75, and 1.0) possessed enlarged band gap and decreased HOMO energy levels as FA cation ratios are increased. Interestingly, the corresponding absorption spectra did not give clear energy information, which is probably due to the oxidation of Sn^{2+}.[82,83] $FA_{0.75}MA_{0.25}SnI_3$ showed the best PCE up to 8.12% with both enlarged V_{OC} and FF. In addition, they also found that PSCs by $FA_{0.75}MA_{0.25}SnI_3$ thin film retained 80% efficiency after being stored in the glovebox for 400 h. The SEM images studies as shown in Figure 7 demonstrated that grain boundaries became more evident and pinholes were reduced as the ratios of FA are raised from 0 to 0.75.

Another composition engineering approach, more specifically, through B-site substitution was also demonstrated to have the possibility to modify the device performance of Sn-based PSCs.[84,85] Hayase et al. reported Sn−Ge mixed perovskite in the form of $FA_{0.75}MA_{0.25}Sn_{1-x}Ge_xI_3$[86] and found that the best device performance was observed from $FA_{0.75}MA_{0.25}Sn_{1-x}Ge_xI_3$ with a low ratio doping of Ge (x = 0.05), whereas higher concentration substitution would result in higher lattice disorder.[87] As illustrated in Table 2, a decreased intensity of Sn^{4+} could be witnessed by XPS spectra as Ge concentration was increased. Such a passivation effect on Sn oxidation might derive from small ionic radii of Ge atom.[86] More interestingly, even if in the low concentration doping, the element content ratio on the surface was higher than those in bulk, which indicated that Ge

https://dx.doi.org/10.1021/acsami.0c02575
ACS Appl. Mater. Interfaces 2020, 12, 26776−26811

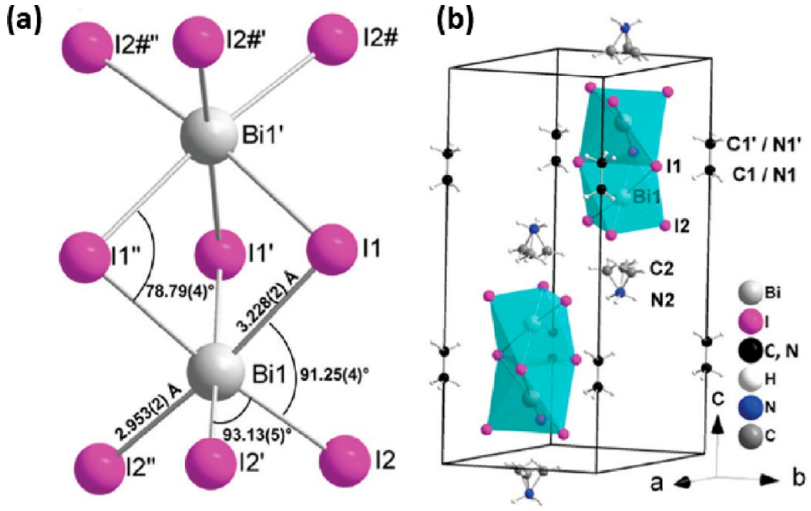

Figure 13. Schematic picture of crystal structure of $(CH_3NH_3)_3Bi_2I_9$ (MABiI): (a) local structure of the $Bi_2I_9^{3-}$ anion; (b) cation and anion positions in the unit cell. Reproduced with permission from ref 113. Copyright 2016 Royal Society of Chemistry.

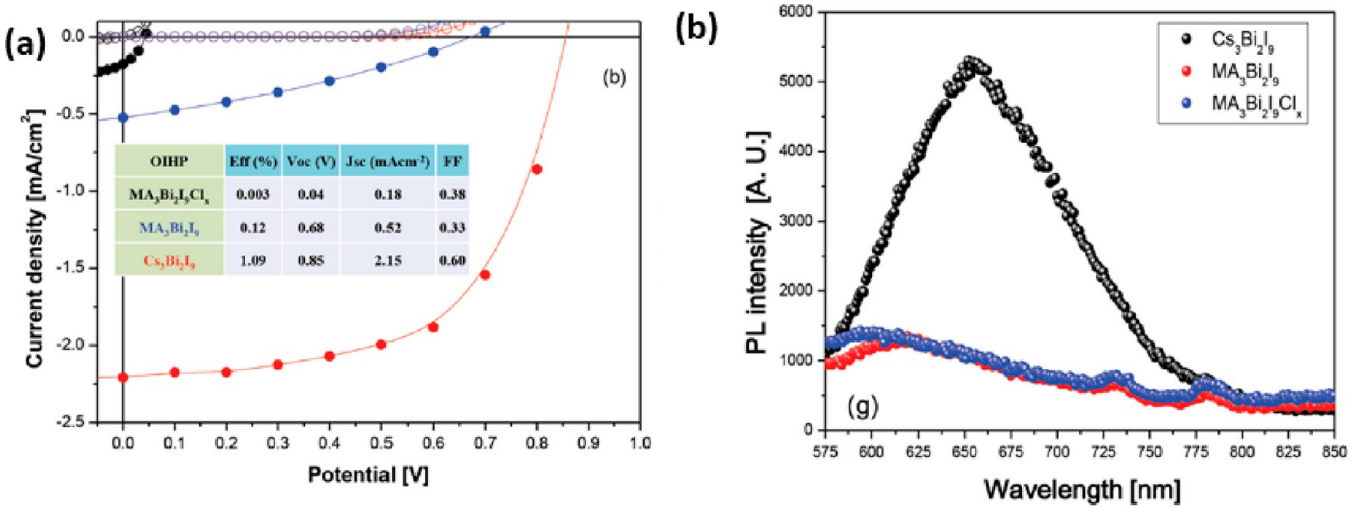

Figure 14. (a) $J-V$ characteristics for solar cells using the three different materials. (b) PL spectra for the three materials. Reproduced with permission from ref 112. Copyright 2015 Wiley.

possesses rich dispersion on the surface of the perovskite layer (Figure 8). Therefore, surface passivation by B-site doping could be formed by filling the defects or vacancies on the surface. Although a small atom size of Ge induced smaller crystal size than that of pristine Sn-based perovskite, the modified surface and passivation effect could still enhance device performance. Figure 9 displays the device performance of PSCs by Ge−Sn mixed perovskite with a 0.05 ratio of Ge doping. The results clearly demonstrated that PSCs exhibited superior stability as they were exposed to air. As shown in Figure 9c, it was surprising that the same device showed self-healing properties and an increased PCE as it was tested after being kept in a dark N_2 atmosphere for 72 h. This could be a slow coalescence of smaller grains into a larger one, resulting in further reduced grain boundaries and suppressed charge carrier recombination effect.[88,89] More recently, Su and his co-workers demonstrated a possibility of mixing group II elements, including Ca and Sr with Sn to tune band gap and improve the thermal stability of the corresponding PSCs.[90]

2.1.4. Two-Step Fabrication Method. So far, most of the studies were focused on using the one-step method to fabricate Sn-based perovskite thin films.[91] Because of the quick crystallization process, however, such a one-step method usually faced randomly oriented growth, which was one major reason for poor surface coverage and film morphology of Sn perovskite.[92] Many effects have been paid to improve the device performance of Pb-based PSCs by different fabrication methods.[93] Kanatzidis et al.[94] devoted the concentration on new fabrication methods of Sn-based perovskites and demonstrated that film quality of $MASnI_3$ can be modified by low-temperature vapor-assisted solution process (LT-VASP). They first prepared SnI_2 film on the top of the mesoporous TiO_2 substrate, then put MAI powder into a preheated Petri dish at 150 °C for 1 min. Afterward, SnI_2 sample was placed next to MAI powder to form perovskite through gas (MAI)-solid (SnI_2) reaction. Surprisingly, the perovskite phase was formed very quickly (within 1 min), which was attributed to the covalent character and a short length of Sn−I bond. Figure 10a illustrated how the temperature was modified in preparation for $MASnI_3$ thin films. As indicated in Figures 10c−e, perovskite thin films showed better surface coverage and film morphology through modification. This phenomenon could be attributed to different crystallization processes at a different temperature: as the substrate temperature was higher than 80 °C, SnI_2 tended to be crystallized before reacting with MAI, which was further verified by XRD patterns. The $J-V$ characteristics of PSCs were displayed in Figure 10b. The PSCs fabricated by LT-VASP exhibited a PCE of 1.86%, with a V_{OC} of 0.27 V, a J_{SC} of 17.36 mA cm^{-2}, and a FF of 39%. Furthermore, the authors used hydrazine as the vapor rather than SnF_2 additives to suppress oxidation of Sn^{2+}.[59]

https://dx.doi.org/10.1021/acsami.0c02575
ACS Appl. Mater. Interfaces 2020, 12, 26776−26811

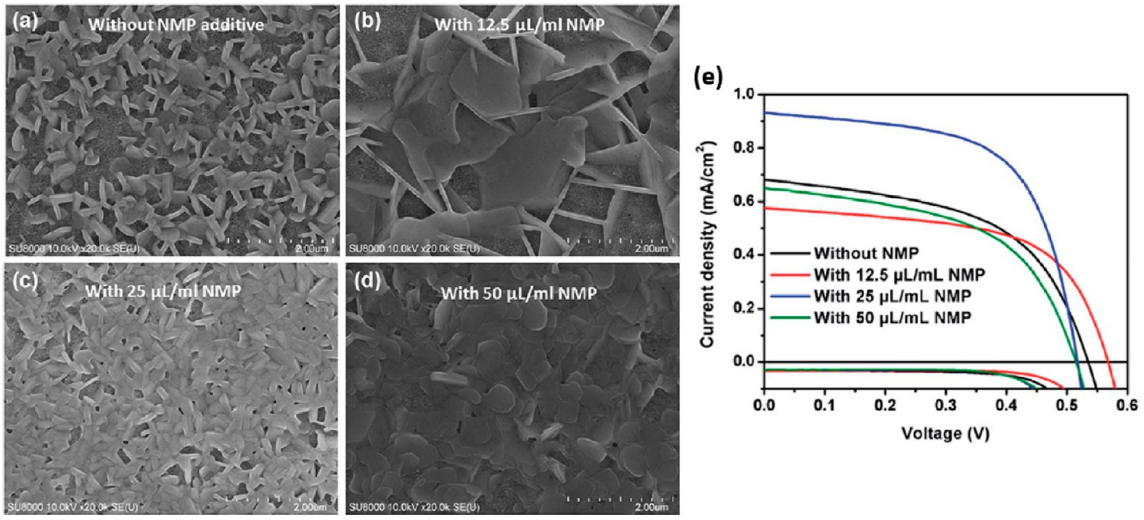

Figure 15. Top surface SEM images of MBI perovskites (a) without and (b–d) with different concentration of NMP additives. (e) Average *J*–*V* curves of devices containing MABI perovskite without and with different concentration of NMP. Reproduced with permission from ref 115. Copyright 2016 Royal Society of Chemistry.

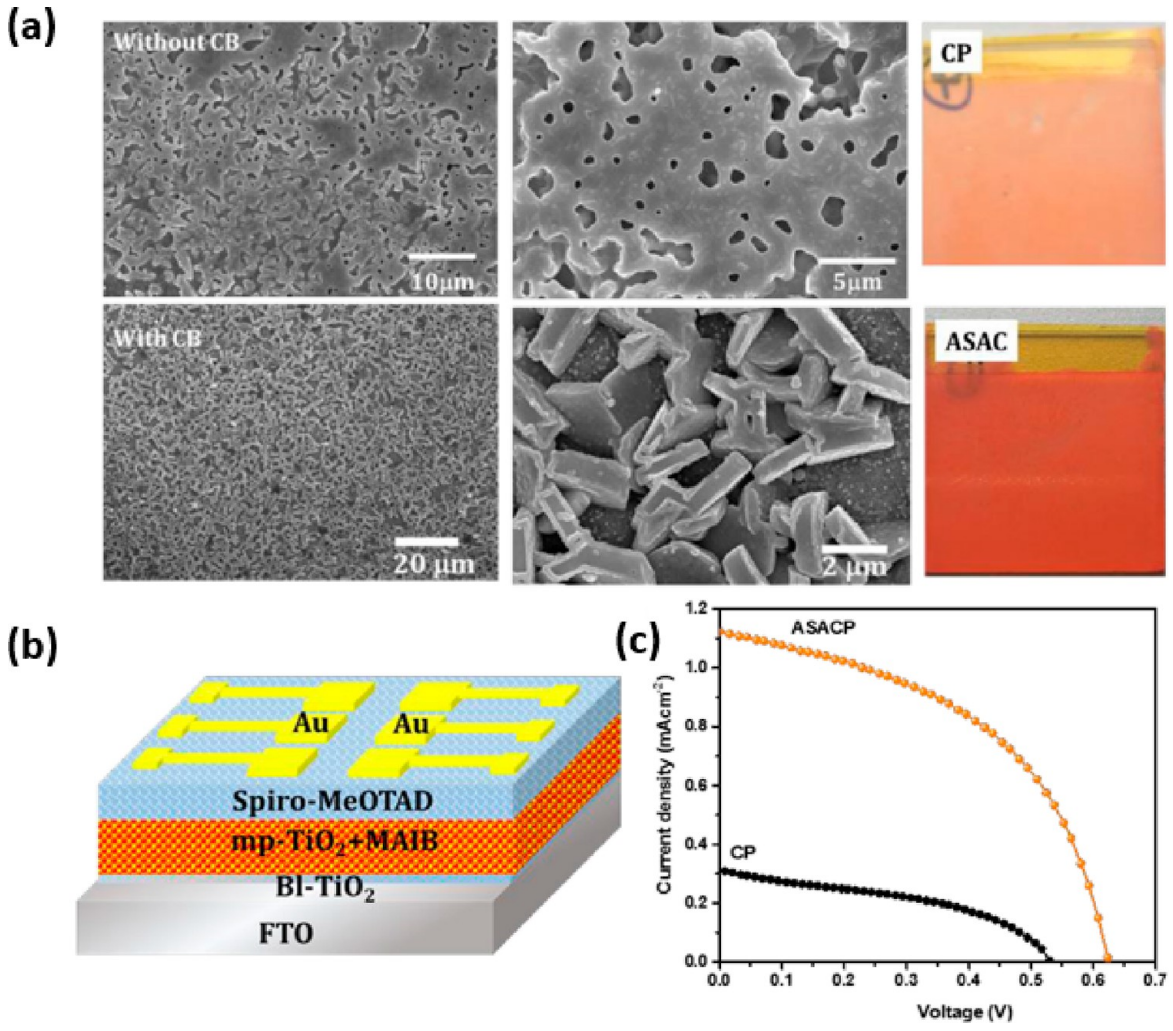

Figure 16. (a) Field-emission scanning electron microscopic (FESEM) images of MAIB thin films deposited by conventional process (CP) and antisolvent assisted crystallization process (ASACP). (b) Schematic representation of the device configuration. (c) *J*–*V* performance of MAIB devices fabricated by CP and ASCAP. Reproduced with permissionfrom ref 116. Copyright 2017 Wiley.

As shown in Figure 11a, Sn-based perovskite thin films were fabricated under the hydrazine atmosphere. Enhanced device performance for different Sn-based perovskites can be witnessed by the *J*–*V* characteristics as shown in Figure 11b-d. For example, with

https://dx.doi.org/10.1021/acsami.0c02575
ACS Appl. Mater. Interfaces 2020, 12, 26776–26811

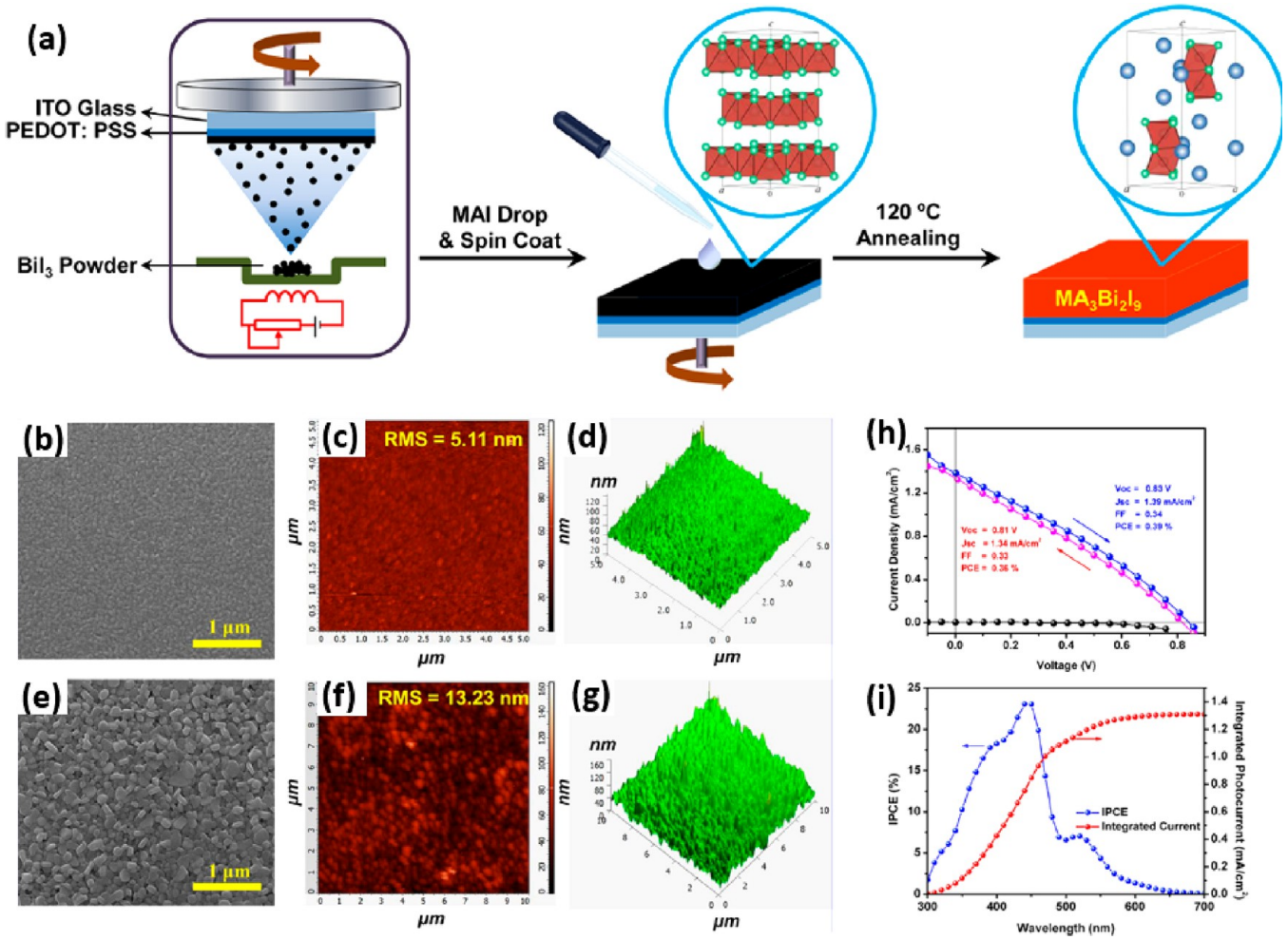

Figure 17. (a) Fabrication Procedure of $MA_3Bi_2I_9$. (b) Thin film SEM, (c) tapping-mode AFM, and (d) 3D AFM images of evaporated BiI_3 film; (e) SEM, (f) tapping-mode AFM, and (g) 3D AFM images of $MA_3Bi_2I_9$ film. (h) Forward and backward scanning and (i) IPCE spectra of the best-forming device. Reproduced with permission from ref 117. Copyright 2017 American Chemical Society.

proper amounts of hydrazine vapor, PCEs of PSCs by $MASnI_3$ were improved dramatically, from an average of ~0.02 to 3.40%. This trend is also observed in $CsSnI_3$ and $CsSnBr_3$ based PSCs, increasing from ~0.16 to 1.50% and ~2.36 to 2.82%, respectively. More importantly, XPS studies indicated that the intensity of Sn^{4+} was reduced as a proper amount of hydrazine added, which indicated a suppressed oxidation process was existed in reducing the vapor atmosphere. Such a reduction process can be considered as a reaction between hydrazine and Sn^{4+} in form of $2SnI_6^{2-} + N_2H_4 \rightarrow 2SnI_4^{2-} + N_2 + 4HI$, which was happened at the same time of perovskite formation, strongly suppressing p-type self-doping, consequently resulting in superior device performance. Besides, a sharper absorption edge from UV−vis measurement suggested a lower level of defects, which was further demonstrated by the time-resolved PL decay. With different fabrication methods, Kanatzidis et al.[59] successfully prepared modified Sn-based perovskite films and then observed enhanced device performance from the corresponding PSCs. Their results demonstrated the possibility to approach high-performance Sn-based PSCs.

Recently, Zhu et al. used a two-step solution-processed method to produce a uniform $FASnI_3$ thin film with a large grain size.[95] In this work, trimethylamine (TMA) was adopted as a Lewis base in the SnY_2 (Y = I^- or F^-) solution to generate SnY_2-TMA complexes. The formation of SnY_2-TMA weakened the affinity with FA^- in the second step so the reaction rate could be modulated. Owing to the large size of the complexes as compared with SnI_2, a compact film with large crystals was observed. XRD patterns also proved a better crystallinity of $FASnI_3$ thin film, which was induced by TMA. As a result, PSCs exhibited a J_{SC} of 22.45 mA/cm^2, a V_{OC} of 0.47 V, and a fill factor of 67.8%, with a corresponding PCE of 7.09%.[95]

Table 3 summarizes recent advances of pure Sn-based PSCs. Fabrication of Sn-based PSCs indeed avoids the toxicity issues to some extent. However, Sn-based PSCs still exhibited low PCEs, compared to Pb-based PSCs.

2.1.5. Sn−Pb Mixed Perovskites. In order to enhance PCEs, researchers developed PSCs by perovskite thin films, where Pb was partially replaced by Sn.[96−98] By tuning the ratio of Sn to Pb, mixed perovskite materials exhibit bandgaps from 1.17 to 1.55 eV.[99] Thus, mixing Sn with Pb can broaden the light absorption to the near-infrared spectrum, consequently resulting in enlarged J_{SC}.

Zuo et al. fabricated PSCs with a device structure of ITO/PEDOT:PSS/$MAPb_{0.85}Sn_{0.15}I_{3-x}Cl_x$/PCBM/$C_{60}$-bis/Ag.[100] They reported the elemental analysis and structure analysis of $MAPb_{0.85}Sn_{0.15}I_{3-x}Cl_x$, and found out that as the ratio of Sn increases, the structure of $MAPb_{0.85}Sn_{0.15}I_{3-x}Cl_x$ varied from the tetragonal *I4cm* to the *P4mm* symmetry, and the perovskite unit cell size was decreased. The optimal composition $MAPb_{0.85}Sn_{0.15}I_{3-x}Cl_x$ thin film had better coverage, smoother surface, enhanced crystallinity, and fewer pinholes compared to pure Pb perovskite $MAPbX_3$. It was also found that PSCs by $MAPb_{0.85}Sn_{0.15}$ $I_{3-x}Cl_x$ thin film showed a remarkable enhancement in J_{SC} and FF, which was attributed to broadened absorption and improved film quality and surface coverage.

Li et al. used a two-step spin-coating method to fabricate a mixed-metal based PSCs with an inverted planar structure of ITO/PEDOT:PSS/perovskite/C_{60}/BCP/Ag.[101] As shown in Figure 12, the SEM images indicated that $MASnI_3$ film was discontinuous and

https://dx.doi.org/10.1021/acsami.0c02575
ACS Appl. Mater. Interfaces 2020, 12, 26776−26811

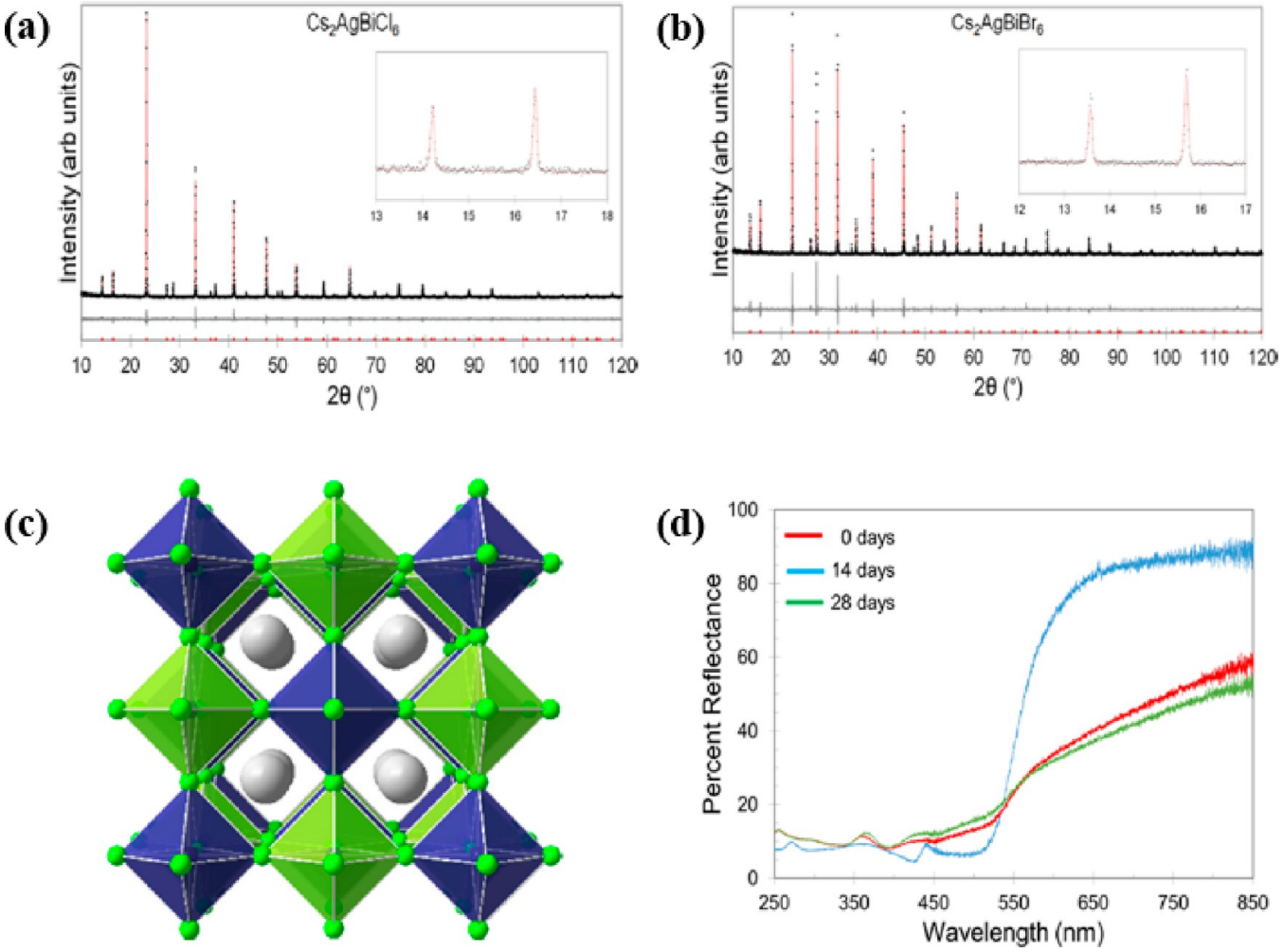

Figure 18. Rietveld refinements of the XRPD patterns for (a) $Cs_2AgBiCl_6$ and (b) $Cs_2AgBiBr_6$. The black dots and red and gray lines are the experimental pattern, calculated fit, and difference curve, respectively. Red tick marks at the bottom give the expected peak positions. The inset shows the fit to the (111) and (200) reflections. (c) Refined crystal structure of $Cs_2AgBiCl_6$. The Cs^+ ions are shown as gray spheres, the chloride ions as small green spheres, whereas the Ag- and Bi-centered octahedra are shown as blue and green polyhedra, respectively. (d) UV−vis diffuse spectra showing the light instability of $Cs_2AgBiBr_6$ after 2 and 4 weeks of light exposure. Reproduced with permission from ref 118. Copyright 2016 American Chemical Society.

had a large number of cracks or dispersive grains. whereas $MASn_{0.5}Pb_{0.5}I_3$ thin film was very smooth and uniform and with no breaks. Absorption and external quantum efficiency (EQE) spectra showed that the absorption edges of $MASn_{0.5}Pb_{0.5}I_3$ perovskite and $MAPbI_3$ are 1050 and 808 nm, corresponding to the bandgaps 1.18 and 1.53 eV, respectively. The optimal PSCs showed a PCE up to 13.6% with a V_{OC} of 0.75 V, a J_{SC} of 26.3 mA/cm^2, and a FF of 68.8%.

Yang et al. studied PSCs by mixed cation and metal perovskite $MA_{1-y}FA_yPb_{1-x}Sn_xI_3$.[82] They first employed an inverted device structure of ITO/PEDOT:PSS/$MAPb_{1-x}Sn_xI_3$/PCBM/Bis-C_{60}/Ag and found that as x is 0.25, PSCs showed a PCE of 14.35% with a V_{OC} of 0.82 V, a J_{SC} of 22.44 mA/cm^2, and a FF of 78%, whereas PSCs by pure Pb perovskite exhibited a PCE of 14.07% with a V_{OC} of 0.92 V, a J_{SC} of 19.60 mA/cm^2, and a FF of 78%. Because partial substitution of MA^+ with FA^+ can retard the oxidation of Sn^{2+} in Sn-based perovskites, which would result in improved film stability.[102−107] Therefore, they fixed the ratio of Pb to Sn and introduced different amounts of FA to form $MA_{1-y}FA_yPb_{0.75}Sn_{0.25}I_3$ perovskites. It was further found that PSCs by $MA_{0.5}FA_{0.5}Pb_{0.75}Sn_{0.25}I_3$ thin film exhibited the highest PCE of 14.19% and good stability (PSCs stored in a N_2 atmosphere can maintain more than 94% of their initial PCE after 30 days).[82]

Eperon et al. studied PSCs with an inverted planar heterojunction device structure of ITO/PEDOT:PSS/$FASn_xPb_{1-x}I_3$/C_{60}/BCP/Ag (or Au), where BCP is bathocuproine.[77] It was found that as x = 0.5, PSCs by $FASn_xPb_{1-x}I_3$ thin film reached the highest PCE of 10.90%. They also studied $FACsSn_{0.5}Pb_{0.5}I_3$ and found that 25% of FA replaced by Cs had little impact on the optoelectronic properties or film quality of the resultant perovskite materials, but PSCs showed enhanced values. Compared to PSCs by $FASn_{0.5}Pb_{0.5}I_3$ (with the highest PCE of 10.90%), PSCs by $FA_{0.75}Cs_{0.25}Sn_{0.5}Pb_{0.5}I_3$ thin film exhibited a J_{SC} of 26.7 mA/cm^2, a V_{OC} of 0.74 V, and a FF of 0.71, with a corresponding PCE of 14.10%, with no appreciable rate-dependent hysteresis at the same time.

Liao et al. mixed different molar ratios of $FASnI_3$ with $MAPbI_3$ precursor solutions to fabricate $(FASnI_3)_{1-x}(MAPbI_3)_x$-based PSCs.[76] The film morphology was characterized by SEM and AFM technologies. Compared to pristine $FASnI_3$ or $MAPbI_3$, the $(FASnI_3)_{0.6}(MAPbI_3)_{0.4}$ film contained smaller grains, but the distribution of grain size was more uniform. The surface root-mean-square roughness of $(FASnI_3)_{0.6}(MAPbI_3)_{0.4}$ was also much more modest. From the result of PL emission peaks and the EQE spectrum, the bandgap of $(FASnI_3)_{0.6}(MAPbI_3)_{0.4}$ was estimated to be 1.2 eV. They applied a device structure of ITO/PEDOT:PSS/$(FASnI_3)_{0.6}(MAPbI_3)_{0.4}$/$C_{60}$/BCP/Ag for investigating photovoltaic properties of this novel perovskite material. PSCs by $(FASnI_3)_{0.6}(MAPbI_3)_{0.4}$ thin film exhibited a PCE of 15.08% with a V_{OC} of 0.795 V, a J_{SC} of 26.86 mA/cm^2, and a FF of 70.6%, measured

https://dx.doi.org/10.1021/acsami.0c02575
ACS Appl. Mater. Interfaces 2020, 12, 26776−26811

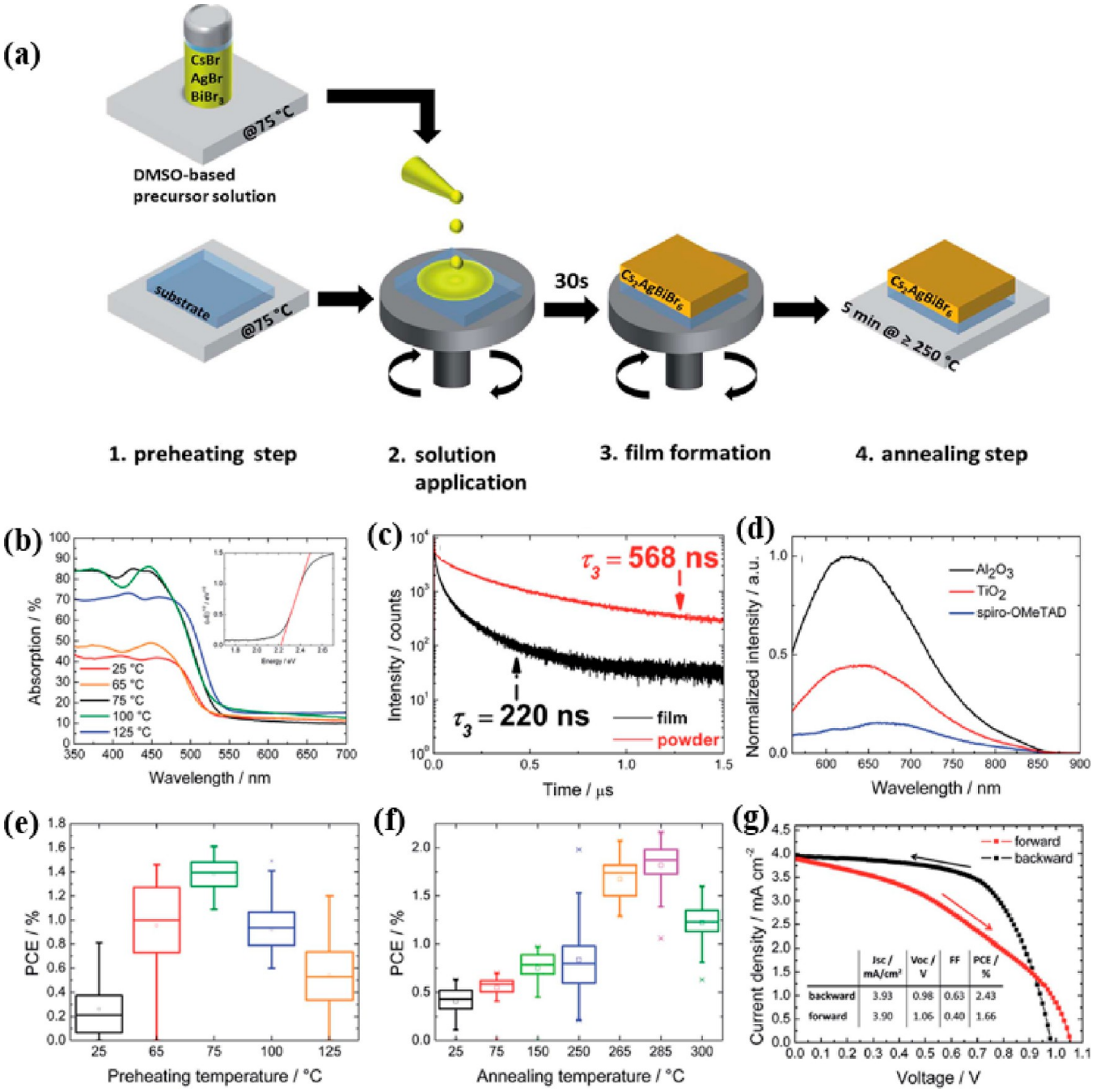

Figure 19. (a) Schematic of the synthesis route for $Cs_2AgBiBr_6$ thin films. (b) Optical absorption spectra of $Cs_2AgBiBr_6$ films prepared from DMSO on flat glass substrates. (c) TCSPC decays of a $Cs_2AgBiBr_6$ film on glass and polycrystalline powder. (d) PL emission spectra of $Cs_2AgBiBr_6$ films on mp-Al_2O_3, mp-TiO_2, and mp-Al_2O_3 covered with spiro-OMeTAD. (e) Device performance as a function of preheating temperature, values obtained from 48 individual devices per temperature. (f) Device performance of solar cells assembled with $Cs_2AgBiBr_6$ films preheated at 75 °C as a function of annealing temperature and (g) $J-V$ curve of the best-performing device. Reproduced with permission from ref 119. Copyright 2017 Royal Society of Chemistry.

under forwarding scan direction. Although under the reverse scan direction, PSCs showed a PCE of 15.00% with a V_{OC} of 0.799 V, a J_{SC} of 26.82 mA/cm^2, and a FF of 70.0%. These device performance parameters indicated that PSCs possessed suppressed photocurrent hysteresis behavior.

Zhao et al.[107] further modified the low-bandgap mixed Sn−Pb perovskite device system. They used relatively thick (ca. 600 nm) perovskite layer with large grains and long carrier lifetimes (up to 250 ns). A V_{OC} of 0.85 V was observed, whereas the EQE value in the range of 700−900 nm (IR region) was more significant than 70%, resulting in an impressive J_{SC} of over 29 mA/cm^2. A PCE of 17.6% was observed and the certified value was 17.01%.[107]

Table 4 summarizes the recent advances of mixed Sn−Pb-based PSCs.

2.2. Bi-Based Perovskite Solar Cells. Pb-free alternatives are the zero-dimensional (0D) Bi-based perovskites $A_3Bi_2X_9$ (e.g., A = Cs^+, MA^+; X = I^-, Br^-).[36−38] The studies indicated that these materials possess high band gap of E_g > 1.8 eV,[39,108,109] which are good candidates for making tandem or triple solar cells.[110,111] Bi is a nontoxic element, and Bi-based perovskites showed better chemical stability under ambient atmosphere than Pb-based perovskites

https://dx.doi.org/10.1021/acsami.0c02575
ACS Appl. Mater. Interfaces 2020, 12, 26776−26811

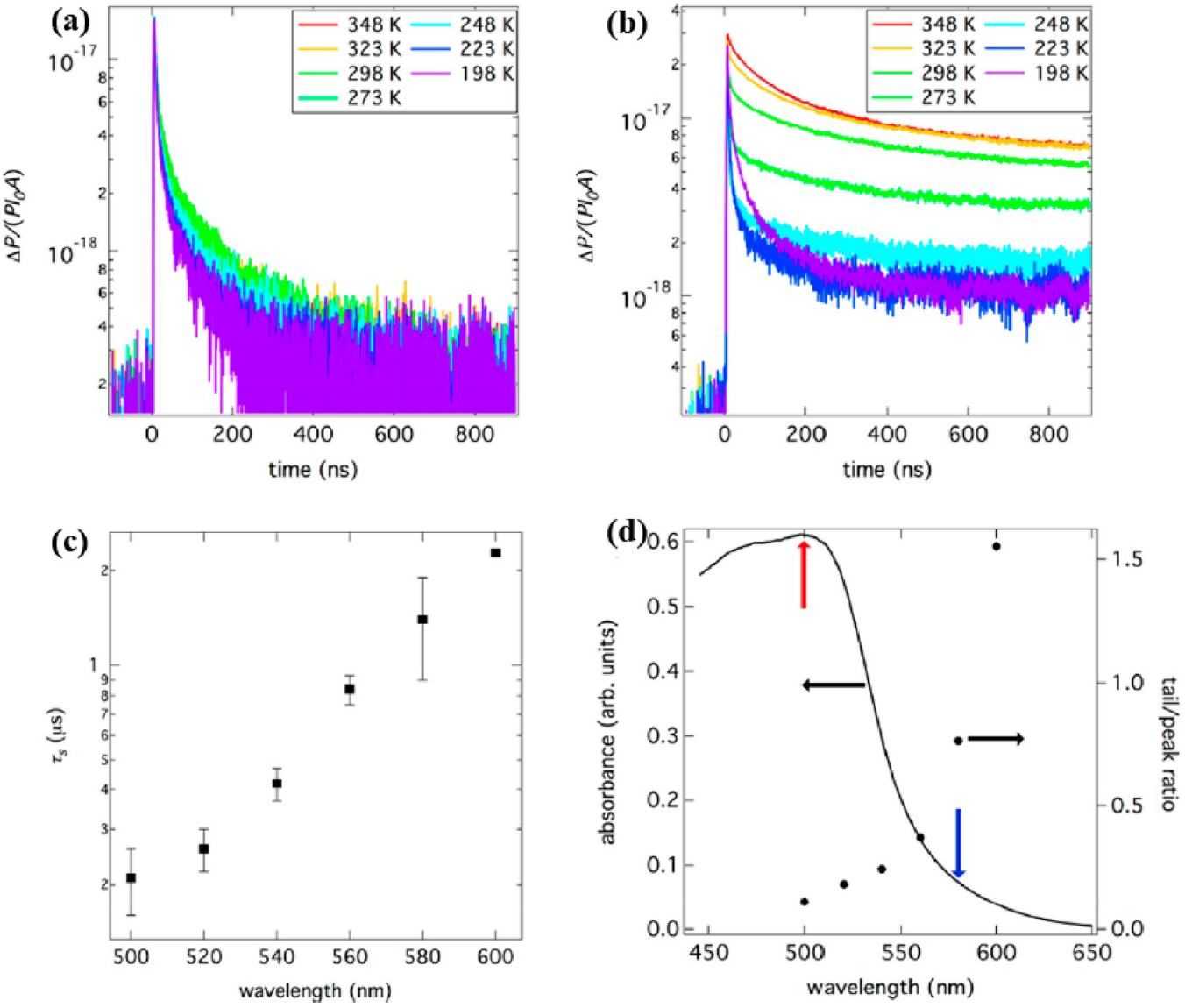

Figure 20. (a, b) TRMC traces for $Cs_2AgBiBr_6$ crystals recorded upon pulsed laser excitation at (a) 500 and (b) 580 nm at indicated temperatures. The fraction of absorbed microwave power $\Delta P/P$ is normalized for the number of incident photons ($I_0 \approx 1.1 \times 10^{15}$ cm^{-2}) and for the surface area of the sample ($A \approx 0.12$ cm^2); (c) decay constant of the slow component of the room temperature TRMC traces measured upon pulsed laser excitation at different wavelengths; (d) absorbance spectrum of $Cs_2AgBiBr_6$ (solid line) and the tail/peak ratio of the TRMC traces measured upon pulsed laser excitation at different wavelengths, with incident photon fluence $I_0 \approx 1.1 \times 10^{15}$ cm^{-2} (dots). The red and blue arrows indicate the absorbance at 500 and 580 nm, respectively. Reproduced with permission from ref 123. Copyright 2018 American Chemical Society.

because of its unique crystal structure, which is presented in Figure 13.[112,113] Park et al.[112] first demonstrated low-toxicity Bi-based PSCs with a device configuration of FTO/TiO_2(solid) under layer/mesoscopic-TiO_2/perovskite/hole transport materials/Ag. The $J-V$ characteristics of PSCs are shown in Figure 14a. The best device performance was observed from PSCs by $MA_3Bi_2I_9$ (MABiI) thin film, which exhibited a J_{SC} of 0.52 mA cm^{-1}, a V_{OC} of 0.68 V, a FF of 0.33, with a corresponding PCE of 0.12%, respectively. The main reason for such low J_{SC} was attributed to the nonradiative recombination. Figure 14b presents the PL spectra of three different perovskite materials. The small PL may be caused by the bandgap states, lowering the efficiency of PSCs by $MA_3Bi_2I_9$ thin film.

2.2.1. One-Step Fabrication Method. The critical challenge in MABiI perovskites made by one-step spin coating process is to control crystallization. The gas-assisted one-step solution method was reported by Okano et al.[114] They utilized this technique to deposit a dense and smooth MABiI layer and found that PSCs by MABiI layer exhibited a PCE of 0.082% (J_{SC} = 0.372 mA/cm^2, V_{OC} = 0.686 V, FF = 0.32). Recently, A. Kulkarni reported that high-quality MABiI could be obtained by using *N*-methyl-2-pyrrolidone (NMP) as a morphology controller in the MABiI-DMF solution to tune the rate of crystallization.[115] Figure 15a–d demonstrates how the film morphology changed with different concentrations of NMP additive. At a high concentration of NMP (2.5% or 25 μL mL^{-1}), the film morphology altered drastically. The SEM results suggested that the grain size was enlarged with the increasing concentration of NMP additive. However, as shown in Figure 15e, with further increasing the concentration of NMP to 5% (50 μL mL^{-1}), the J_{SC} was decreased, which was attributed to the nonsmooth region of MABiI perovskite layer over the substrate, and the perovskite from the concentration of NMP (2.5% or 25 μL mL^{-1}) covered the electron transporting layer more uniformly. As a result, PSCs by the MABiI device treated with NMP (2.5% or 25 μL mL^{-1} showed a PCE of ~0.31%.

Mali et al.[116] synthesized MABiI cuboids by an antisolvent assisted crystallization process (ASACP). The field emission scanning electron microscopy (FESEM) images as shown in Figure 16a indicated that

https://dx.doi.org/10.1021/acsami.0c02575
ACS Appl. Mater. Interfaces 2020, 12, 26776–26811

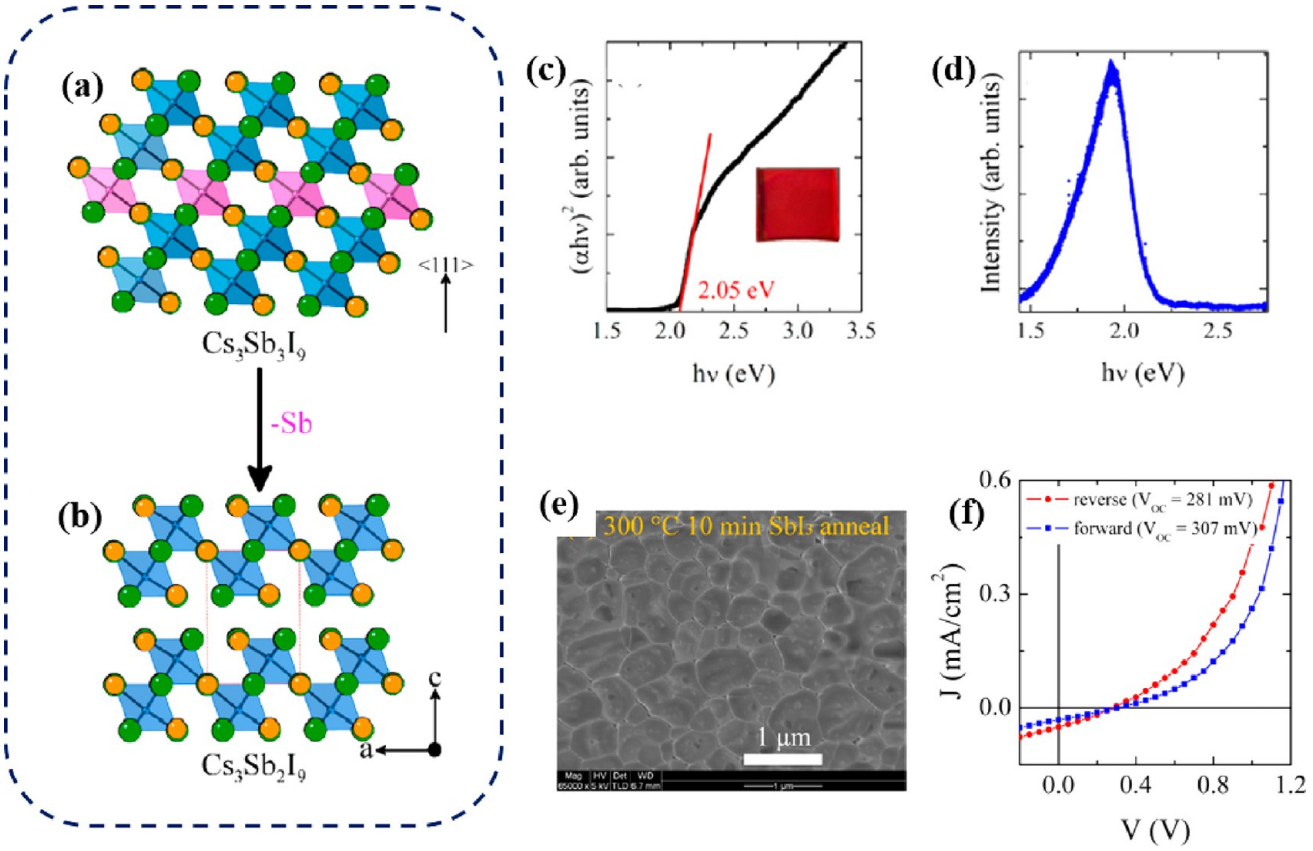

Figure 21. Removal of every third Sb layer along the ⟨111⟩ direction of (a) the perovskite structure results in (b) the 2D layered modification of $Cs_3Sb_2I_9$. Cs and I atoms are shown as orange and green spheres, respectively; Sb coordination polyhedra are shown in blue and pink. (c) Band gap of the layered modification of $Cs_3Sb_2I_9$ (inset shows a thin film) was calculated to be 2.05 eV from absorbance data using the Tauc relation. (d) Photoluminescence spectrum of $Cs_3Sb_2I_9$ obtained using 442 nm laser excitation. (e) SEM image of $Cs_3Sb_2I_9$ thin film, deposited via coevaporation of CsI and SbI_3 followed by annealing at 300 °C for 10 min in SbI_3 vapor atmosphere (f) Hysteresis effect of layered $Cs_3Sb_2I_9$ PSCs with forward to reverse and reverse to forward directions. Reproduced with permission from ref 122. Copyright 2015 American Chemical Society..

the samples with antisolvent (CB) exhibited a regular arrangement of cuboid-shaped the J_{SC} was enhanced over three times, with increased V_{OC} from PSCs by MABiI cuboids through ASACP, resulting in a PCE of 0.356%. All these results demonstrated that MABiI was a promising material toward Pb-free perovskite photovoltaics. However, MABiI thin film was nonuniform with island morphology owing to the crystallization process of MABiI crystal was so quick.

2.2.2. Two-Step Fabrication Method. Ran et al.[117] reported that a two-step BiI_3 salt evaporation technique was an effective strategy to yield efficient Bi-based PSCs. As illustrated in Figure 17a−g, smooth and continuous MABiI grains can be realized by a two-step fabrication method. The thermal evaporation technique yielded a flat BiI_3 and more continuous crystal grains. As a result, a uniform and compact MABiI thin-film promoted PSCs with a V_{OC} over 0.80 V and a champion PCE of 0.39%. However, the low FF (0.34) was observed, which was probably originated from the short carrier diffusion length and low charge mobility of MABiI thin film.

2.2.3. Double Perovskites. Bi^{3+}-containing hybrid halides are typical with a low-dimensional structure, such as $(MA)_3Bi_2I_9$, which gives rise to a larger band gap induced by the quantum confinement. Therefore, in order to incorporate with the trivalent Bi^{3+} into a 3D perovskite architecture, a combination with a monovalent cation is necessary to form a double perovskite, such as $A_2M^IM^{III}X_6$ (A and M^I = Li, Na. K, Rb, Cs, Tl, Ag, etc.; M^{III} = Al, Bi, Fe, Ga, Ln, etc.; and X = F, Cl, Br, or CN).[118−122] Very recently, Cs_2AgBiX_6 (X = Cl or Br) was reported by three different groups.[118−120] McClure et al.,[118] observed the crystal structure of Cs_2AgBiX_6 from the inspection of XRPD patterns. The results shown in Figure 18 revealed that both compounds adopt the cubic double perovskite structure with $Fm\bar{3}m$ space group symmetry. Similar to the Pb-based perovskite structure, a 3D framework of corner is connected octahedra with Cs^+ ions occupying the cuboctahedra cavities. Based on the Kubelka−Munk equation and Tauc method, the optical bandgap of $Cs_2AgBiBr_6$ was estimated to be 2.19 eV. To confirm the stability of double perovskite materials, the samples were exposed to an ambient atmosphere for about one month. UV−vis diffuse reflection spectroscopy results revealed drastically change after 2 weeks of exposure to light and ambient air. These results suggested that double perovskite materials still suffer from degradation as it was exposed to light and/or air.

Greul et al.,[119] reported a solution-processed double perovskite $Cs_2AgBiBr_6$ films via a fast and efficient spin-coating method. The detailed processes were described in Figure 19a. The bandgap of the $Cs_2AgBiBr_6$ film was determined from the absorption spectra, which is demonstrated in Figure 19b. It was found that a steep onset is at ∼550 nm, which corresponding to an E_g of 2.21 eV for a direct bandgap is obtained with a Tauc plot as shown in Figure 19b. Figure 19c presents the PL decay times of the double perovskite films by the method termed as the time-correlated single-photon counting (TCSPC). It was found that both powder and the thin film showed elongated PL decay times in the range of hundreds of nanoseconds, similar to the values observed from Pb-based perovskites, and the decay times do not differ significantly between single crystals and polycrystalline powders, which suggests a high defect tolerance of this kind of materials. As shown in Figure 19d, maximum PCE was observed at 75 °C indicating improved optical properties of thin film.

Interestingly, the increased device performance at 75 °C preheating is not only caused by an increased J_{SC}, but also by the enhanced FF and by the increased V_{OC}. They believed that the preheating could improve the mp-TiO_2/double perovskite interface, resulting in boosted device performance. It was likely that preheating to 75 °C

https://dx.doi.org/10.1021/acsami.0c02575
ACS Appl. Mater. Interfaces 2020, 12, 26776−26811

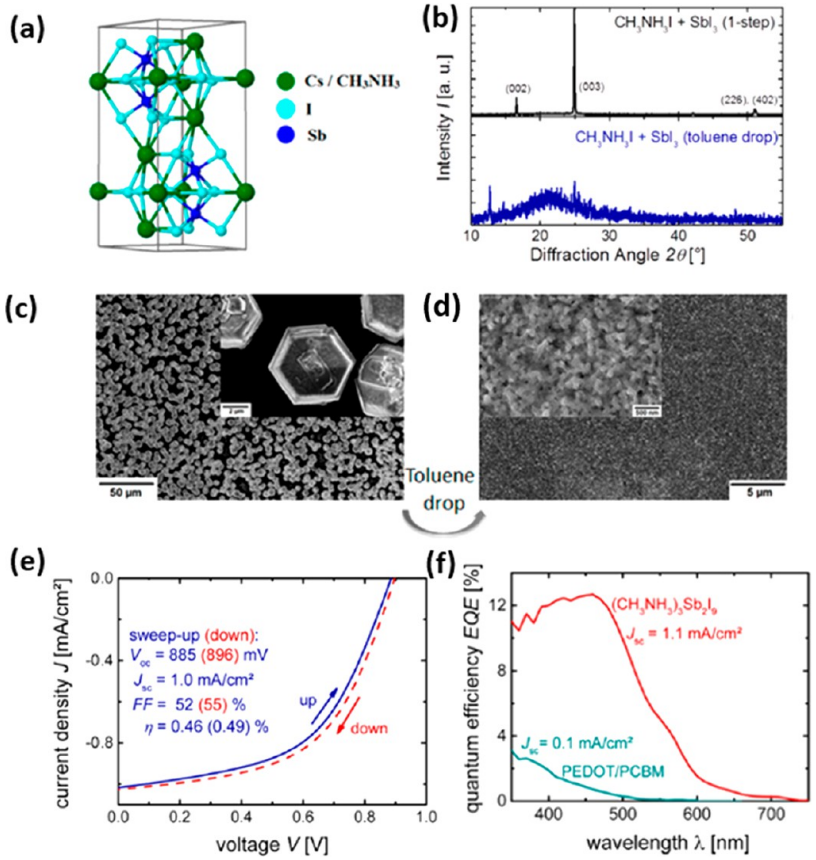

Figure 22. (a) Crystal structure of $(CH_3NH_3)_3Sb_2I_9$ (space group *P*63/*mmc*), (b) XRD pattern of $(CH_3NH_3)_3Sb_2I_9$ thin films prepared by the one-step spin-coating process (upper panel) and after the toluene drop (lower panel), (c) SEM image of the $(CH_3NH_3)_3Sb_2I_9$ thin film, showing hexagonal crystals after one-step spin-coating, and (d) SEM image of the thin film with additional an toluene drop during spin-coating with the two-step process. (e) Illuminated *J*−*V* curve of $(CH_3NH_3)_3Sb_2I_9$ solar cell measured with "up" and "down" sweep with a rate of 0.1 V/s. (f) EQE measurement of the $(CH_3NH_3)_3Sb_2I_9$ solar cell compared to the reference device (ITO (120 nm)/PEDOT/PCBM/ZnO-NP/Al). Reproduced with permission from ref 35. Copyright 2016 American Chemical Society.

resulted in double perovskite films featuring strongly improved optoelectronic properties. However, the full conversion of the precursors into the double perovskite phase was achieved by annealing at 250 °C, as shown in Figure 19d. As shown in Figure 19e, the highest and most reproducible PCEs were obtained from PSCs where perovskite was annealed at a temperature of 285 °C and the best PCE was 2.43%. In particular, a V_{OC} of 0.98 V was significantly higher than that by other Bi-based compounds featuring comparable E_g. These results indicated the potential for the development of a wide range of double perovskites for diverse environmentally friendly optoelectronic applications.

The low efficiency from double perovskite is likely due to fast charge carrier recombination at the film surface. Bartesaghi et al.[123] characterized thin films and crystal structure of $Cs_2AgBiBr_6$ by time-resolved microwave conductance (TRMC), which probes the formation and decay of mobile charges upon pulsed irradiation. The photoinduced TRMC technique measures the change in photoconductance gain (ΔG) as a function of time on optical excitation of the sample.[123] The ΔG transients measured for a 400 nm thick film of $Cs_2AgBiBr_6$ upon optical excitation at different wavelengths are shown in Figure 20. It was found that the decay of the TRMC signals was slightly slower for excitation at a long wavelength. The slope of $\log(\varphi\Sigma\mu)$ versus $\log(I_0)$(where φ is the product of the charge photogeneration yield, μ is the sum of electron and hole mobility, and I_o is the number of incident photons, respectively) is close to −1/2, which implies a dominant bimolecular decay process happens, such as band-to-band recombination.[123] It should be noted that the value of φ may be limited due to the faster charge carrier decay, which is within the scale of instrument response time. They found that the charge carrier mobility (sum of electron and hole mobility) in $Cs_2AgBiBr_6$ thin film is ∼1 $cm^2\ V^{-1}\ s^{-1}$, which is much lower than the value reported by $CH_3NH_3PbI_3$ thin film (35 $cm^2\ V^{-1}\ s^{-1}$).[124] Figure 20c displays τ_s versus the wavelength (where τ_s is the decay constants of the slow components of the traces). The increment in values above 1 μs with a longer wavelength implied that the TRMC signals for $Cs_2AgBiBr_6$ single-crystal shown a longer decay tail at a longer wavelength. The absorption spectra of polycrystalline $Cs_2AgBiBr_6$ and A_s and A_f (where A_s and A_f are the tail/peak ratio of the slow and fast components of the TPMC traces, respectively) are shown in Figure 20d. It was found that the absorption of polycrystalline $Cs_2AgBiBr_6$ decreases quickly, but the tail/peak ratio increases, which may be ascribed to the increment of light penetration depth. They proposed that the fast charge carrier recombination at $Cs_2AgBiBr_6$ thin film surface was responsible for the inferior device performance.[123]

2.3. Sb-Based Perovskite Solar Cells. Antimony-based perovskite $Cs_3Sb_2I_9$ has been intensively investigated by Mitzi group.[122] The optical band gap value of 2.05 eV was confirmed by absorption using Tauc relation, as demonstrated in Figure 21c-d. The SEM images shown in Figure 21e proved that a highly oriented $Cs_3Sb_2I_9$ thin film can be achieved by annealing the coevaporated film in SbI_3 vapor at 300 °C for 10 min, which was further confirmed by XRD patterns. However, as shown in Figure 21f, the PCE value was lower than 1% with a huge hysteresis effect.

Recently, Hebig et al.[35] introduced 0D $(CH_3NH_3)_3Sb_2I_9$ (MASbI) perovskite as a possible candidate for Pb-free PSCs. They fabricated PSCs by using both a one-step method (SbI_3 + CH_3NH_3I in a mixture of γ-butyrolactone (GBL) and dimethyl sulfoxide (DMSO)) and a

https://dx.doi.org/10.1021/acsami.0c02575
ACS Appl. Mater. Interfaces 2020, 12, 26776−26811

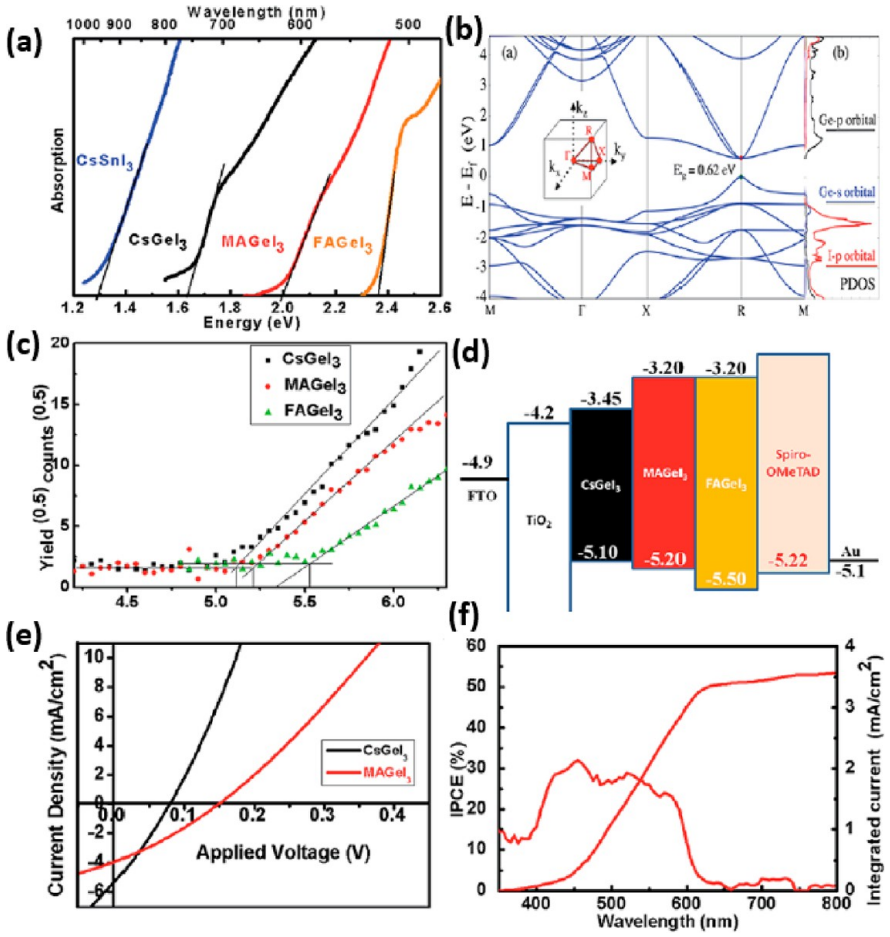

Figure 23. (a) Optical absorption spectrum of $CsGeI_3$, $MAGeI_3$ and $FAGeI_3$, in comparison with $CsSnI_3$. (b) Calculated band structure and projected density of states of cubic $CsGeI_3$. The energy of the highest occupied state is set to 0 eV. (c) Photoelectron spectroscopy in air (PESA) of powder samples and (d) schematic energy level diagram of $CsGeI_3$, $MAGeI_3$ and $FAGeI_3$. (e) $J-V$ curves of photovoltaic devices fabricated with different germanium halide perovskites. (f) IPCE spectrum of the $MAGeI_3$ device. Reproduced with permission from ref 31. Copyright 2015 Royal Society of Chemistry.

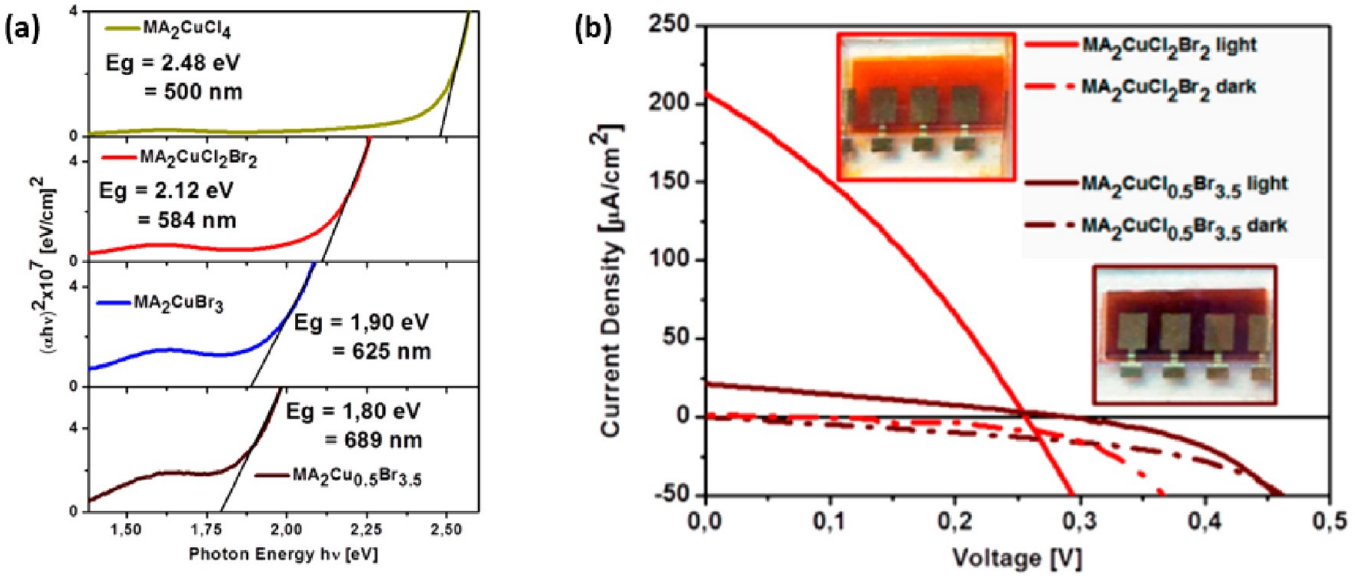

Figure 24. (a) Tauc plots for the determination of band-gaps associated with charge transfer (CT) Transitions, (b) the $J-V$ curve of solar cells sensitized with $MA_2CuCl_2Br_2$. Reproduced with permission from ref 40. Copyright 2016 American Chemical Society.

two-step method (SbI_3, CH_3NH_3I), followed with low-temperature annealing (100−120 °C). As shown in Figure 22a, MASbI obtained by a one-step method with dropping toluene on the top shows a hexagonal structure, but with poor homogeneity of the thin film. By a

https://dx.doi.org/10.1021/acsami.0c02575
ACS Appl. Mater. Interfaces 2020, 12, 26776−26811

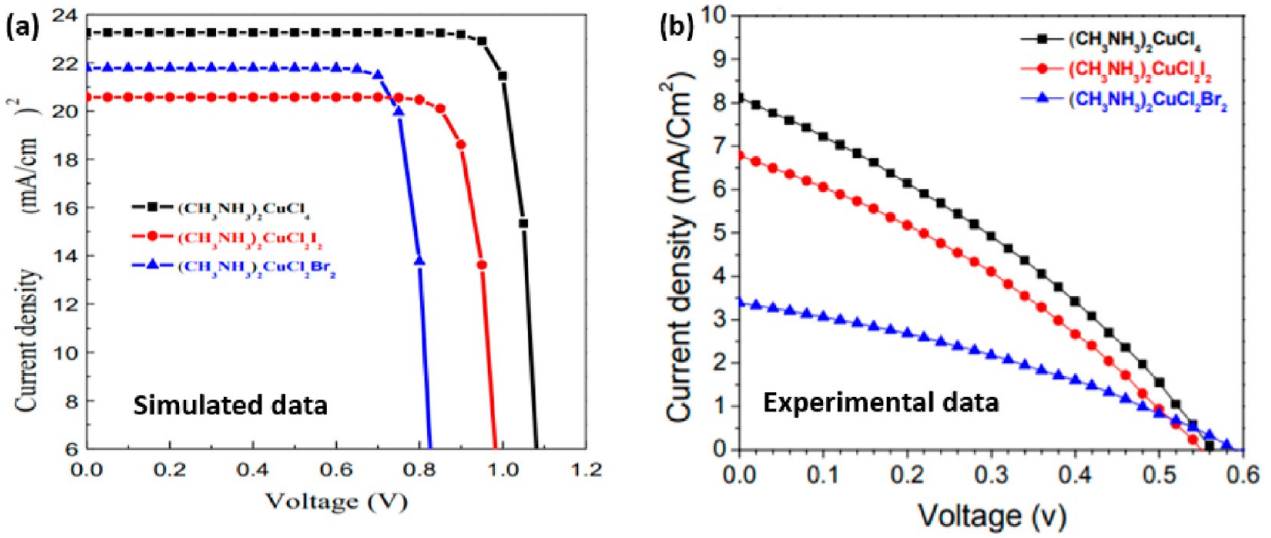

Figure 25. (a) Simulated and (b) experimental $J-V$ curves of solar cells by different Cu^{2+}-based perovskite materials. Reproduced with permission from ref 41. Copyright 2018 American Chemical Society.

Table 5. Recent Advance of Bi, Sb, Ge, and Cu-Based PSCs

perovskite	J_{SC} (mA/cm^2)	V_{OC} (V)	FF (%)	PCE (%)	ref
$(CH_3NH_3)_3Bi_2I_9$	0.52	0.68	33	0.12	112
$(CH_3NH_3)_3Bi_2I_9$(Gas-assisted)	0.37	0.69	32	0.082	114
$(CH_3NH_3)_3Bi_2I_9$(without NMP)	0.68	0.53	53	0.19	115
$(CH_3NH_3)_3Bi_2I_9$(12.5 μL NMP)	0.70	0.51	51	0.18	115
$(CH_3NH_3)_3Bi_2I_9$(25 μL NMP)	0.94	0.51	61	0.31	115
$(CH_3NH_3)_3Bi_2I_9$(50 μL NMP)	0.65	0.51	52	0.18	115
$(CH_3NH_3)_3Bi_2I_9$(ASACP)	1.10	0.653	49.6	0.356	116
$(CH_3NH_3)_3Bi_2I_9$(thermal evaporation)	1.40	0.83	34.0	0.39	117
$(CH_3NH_3)_2AgBrBr_6$	3.90	0.98	63	2.43	119
$(CH_3NH_3)_3Sb_2I_9$(one-step method and mixed with GBL)	1.00	0.89	52	0.48	35
$MAGeI_3$	4.00	0.15	30	0.20	31
$(CH_3NH_3)_2CuCl_2Br_2$	0.22	0.26	32	0.017	40
$(CH_3NH_3)_2CuCl_2I_2$	6.78	0.55	47	1.75	41
$(CH_3NH_3)_2CuCl_2Br_2$	3.35	0.58	50	0.99	41
$(CH_3NH_3)_2CuCl_2Cl_4$	8.12	0.56	52	2.41	41

two-step method, a homogeneous, flat, and compact thin film was achieved, which is essential for application in photovoltaic devices. They fabricated PSCs with a device configuration of ITO (120 nm)/PEDOT:PSS (25 nm)/$(CH_3NH_3)_3Sb_2I_9$ (300 nm)/$PC_{61}BM$ (60 nm)/ZnO-NP (60 nm)/Al (150 nm) and found that PSCs exhibited a J_{SC} of 1.1 mA/cm^2 with suppressed hysteresis at a scan speed of 0.1 V/s. The relatively small J_{SC} was attributed to short charge carrier lifetime of MASbI materials. Nevertheless, the maximum EQE of MASbI perovskite is 12%.[35]

2.4. Ge-Based Perovskite Solar Cells. Previous efforts have led to the discovery of a series of Pb-free perovskite based on Sn, Sb, Bi.[26,35,39,55] However, there was a rare report on Ge-based perovskites, which is probably due to the critical drawbacks of Ge-based PSCs.[31,125] The structural instabilities originated from spontaneous oxidation during the synthesis and fabrication procedures and the solubility of Ge in polar solvents are probably two major factors. In addition, high cost and expensive refinement techniques are required in synthesizing Ge-based PSCs.

Krishnamoorthy et al.[31] used computational screening to prove that Ge is indeed a promising alternative element for Pb in perovskite materials for solar cell application. They found that with increasing size of A^+ cation in perovskite, the color of the final film changes from black to orange, as shown in Figure 23a. Figure 23b displays the bandgap of Ge-based perovskite versus different cation substitutions. These results suggested that Ge-based perovskite is a suitable material for tandem solar cells. To confirm the functionalities of A^+ cation (Cs, MA, and FA), we used photoemission spectroscopy to estimate the valence band of different perovskite. As demonstrated in Figure 23c, it was found that the replacement of Cs with MA and FA could reduce the valence band of the resultant perovskites. Figure 23d–f presents J_{SC} of ~5.7 and ~4.0 mA cm^{-2} for $CsGeI_3$ and $MAGeI_3$-based PSCs, respectively. Although a low J_{SC} was observed from $MAGeI_3$-based PSCs, Ge-based halide perovskite possesses great potentials for photovoltaic applications.

2.5. Cu-Based Perovskite Solar Cells. The first Cu-based halide perovskite as the light harvester with the 2D crystal structure of $MA_2CuCl_xBr_{4-x}$ was reported by Cortecchia et al.[40] The authors systematically investigated the optical band gap by increasing the concentrations of Br from 2.48 eV for MA_2CuCl_4 to 1.80 eV for $MA_2CuCl_{0.5}Br_{3.5}$ (Figure 24a). The $MA_2CuCl_xBr_{4-x}$ active layer was spun coated onto the PEDOT:PSS from one-step method by mixing precursors of MABr, MACl, $CuCl_2$ and $CuBr_2$ at different ratio. However, a very low PCE of 0.017% with rather poor J_{SC} and V_{OC} were observed from PSCs with a device structure of FTO/mesoporous TiO_2/$MA_2CuCl_2Br_2$/PCBM/Al, as shown in Figure 24b. The low absorption coefficient and unbalanced charge carrier mobilities were the main restriction for high performance of Cu-based halide PSCs. However, this work provided guidelines for future investigation of Cu-based halide PSCs.

https://dx.doi.org/10.1021/acsami.0c02575
ACS Appl. Mater. Interfaces 2020, 12, 26776–26811

Table 6. Crystal Structure, Trap Density, Absorption, and Stability of Low-Toxicity Perovskite Materials[a]

perovskite materials	crystal structure	trap density	absorption range (nm) or bandgap (eV)	stability	ref
$FASnI_3$	orthorhombic	1×10^{19}	370−900	NA	27
$FASnI_3(SnF_2)$	orthorhombic	1×10^{17}	370−900	maintain 90%/30 days (encapsulated)	27
$FASnI_3(SnF_2)$	orthorhombic	NA	400−900	maintain ∼20%/600 h (encapsulated)	62
$FASnI_3(SnF_2$+2.5 mol % $N_2H_5Cl)$	orthorhombic	NA	400−900	maintain ∼65%/1000 h (encapsulated)	62
$FASnI_3(SnF_2$+5 mol % $N_2H_5Cl)$	orthorhombic	NA	400−900	NA	62
$FASnI_3(SnF_2$+10 mol % $N_2H_5Cl)$	orthorhombic	NA	400−900	NA	62
$(PEA)_2(FA)_{n-1}Sn_nI_{3n+1}$	orthorhombic	2×10^{17}	370−900	maintain ∼96%/100 h (without encapsulated)	68
$PEA_2FA_{24}Sn_{25}I_{76}(n = 25)$	orthorhombic	2.7×10^{16}	500−900	maintain ∼59%/76 h (without encapsulated)	29
$MASnBr_3$	cubic	NA	$E_g = 2.40$	NA	78
$(FA)_{0.75}(MA)_{0.25}SnI_3$	NA	NA	400−900	maintain ∼80%/400 h(In glovebox)	81
$MASnI_3$(LT-VASP)	NA	NA	$E_g = 1.27$	loss black/24 h	94
$MAPb_{0.85}Sn_{0.15}X$(X = Cl)	tetragonal	NA	350−900	NA	100
$MA_3Bi_2I_9$	hexagonal	NA	$E_g = 2.1$	47%/30 days	112
$MA_3Bi_2I_9Cl_x$	hexagonal	NA	$E_g = 2.4$	NA	112
$MA_3Bi_2I_9$	hexagonal	NA	400−600	NA	114
$Cs_2AgBiBr_6$	cubic	NA	$E_g = 2.19$	no apparent change in absorption/28 days	118
$Cs_2AgBiCl_6$	cubic	NA	$E_g = 2.77$	no apparent change in absorption/28 days	118
$Cs_2AgBiBr_6$	cubic	NA	$E_g = 2.21$	no apparent change in efficiency/25 days	119
$MA_3Sb_2I_9$	hexagonal	NA	350−650	NA	35
$MAGeI_3$	cubic	NA	$E_g = 2.20$	NA	31
$FAGeI_3$	cubic	NA	$E_g = 2.35$	NA	31
MA_2CuCl_4	monoclinic	NA	300−500	NA	40
$MA_2CuCl_2Br_2$	orthorhombic	NA	300−600	NA	40
$MA_2CuClBr_3$	orthorhombic	NA	300−650	NA	40
$MA_2CuCl_{0.5}Br_{3.5}$	orthorhombic	NA	300−689	NA	40
MA_2CuCl_4	orthorhombic	1×10^{20}	$E_g = 2.36$	NA	41
$MA_2CuCl_2Br_2$	orthorhombic	1×10^{20}	$E_g = 1.99$	NA	41
$MA_2CuCl_2I_2$	orthorhombic	1×10^{20}	$E_g = 1.04$	NA	41

[a]NA: not available.

Similar work was done by Elseman et al.[41] They did a series of simulation studies of $MA_2CuCl_2Br_2$, $MA_2CuCl_2I_2$ and MA_2CuCl_4 materials on photovoltaics performance. As shown in Figure 25a, the simulated results showed that PSCs based on $MA_2CuCl_2Br_2$ exhibited the highest efficiency of 15.03%, with V_{OC}, J_{SC}, and FF of 0.85 V, 21.8 mA/cm^2, and 82%, respectively. The PSCs based on $MA_2CuCl_2I_2$ exhibited an efficiency of 17.08% with V_{OC}, J_{SC}, and FF of 1.00 V, 20.6 mA/cm^2, and 83%, respectively. The PSCs based on the MA_2CuCl_4 exhibited the highest efficiency of 21.76% with V_{OC}, J_{SC}, and FF of 1.1 V, 23.3 mA/cm^2, and 85%, respectively. These results indicated that Cu^{2+} based PSCs were particularly interesting for low-toxicity PSCs and the Cl^- rich in Cu^{2+} based perovskite materials may exhibit better performance than the one with Br^- rich. However, as shown in Figure 25b, it should be noted that the obtained experimental data for PSCs based on the MA_2CuCl_4 only exhibited the highest efficiency of 2.41%, with V_{OC}, J_{SC}, and FF of 0.56 V, 8.12 mA/cm^2, and 52%, respectively. Such poor device performance was attributed to the strong recombination in the Cu^{2+}-based solar cells. Further surface passivation and designing of the device structure are essential toward high-performance Cu^{2+}-based solar cells.

The device performance of Bi, Sb, Ge, and Cu-based PSCs are summarized in Table 5. The crystal structure, trap density, absorption, and stability of low-toxicity perovskite materials are summarized in Table 6.

3. LOW-TOXICITY PEROVSKITE MATERIALS FOR NEAR-INFRARED PEROVSKITE PHOTODETECTORS

Near-infrared (NIR) PDs refer to light detectors that can convert NIR optical signal into an electric signal, which usually manifests as a photocurrent. Enormous progress has been made in the field of NIR PDs since the first photomultiplier tube was invented by L. Kubetsky in 1930.[126,127] The NIR PDs have attracted extensive research due to its industrial and scientific applications such as image sensing, environmental monitoring, day- and night-time surveillance, remote control, communications, and chemical/biological sensing.[128,129]

Scheme 2. Schematic of a Typical Vertical Structure PD[a]

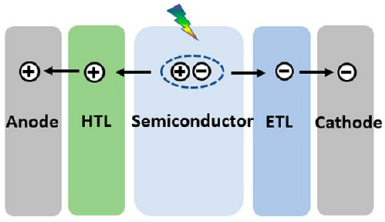

[a]HTL: hole transporting layer. ETL: electron transporting layer.

The general vertical structure of PDs is similar to that used for solar cells (see Scheme 2), in which the semiconductor is sandwiched by charge carrier transporting layers and the electrodes. Under illumination, the photogenerated excitons in semiconductor would be dissociated to holes and electrons, then being transported by the hole transporting layer and electron transporting layer, and finally being collected by the anode and cathode, respectively.

Perovskite materials are one of a promising candidate for next-generation PDs.[15,17,130−142] First, a longer diffusion length guarantees charge carriers can be collected efficiently, which provides high-speed photoresponse and large photogain factors. Second, crystallographic defects in perovskite play a vital role in the dark current; big crystal domains in perovskite will reduce the possibility of charge carrier

https://dx.doi.org/10.1021/acsami.0c02575
ACS Appl. Mater. Interfaces 2020, 12, 26776−26811

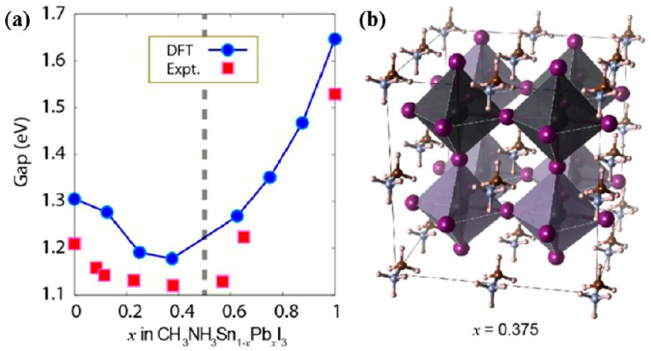

Figure 26. (a) Experimental and calculated band gap evolution of $CH_3NH_3Sn_{1-x}Pb_xI_3$ solid solution as a function of composition x. (b) Crystal structure of $CH_3NH_3Sn_{0.625}Pb_{0.375}I_3$Reproduced with permission from ref 148. Copyright 2015 American Chemical Society.

recombination and therefore suppress leakage current and dark current, which is an essential parameter for PDs.[143] Third, solution-processable perovskite materials can be deposited using spin-coating, spray-casting, or inkjet-printing techniques, which address the need for cost-effective electronics. Furthermore, high film quality and surface morphology can be controlled.

So far, most research efforts on perovskite PDs have been focusing on Pb-based perovskite materials and impressive device performance were reported.[131,144−147] Nevertheless, Pb-based perovskite PDs lack photoresponse in NIR region owing to its limited optical response, which would severely restrict its practical applications.

In the past years, our group made numerous efforts to further extend the photoresponse range from Pb-based perovskite PDs.[15,130,131,142] For example, uncooled ultrasensitive solution-processed broad-band perovskite PDs were achieved by introducing a layer of PbS quantum dots (QDs) upon the $CH_3NH_3PbI_3$ thin film, where PbS QDs acts as a broadband light sensitizer in both the visible and NIR regions, and $CH_3NH_3PbI_3$ acts as the trap state passivation layer. By this strategy, a responsivity (R) over 130 mA/W and a projected detectivity (D^*) exceeding 1×10^{12} Jones (1 Jones = 1 cm $Hz^{1/2}$ W^{-1}) were observed.[131] In addition, we utilized an n-type low-bandgap conjugated polymer, poly[(N, N′-bis(2-octyldodecyl)-1,4,5,8-naphthalene diimide-2,6-diyl) (2,5-dioctyl-3,6-di(thiophen-2-yl) pyrrolo[3,4-c]pyrrole-1,4-dione-5,5′-diyl)] (NDI-DPP) and single-wall carbon nanotubes (SWCNTs) as near-infrared light sensitizer.[15] By forming NDI-DPP:SWCNTs interfaces, wes expected efficient exciton dissociation. As a result, the PDs derived from nanocomposite of Pb-based perovskite, SWCNTs, and NDI-DPP present an EQE of 20%, an R of 150 mA/W, and a D^* of 2×10^{12} Jones in the NIR region (950 nm) at room temperature. All these results indicated that if combined with a strong NIR response photoactive layer, $CH_3NH_3PbI_3$ materials would have huge potentials for NIR PDs.

Very recently, the Pb−Sn mixed perovskite materials attracted much more attention, instead of pure Pb-based perovskite in NIR PDs.[42−44] Kanatzidis' group[148] reported that $CH_3NH_3Sn_{1-x}Pb_xI_3$ displays an anomalous trend in the bandgap with decreasing the compositions approaching $x = 0.5$ showing lower band gaps as shown in Figure 26. Xu et al.[43] recently reported low-cost, solution-processable NIR PDs by adjusting the composition of Pb and Sn with 0.5 and 0.5 wt %, respectively. In terms of the facile oxidization of Sn^{2+} to Sn^{4+}, leading to higher charge carrier density and electrical conductivity, they processed $MA_{0.5}FA_{0.5}Pb_{0.5}Sn_{0.5}I_3$ with an antioxidant additive, ascorbic acid (AA). The oxygen preferred to react with AA additive rather than oxidizing Sn^{2+} because of the strong reduction properties of AA. As a result, AA can retard the Sn^{2+} oxidation in perovskite and reduce Sn vacancy caused by the Sn oxidation. As shown in Figure 27, Sn-containing perovskite ($MA_{0.5}FA_{0.5}Pb_{0.5}Sn_{0.5}I_3$) solar cells displayed an EQE onset at ∼1000 nm, with an EQE of ∼30%, a responsivity of 0.25 A/W, and detectivity of $\sim 2.8 \times 10^{12}$ Jones at ∼920 nm. These results indicated that Sn-based perovskite has enormous potentials in NIR PDs.

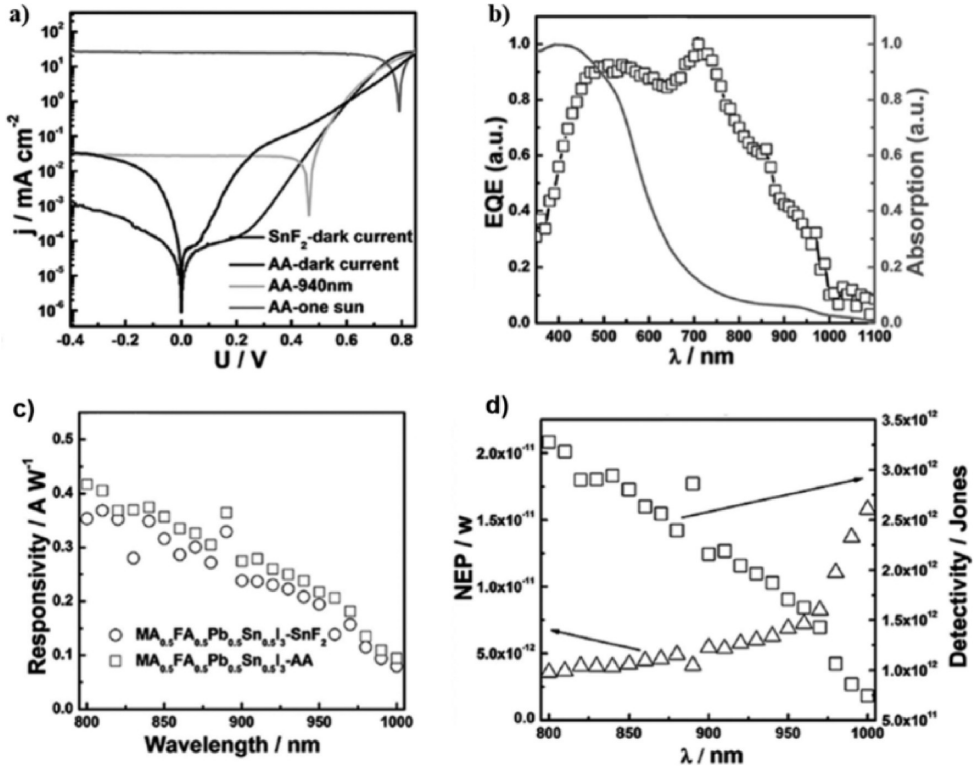

Figure 27. (a) J−V curves of the studied PDs measured in dark and under illumination. (b) Normalized UV−vis absorption spectrum of $MA_{0.5}FA_{0.5}Pb_{0.5}Sn_{0.5}I_3$ film and the EQE of its derived photodetector. (c) Spectral responsivity of the studied PDs and (d) its estimated noise equivalent power (NEP) and the detectivity. Reproduced with permission from ref 43. Copyright 2017 Wiley.

https://dx.doi.org/10.1021/acsami.0c02575
ACS Appl. Mater. Interfaces 2020, 12, 26776−26811

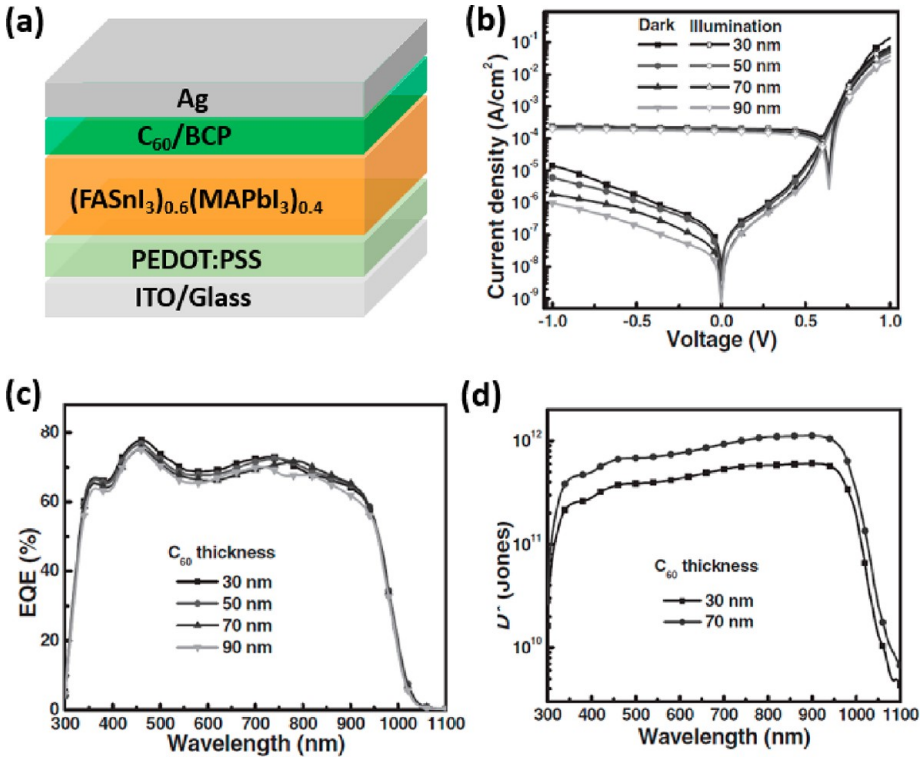

Figure 28. (a) Schematic representation of the device configuration, (b) $J-V$ curves of the PPDs with different thickness of C_{60} layer measured in dark and under white light illumination. (c) EQE spectra. (d) Calculated D^* of the PPDs under −0.2 V bias. PPDs under −0.2 V bias. Reproduced with permission from ref 42. Copyright 2017 Wiley.

Table 7. Recent Advance of Sn/Pb-Based Perovskite PDs

active layer	EQE (max) at λ (nm)	R (A/W) at λ (nm)	D^* (max) in NIR (Jones)	ref
$MA_{0.5}FA_{0.5}Pb_{0.5}Sn_{0.5}I_3$(AA additive)	30/920	0.25/920	2.8×10^{12}/920	43
$(FASnI_3)_{0.6}(MAPbI_3)_{0.4}$(70 nm C60)	~65/900(−0.2 V bias)	~0.6/900(−0.2 V bias)	1.1×10^{12}/900(−0.2 V bias)	42
$FASnI_3$ (200 nm)($SnCl_2$)	NA	1.7×10^5/685(0.5 V)	NA	149
$FASnI_3$ (160 nm)($SnCl_2$)	NA	1.1×10^5/685(0.5 V)	NA	149
$FASnI_3$ (60 nm)($SnCl_2$)	NA	7.3×10^3/685(0.5 V)	NA	149

Similar work was also done by Wang and co-workers.[42] They reported perovskite PDs based on an $(FASnI_3)_{0.6}(MAPbI_3)_{0.4}$ active layer, which exhibited low dark current and broad spectral response from 300 to 1000 nm. As shown in Figures 28a, b, a dark current of ~3.9 nA was successfully observed from Pb−Sn mixed perovskite PDs with a device structure of ITO/PEDOT:PSS/$(FASnI_3)_{0.6}(MAPbI_3)_{0.4}$/$C_{60}$ (70 nm)/BCP/Al, through fine adjusting the thickness of the C_{60} layer. Interestingly, the thickness of C_{60} layer changing from 30 to 90 nm did not affect the EQE values of Pb−Sn mixed perovskite PDs, which are shown in Figure 28c. The optimized Pb−Sn mixed perovskite PDs with a 70 nm thick C_{60} layer yielded high specific D^* of more than 1×10^{11} Jones from 300 to 1000 nm under a −0.2 V bias (Figure 28d).

Different from previous studies, reported NIR PDs were fabricated on the basis of Pb−Sn mixed perovskite materials. Liu et al. reported a high device performance PD based on pure Sn-based perovskite material $FASnI_3$.[149] They introduced a new additive hydroxybenzenesulfonic acid along with excess $SnCl_2$ to encapsulate perovskite grains. The as-prepared pure Sn-based perovskite materials exhibit a broad wavelength region from 300 to 1000 nm, with high hole mobilities and photocarrier density. As a result, a photoresponsivity greater than 1×10^5 A W^{-1} was achieved at a working voltage of 0.5 V. These results indicate that pure Sn-based perovskite materials are also a promising material for high performance PDs. However, PDs using Pb−Sn mixed or pure Sn-based perovskite materials have rarely been reported so far. The reason is possibly similar to that for PSCs: the dark current of Sn-perovskite materials will increase because of the very quick oxidation process, causing poor performance of PDs.

The recent advances in Sn/Pb-based perovskite PDs are summarized in Table 7.

4. LOW-TOXICITY PEROVSKITE MATERIALS FOR LIGHT-EMITTING DIODES

Light-emitting diodes (LEDs) refer to a semiconductor light source that emits light when current flows through, in which the electrons

Scheme 3. Schematic of Working Principle of Light-Emitting Diodes

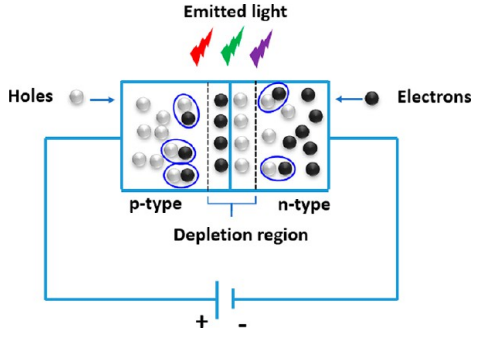

https://dx.doi.org/10.1021/acsami.0c02575
ACS Appl. Mater. Interfaces 2020, 12, 26776−26811

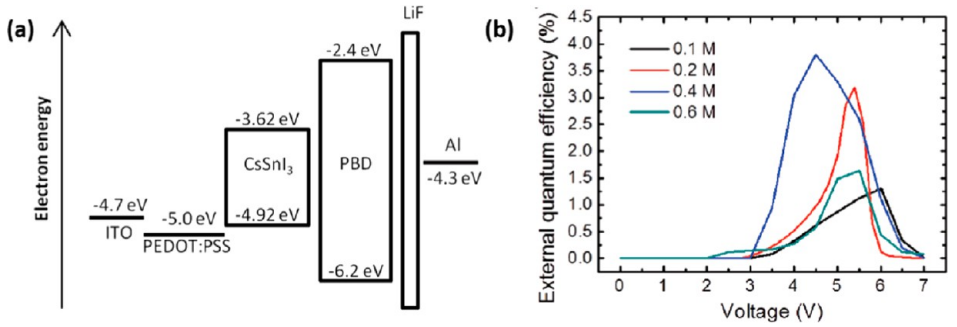

Figure 29. (a) Schematic representation of the band energy-level of materials in perovskite infrared LED. (b) External quantum efficiency of infrared perovskite LEDs synthesized with different precursor concentrations. Reproduced with permission from ref 170. Copyright 2016 Wiley.

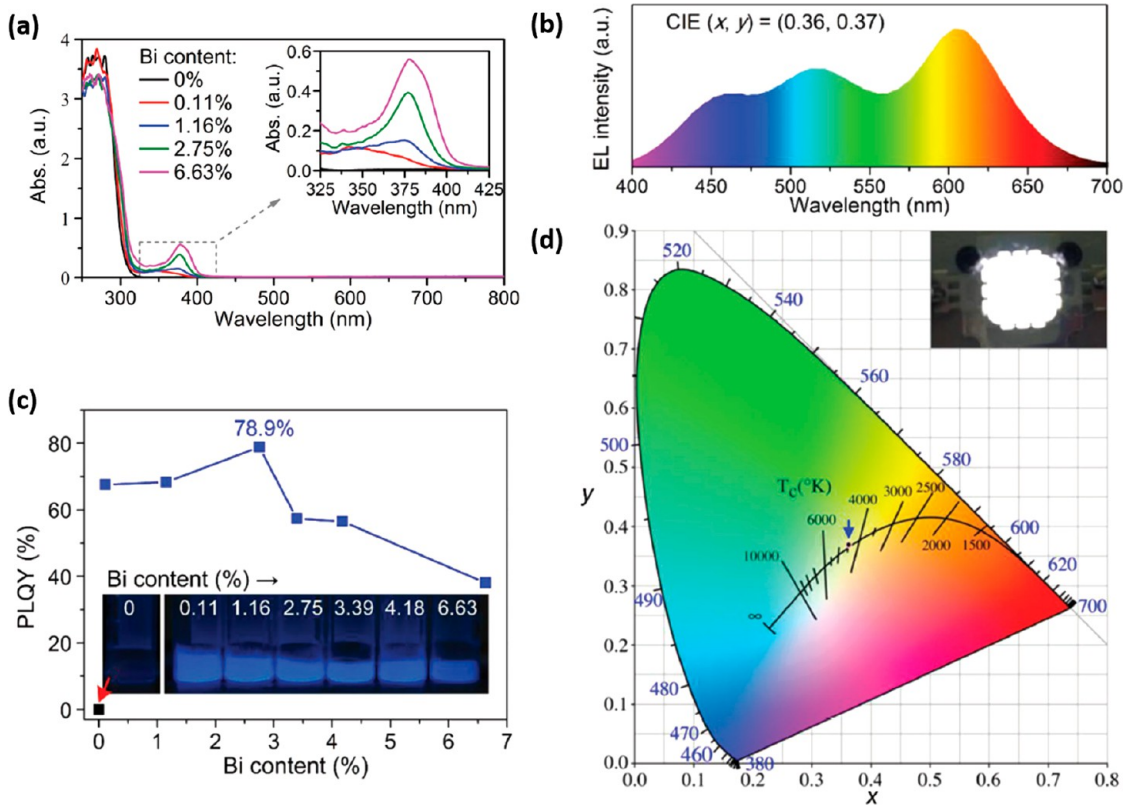

Figure 30. (a) UV−vis absorption spectra of Cs_2SnCl_6:xBi. (b) Room-temperature PLQY of Cs_2SnCl_6 with different concentrations of Bi content. (c) Electroluminescent spectra from Cs_2SnCl_6:2.75% Bi-based LEDs with warm white emission. (d) CIE color coordinates corresponding to white-LED device and (inset) photo of operating LED. Reproduced with permission from ref 156. Copyright 2018 Wiley.

would recombine with holes, releasing energy in the form of photons, as presented in Scheme 3.[150]

Compared with organic and inorganic perovskite materials, all inorganic perovskites with higher thermal stability draw much attention in the fabrication of LEDs.[151] Recently, significant efforts have been made to design all inorganic lead-free metal halide perovskite as potential perovskite LEDs (PeLEDs) materials by replacing Pb^{2+} with Sn^{2+}, Bi^{3+}, and Sb^{3+}.[152−169]

4.1. Sn-Based Perovskite Light-Emitting Diodes. The work reported by Hong and his colleagues triggered intensive investigations on Sn-based PeLEDs.[170] They prepared an infrared PeLEDs by using low-temperature solution-processed $CsSnI_3$ perovskites. They fabricated PeLEDs with a device configuration of ITO/PEDOT:PSS/$CsSnI_3$/PBD/lithium fluoride (LiF) /Al, as indicated in Figure 29a, where PEDOT:PSS was used as the hole injection layer, PBD is 2-(4-*tert*-butylphenyl)-5-(4-biphenylyl)-1,3,4-oxadiazole and served as electron injection layer, LiF and Al were used as cathode. Light emission occurs when injected holes and electrons meet in $CsSnI_3$ active layer. The $CsSnI_3$-based PeLEDs exhibited an electroluminescent (EL) emission band centered at around 950 nm, with a maximum radiance of 10.0 W sr^{-2} m^{-2} and an external quantum efficiency (EQE) of 3.80% at a driven voltage of 4.5 V (Figure 29b).

Similar to Hong's work, Lai et al.[171] demonstrated near-infrared EL from $MASn(Br_{1-x}I_x)_3$ based LEDs, where MA is CH_3NH_3. The $MASn(Br_{1-x}I_x)_3$ based LEDs exhibits tunable emissions from 667 to 945 nm with the structure of ITO/PEDOT:PSS/$MASn(Br_{1-x}I_x)_3$/poly(9,9′-dioctylfluorene) F8/Ca/Ag, where PEDOT:PSS was used as the hole injection layer, F8 layer served important roles in holes blocking layer, reducing electrical shunts and optical field quenching near the cathode. The devices exhibited a radiance of 3.4 W sr^{-1} m^{-2} and a maximum EQE of 0.72%.

In addition to near-infrared EL from Sn-based PeLEDs, Tan et al.[156] fabricated bismuth-doped Cs_2SnCl_6 perovskites with a blue emission at 455 nm and an outstanding PLQY up to 78.9%. As indicated in Figure 30a, the pristine Cs_2SnCl_6 showed an optical absorption sedge at ∼315 nm, which corresponded to the optical

https://dx.doi.org/10.1021/acsami.0c02575
ACS Appl. Mater. Interfaces 2020, 12, 26776−26811

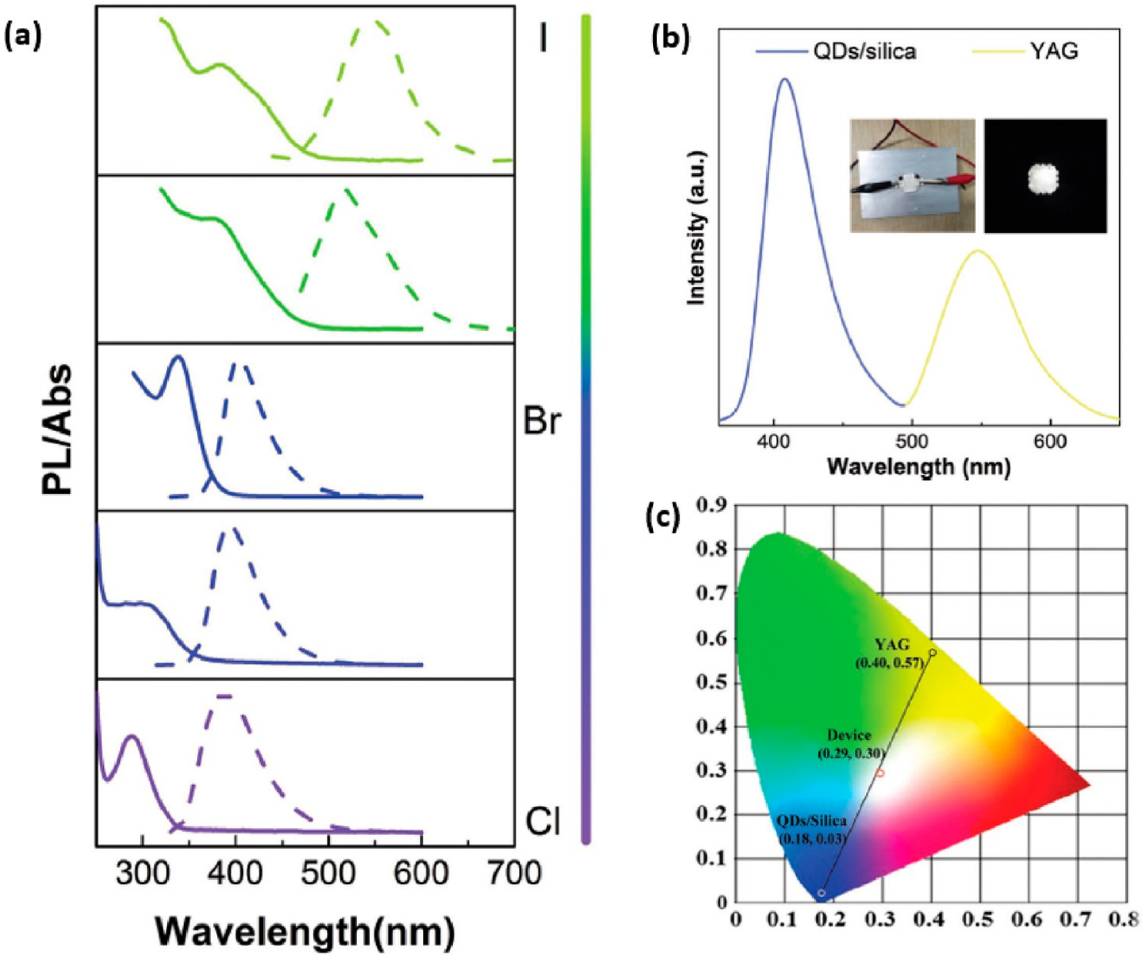

Figure 31. (a) Composition-tunable absorption and PL spectra of various $Cs_3Bi_2X_9$ QDs. (b) EL spectrum of the white LED by combing blue-emissive $Cs_3Bi_2X_9$ QDs and yellow-emissive rare-earth phosphor YAG. Inset: Device images of QD/silica composites combined with YAG (off and on). (c) CIE color coordinates corresponding to $Cs_3Bi_2X_9$ QDs, YAG, and W-LED device. Reproduced with permission from ref 151. Copyright 2018 Wiley.

bandgap of 3.93 eV (black line). An additional absorption peak at around 400 nm due to transitions from defect band to the conduction band of Cs_2SnCl_6 was found by bismuth doping. It was found that the Cs_2SnCl_6:*x*Bi with x = 0.11,1.16, and 2.75% exhibited PLQY values of 67.6, 68.3, and 78.9%, but further increasing the concentration x of Bi resulted in PLQY decreasing (Figure 30b). They further constructed white light-emitting diodes by combing highly stable and efficient blue-emitting Cs_2SnCl_6:Bi perovskite, yellow-emitting $Ba_2Sr_2SiO_4:Eu^{2+}$, red-emitting $CaAlSiN_3:Eu^{2+}$ phosphors, and a 365 nm LED chip. The corresponding EL spectrum was shown in Figure 30c. The commission international de L'Eclarage (CIE) *xy* coordinates of their lead-free perovskite-based white-LED output (0.36, 0.37) refer to a warm white with a correlated color temperature of 4486 K (Figure 31d). All these results indicated that Sn-based perovskites have substantial potential in LED applications.

4.2. Bi-Based Perovskite Light-Emitting Diodes. Compared to Sn-based PeLEDs, $Cs_3Bi_2X_9$ perovskite has an equal or lower than 2D electronic dimension, which leads to creased exciton binding energy and beneficial for high PLQY.[172,173]

Leng et al.[151] reported the synthesis and optical characterization of $Cs_3Bi_2X_9$ perovskite QDs. As shown in Figure 31a, the Pl peak of $Cs_3Bi_2X_9$ perovskite QDs can be easily tuned from 393 to 545 nm by controlling the compositions of halide. They further constructed white light-emitting diodes by combing blue-emitting $Cs_3Bi_2Br_9$ perovskite QDs and yellow-emitting $Y_3Al_5O_{12}$ (YAG) with violet-emissive GaN chips. The corresponding EL spectrum was shown in Figure 31b. There are two peaks located at 407 and 551 nm, which were related to $Cs_3Sn_2Bi_9$ perovskite QDs and yellow-emitting YAG, respectively. The CIE color coordinates of (0.29, 0.30) corresponding to their white LED as indicated in Figure 31c. In addition, they reported that their white LED still shows 68% of the initial EL intensity as it was heated at 60 °C for 15 h.

In addition to $Cs_3Bi_2X_9$ perovskite QDs, Bi-based perovskite nanocrystals (NCs) or double perovskite NCs also show a promising candidate for PeLED applications in recent studies.[174−178] Xie et al.[175] reported new Bibased perovskite NCs with the formula of $Rb_7Bi_3Cl_{16}$ by a hydrothermal method. They found that the $Rb_7Bi_3Cl_{16}$ NCs possess superior thermal and moisture stability and the PL peak was located in 478 nm with a full width at half-maximum (fwhm) of 93 nm and a PLQY of 28.43%. Yang and his colleagues found that the indirect bandgap of double perovskite $Cs_2AgBiCl_6$ can be easily tuned to a direct bandgap by doping indium.[178] The PLQY of indium-doped $Cs_2AgBiCl_6$(36.6%) is more than 5 times higher than that of pristine $Cs_2AgBiCl_6$ (~7%).[178]

4.3. Sb-Based Perovskite Light-Emitting Diodes. In terms of all in organic Sb-based perovskite materials $Cs_3Sb_2X_9$, their thin films showed a high absorption coefficient (>1 × 10^5/cm), high PLQY values, nearly direct bandgap and better stability, giving Sb-based perovskite huge potential in LED applications.[179]

In the recent work reported by Zhang and his colleagues,[180] they successfully synthesized $Cs_3Sb_2Br_9$ QDs by a simple ligand-assisted reprecipitation method, as displayed in Figure 32a. By further controlling the crystallization of QDs, they found that the PLQY of $Cs_3Sb_2Br_9$ QDs were in the range of 20−46%, which indicated that the suppression of nonradiative recombination happened. They assumed that the enhanced PLQYs were also related to the richness

https://dx.doi.org/10.1021/acsami.0c02575
ACS Appl. Mater. Interfaces 2020, 12, 26776−26811

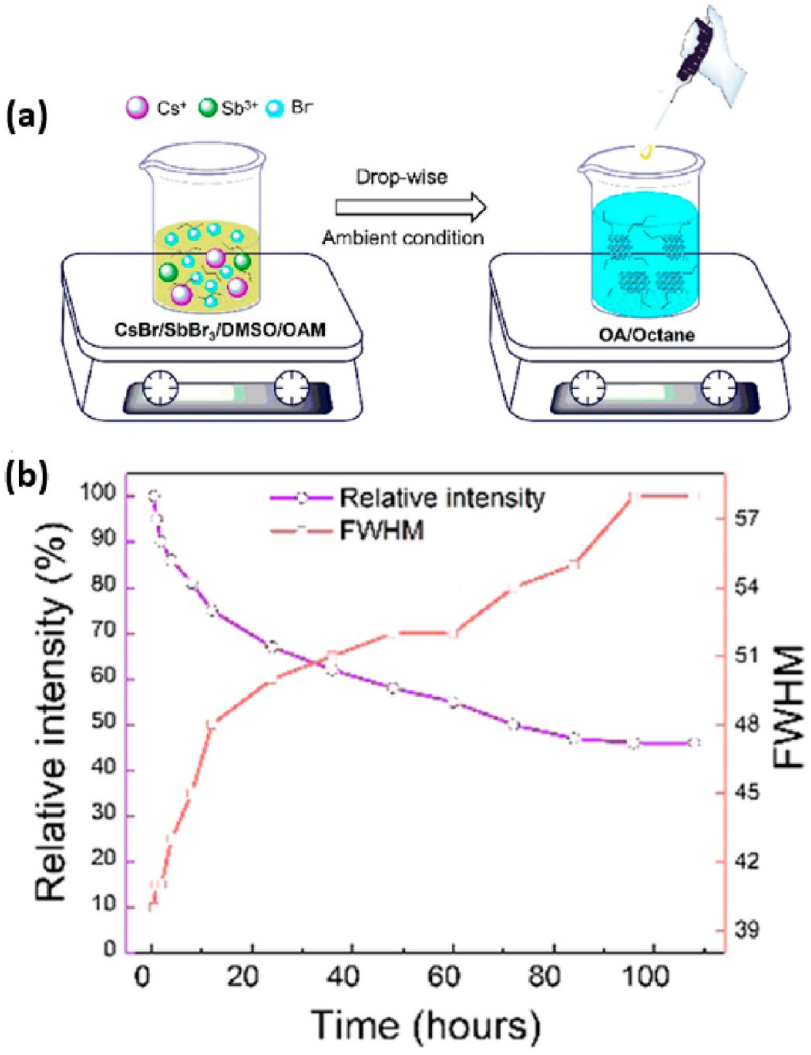

Figure 32. (a) Schematic representation of the reaction system for modified ligand-assisted reprecipitation. (b) Photostability test of $Cs_3Sb_2Br_9$ QDs. Reproduced with permission from ref 180. Copyright 2017 American Chemical Society.

Table 8. Recent Advance of Low-Toxicity PeLEDs

device structures	CIE color coordinates (x, y)	EL. peak (nm)	EQE (%)	luminescence	refs
UV LED/Cs_2SnCl_6:Bi/$Ba_2Sr_2SiO_4$:Eu^{2+}/$GaAlSiN_3$:Eu^{2+}	(0.36, 0.37)	~350	NA	NA	156
ITO/PEDOT:PSS/$CsSnI_3$/PBD/LiF/Al	NA	950	3.80	40.0 W $sr^{-1}m^{-2}$	170
ITO/PEDOT:PSS/MASn(Br/I)$_3$/F8/Ca/Ag	NA	667−945	0.72	3.4 W $sr^{-1}m^{-2}$	166
glass/ITO/LiF/$CsSnBr_3$/LiF/ZnS/Ag	NA	672	0.34	172 cd m^{-2}	167
ITO/PEDOT:PSS/PEA_2SnI_4/TPBi/LiF/Al	NA	629	0.16	58 cd m^{-2}	168
ITO/PEDOT:PSS/TEA_2SnI_4/TPBi/LiF/Al	(0.695, 0.305)	638	0.62	322 cd m^{-2}	168
$(C_{18}H_{35}NH_3)_2SnBr_4$/YAG:$Ce^{3+}$/UV LED chip	(0.488, 0.415)	600	NA	NA	169
$Cs_3Bi_2Br_9$/YAG/GaN chips	(0.29, 0.30)	407, 551	NA	NA	151
glass/ITO/PEDOT:PSS/layer-$Cs_3Sb_2I_9$/TPBi/LiF/Al	NA	~780	1×10^{-8}	0.012 W $sr^{-1}m^{-2}$	173

[a]TPBi: 2,2′,2″-(1,3,5-benzenetriyl)tris(1-phenyl-1-H-benzimidazole; YAG: $Y_3Al_5O_{12}$. LiF: lithium fluoride.

of Br and organic ligand on the $Cs_3Sb_2Br_9$ QDs surface.[180] The photostability test of $Cs_3Sb_2Br_9$ QDs was also studied and the results are shown in Figure 32b. It was found that the relative PL intensity of $Cs_3Sb_2Br_9$ QDs still kept 50% of its initial value after 108 h irradiation. All these results indicated that $Cs_3Sb_2Br_9$ QDs have great potentiald in the application of LEDs.

It should be noted that the synthetic method plays an important role in PLQY performance of $Cs_3Sb_2Br_9$ QDs. For example, Ma et al.[181] did similar works as Zhang's work, but with a different synthetic method. They prepared $Cs_3Sb_2Br_9$ QDs according to supersaturated recrystallization at a low processing temperature of 50 °C. The highest PLQY observed from $Cs_3Sb_2Br_9$ QDs was 51.2% and the average PLQY was 49.3% with an error deviation of 10.2%, which was much higher than the work reported by Zhang and his co-workers.[180]

Low-toxicity PeLEDs have been developed rapidly in recent years, but the performance was far inferior for commercial applications. Future efforts should be focused on increasing PLQY by metal ion doping and defect passivation with different ligands. The device performance of different low-toxicity PeLEDs is summarized in Table 8.

https://dx.doi.org/10.1021/acsami.0c02575
ACS Appl. Mater. Interfaces 2020, 12, 26776−26811

5. LOW-TOXICITY PEROVSKITE MATERIALS FOR THERMOELECTRIC DEVICES

Thermoelectric (TE) electrics are the device made by thermoelectric materials that can convert heating into electrical energy, as presented in Scheme 4.[46,182−185]

Scheme 4. Schematic of Seebeck Effect[a]

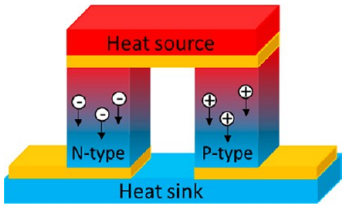

[a]Reproduced with permission from ref 183. Copyright 2018 Materials.

Scheme 5. Interdependent Relationship of the Seebeck Coefficient, Electrical Conductivity, and Thermal Conductivity, and the Strategies to Decouple Their Interdependency[a]

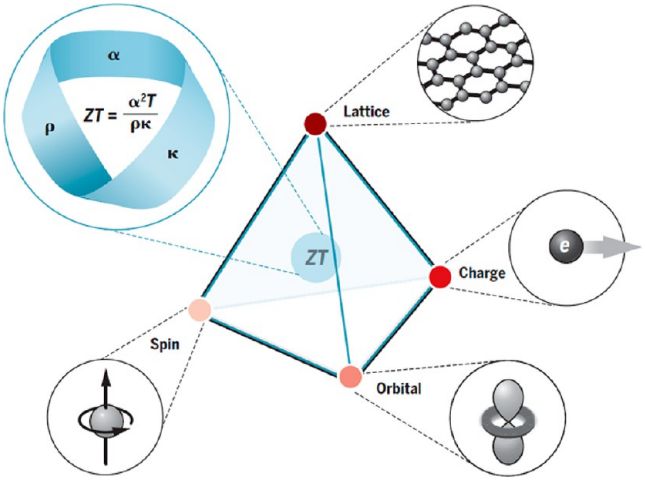

[a]Reproduced with permission from ref 182. Copyright 2017 American Association for the Advancement of Science.

The TE materials are evaluated by the dimensionless figure of merits ZT, which determines the maximum TE energy conversion efficiency:[46,184]

$$\eta = \left(\frac{T_{hot} - T_{cold}}{T_{hot}}\right)\left[\frac{\sqrt{ZT} - 1}{\sqrt{ZT} + \left(\frac{T_{cold}}{T_{hot}}\right)}\right] \quad (1)$$

where T_{hot} is the temperature at hot junction and T_{cold} is the temperature at the surface being cooled. The ZT is defined as

$$ZT = \frac{S^2\sigma}{k}T \quad (2)$$

$$\sigma = e(n_e\mu_h + n_h\mu_h) \quad (3)$$

where S (V/K) is the Seebeck coefficient, σ (S/m) is the electrical conductivity, k (W/(m K)) is the thermal conductivity, T (K) is absolute temperature, e is an elementary charge, n_e and n_h are charge carrier concentrations of electrons and holes, respectively, μ_e and μ_h are charge carrier mobilities of electrons and holes. Therefore, to boost the TE performance, semiconductors should have high Seebeck coefficients and electrical conductivities (the charge carrier and mobility), but low thermal conductivities.

Several groups have shown that Pb-free perovskites can function as thermoelectric materials because of their high electrical conductivity and low thermal conductivity.[186−190]

In Sn-based perovskites, there is a facile tendency toward oxidation, which causes the materials to be doped with Sn^{4+} and thus behave as p-type semiconductors. The quick oxidation of Sn^{2+} will generate large leakage current that is averse to the solar cells (induce a low shunt resistance) or PDs (induce a high dark current) performance. However, the oxidation will increase charge carriers, resulting in higher electrical conductivity. Based on eqs 2 and 3, and the interdependent relationship of the Seebeck coefficient and the electrical conductivity as shown in Scheme 5, the oxidized Sn-based perovskite materials with high electrical conductivity can possibly be a candidate for TE materials.

Stoumpos. et al.[187] studied the thermoelectric properties of $CH_3NH_3MI_3$ (M = Pb, Sn) thin films. As shown in Figure 33, they performed Seebeck coefficient measurements of $HC(NH_2)_2SnI_3$ and $CH_3NH_3PbI_3$ single-crystals and found that the thermopower of both samples in the 300−400 K range, are negative and very large in magnitude, indicating that materials are n-type semiconductors, which were presented in Figures 33b, d, respectively. They also investigated the polycrystalline pellets of $CH_3NH_3SnI_3$, $HC(NH_2)_2SnI_3$, $CH_3NH_3PbI_3$, and $HC(NH_2)_2PbI_3$ and found that Sn-based polycrystalline materials exhibited significantly lower Seebeck coefficients compared with Pb-containing samples, indicating a higher charge carrier concentration with respect to the Pb analogs.

Similar work was also reported by Mettan and his colleagues.[188] They found that ZT only reached a value of 1×10^{-9} in dark for $MAPbI_3$ materials. However, its electrical conductivity was increased dramatically but ZT still remained low value after the photoinduced doping process. These results indicated that the doping process in $MAPbI_3$ was not sufficient for thermoelectric application. In contrast, the ZT value of $MASnI_3$ exhibited approximately five magnitudes higher than that of $MAPbI_3$, which was illustrated in Figure 34. In their work, it was assumed that the ZT value could be increased to unity for $MASnI_3$ with suitable doping. Thus, to dope $MASnI_3$ will be a route for future research.

Recently, we reported thermoelectric performance of Sn-based perovskite materials through a chemical doping of 2,3,5,6-tetrafluoro-7,7,8,8-tetracyanoquinodimethane (F4-TCNQ) into $FASnI_3$ thin films.[189] Systemically studies demonstrate that enhanced electrical conductivities are attributed to increased charge carrier concentrations and mobilities, as well as superior film morphologies. The quantitative thermal conductivity scanning thermal microscopy studies reveal that the F4-TCNQ doped $FASnI_3$ thin films exhibit ultralow (~0.200 ± 0.014 W m^{-1} K^{-1}) thermal conductivity. Moreover, a Seebeck coefficient of ~310 μV K^{-1}, a power factor of over 130 μW m^{-1} K^{-2} and a ZT value of 0.19 at room temperature from the F4-TCNQ-doped $FASnI_3$ thin films are also reported.[189] All these results demonstrate that our studies open a door for potential applications of cost-effective less-toxic hybrid perovskite materials on heat-to-electricity conversion at room temperature.

Liu et al.[190] reported an electrical conductivity of 3.6×10^3 S cm^{-1} and a Seebeck coefficient of 70 μV K^{-1} at room temperature from $C_6H_4NH_2CuBr_2I$ thin film. The electrical conductivity was boosted by utilizing defect-related heavy doping (Cu^+) to substitute B-site. The improved Seebeck coefficient was attributed to the coexisting entropy difference and polarization difference. By studying the temperature dependence of the Seebeck coefficient, it was proved that $C_6H_4NH_2CuBr_2I$ sample behaving like metallic originated from the self-electron doping process, as demonstrated in Figure 35c. It was found that the major charge carrier in $C_6H_4NH_2CuBr_2I$ were electrons (Figure 35d). Thus, an extremely high-power factor (1900 μW mK^{-1}) observed from $C_6H_4NH_2CuBr_2I$ indicates that $C_6H_4NH_2CuBr_2I$ possesses great potential as an n-type thermoelectric material.

https://dx.doi.org/10.1021/acsami.0c02575
ACS Appl. Mater. Interfaces 2020, 12, 26776−26811

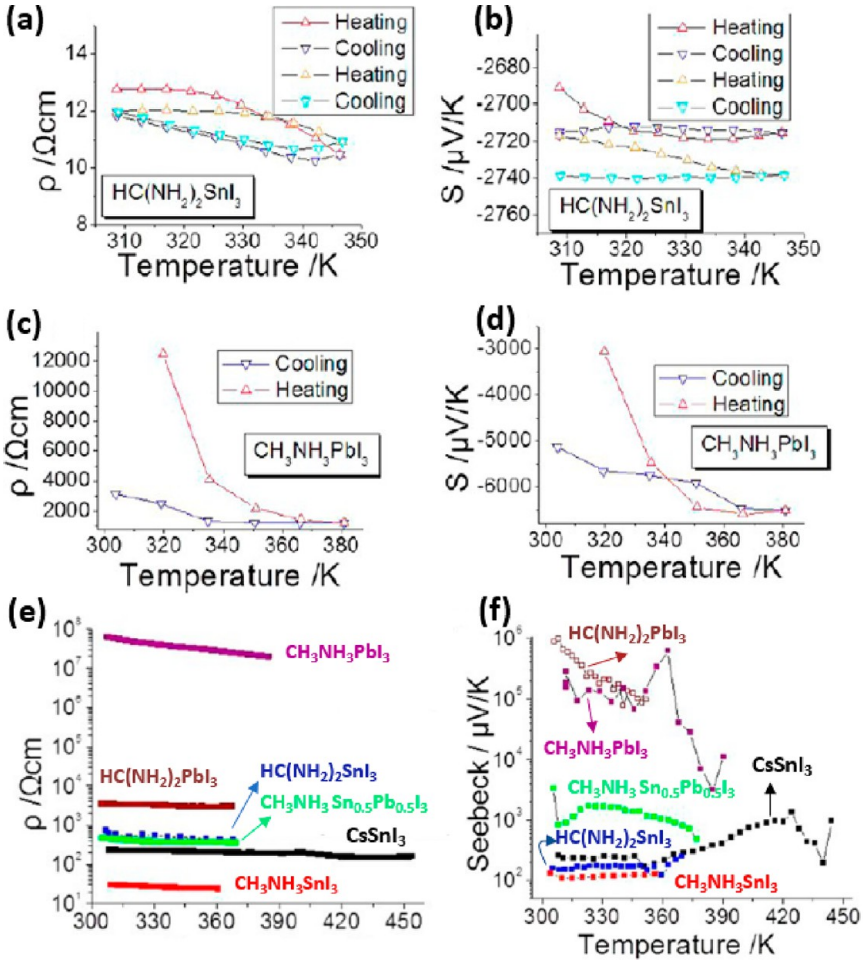

Figure 33. Temperature dependence of the Seebeck coefficients on single-crystals of $HC(NH_2)_2SnI_3$ and $CH_3NH_3PbI_3$. The respective resistivity values are given for reference in panels a and c. (e) Resistivity and (f) Seebeck coefficients on cold-pressed pellets of annealed polycrystalline samples. (Reproduced with permissionfrom ref 187. Copyright 2013 American Chemical Society.

6. CONCLUSIONS AND FUTURE PROSPECTS

In short, the developments in low-toxicity and/or Pb-free PSCs, PDs as well as thermoelectric performance are highlighted. By taking consideration of environmental impact, Pb-free (or Pb-less) perovskites possess a lower content of toxic, which may eventually provide a large-scale implementation in future industrial applications.

In studies of Pb-free (or Pb-less) PSCs, Sn, as the most important substitution species, has been demonstrated to exhibit high efficiency in recent works.Because of the low bandgap property, Sn-based PSCs usually possesses highly generated photocurrent. However, Sn-based PSCs face from natural fast crystallization process and oxidation induced "self-doping". Therefore, to find a solution addressing those two issues is an ongoing major investigation area in Sn-based perovskites. One is to introduce the process additive into the precursor solution. Several additives with better properties that are applied to enhance the quality of Sn-based perovskite thin film. But, the role of additives as well as the effect of binary reducing additives, which may assist in forming a better-quality perovskite thin film needs to be carefully investigated. Another solution is to synthesize low-dimensional perovskite materials for tuning the rate of nucleation and crystal growth in Sn-based perovskite thin film. The corporation between high-quality agents and low dimensional Sn-based perovskite materials would be efficiently approaches in future research. Besides, composition engineering (in both A site and B site) is a promising strategy to modify the energy condition of Sn-based perovskite. Aside from material modification, the novel fabrication process should also be taken into consideration. Compared to pure Sn-based perovskite materials, the Pb−Sn mixed perovskite materials exhibit not only smoother surface and enhanced crystallinity, but also an ultrahigh J_{SC} (~28 mA/cm^2).[191] Efforts now should be focused on enhancing V_{OC} toward 1.0 V by tuning halide.

The Bi element is dramatically stable at +3 valence state in the atmosphere compared to Sn^{2+}, but the thin film exhibits nonuniformly with island morphology. The antisolvent assisted crystallization process and two-step BiI_3 salt evaporation technique are effective strategies to address the above issues. However, it is more challenging to form a high-quality Bi-based perovskite thin film with fewer defects and pinholes than a Pb-based perovskite thin film.[114] To facilitate the feasibility of Bi-based perovskite materials in PSCs, further improvements should be focused on improving mobility and reducing trap density in Bi-based perovskite materials.

Double perovskite materials have been investigated in the last two years. However, PCEs observed from these materials were poor. The main reasons were the recombination process happened in a very short time and nonuniform crystals generate uncovered thin film, resulting in limited J_{SC}. Thus,

https://dx.doi.org/10.1021/acsami.0c02575
ACS Appl. Mater. Interfaces 2020, 12, 26776−26811

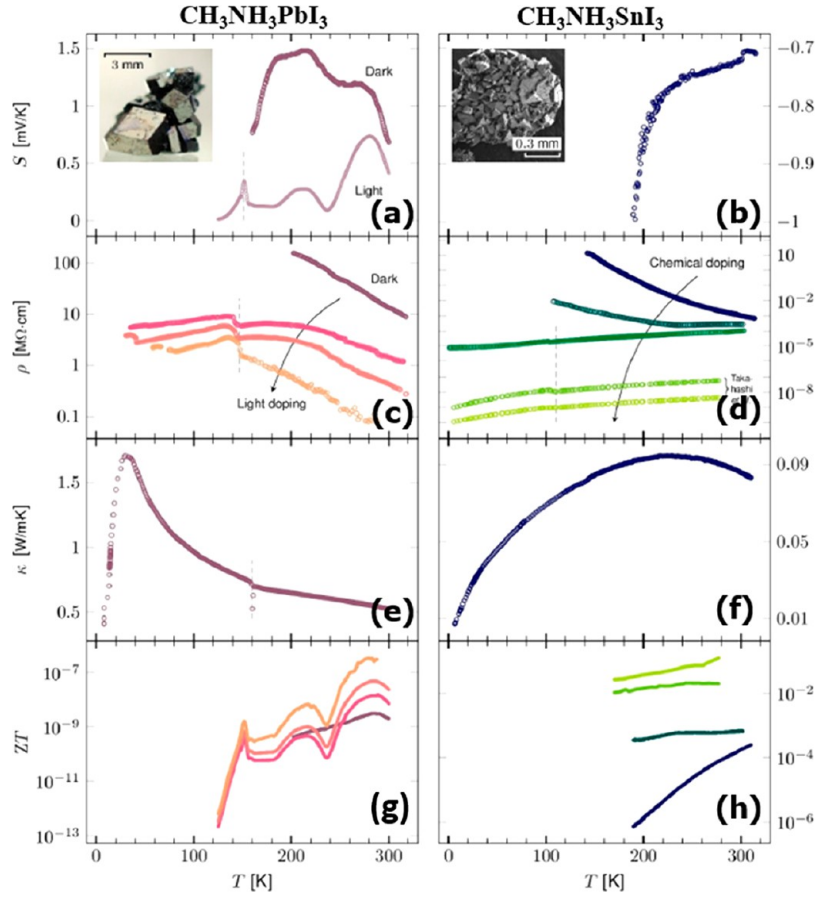

Figure 34. From top to bottom: thermoelectric power, S; electrical resistivity, ρ; thermal conductivity, κ; and figure of merit, ZT, of $CH_3NH_3PbI_3$ [(a), (c), (e), (g), respectively] and $CH_3NH_3SnI_3$ [(b), (d), (f), (h), respectively] for light (photoelectron) and impurity doping. The three curves of $MAPbI_3$, red, orange, and yellow correspond to light intensities of 80, 165, and 220 mW/cm^2. κ of $MAPbI_3$. Reproduced with permission from ref 188. Copyright 2015 American Chemicaly Society.

future research should focus on surface passivation to reduce the surface traps and realize the long carrier lifetimes for their application in efficient PSCs.

Ge- and Sb-based perovskite show structural instabilities due to spontaneous oxidation. Future research in Ge-based PSCs can be performed along three directions: First, designing the band suitable hole and electron transporting layer to facilitate charge extraction. Second, it has been proved that adding an antioxidation additive can efficiently suppress the oxidation process of Ge-based perovskite solar cells. Thus, the high oxidization tendency of Ge-based perovskite might be addressed by blending with antioxidation additives. Finally, the doping process was widely used to tune the electrical properties of the perovskite solar cell. Higher efficiency Ge-based perovskite solar cells might be achieved via doping inequivalent rare-earth element. The Sb-based PSCs can be created by designing the band suitable hole and electron transporting layer to facilitate charge extraction, as well as by adding an antioxidation additive that can efficiently suppress the oxidation process.

Recent results indicate that Cu-based PSCs are particularly interesting for low-toxicity PSCs, but tremendous work needs to be done to improve device performance of Cu-based PSCs, such as reducing the bandgap, balancing charge carriers mobilities, enhancing exciton diffusion length, designing device structures, and exploring new fabrication methods.

The ultimate challenge for low-toxicity PSCs is to achieve stable devices and solve long-term stability issues. Four strategies to address the poor stability of low-toxicity PSCs are considered. Low-toxicity perovskite materials are treated by additives and/or coadditives, and to replace organic cation in low-toxicity perovskite materials. Both above two methods have been well discussed above. The third approach is to introduce the functional group from polymer into perovskite precursor, which probably could boost the stability of low-toxicity perovskite materials. For example, Liu et al.[192] introduced a polymer [poly(ethylene-*co*-vinyl acetate) (EVA)] into antisolvent during spin coating of $FASnI_3$ precursor solution, the C = O group on the molecule interacts with Sn^{2+} by Lewis acid coordination, which can greatly stabilize the $FASnI_3$ structure. By this strategy, the devices maintained over 90% of its original efficiency with 800 h of storage in nitrogen glove. The fourth approach is to form 2D/3D structure. For example, the work was done by Chen et al.[193] They introduced a polymer N-(3-aminopropyl)-2-pyrrolidinone (NAP) into the $CH_3NH_3Sn_{0.5}Pb_{0.5}I_xCl_{3-x}$ thin film, the carbonyl group interacts with Sn^{2+}/Pb^{2+}, forming vertically oriented 2D layered perovskite. The device based on $CH_3NH_3Sn_{0.5}Pb_{0.5}I_xCl_{3-x}$ treated by 0.144 M NAP thin film exhibited 90% of its initial performance over 1 month as it was stored in ambient condition.

For PDs systems, by replacing the Pb element with the Sn element, the bandgap was reduced from ∼1.40 to ∼1.17 eV,

https://dx.doi.org/10.1021/acsami.0c02575
ACS Appl. Mater. Interfaces 2020, 12, 26776−26811

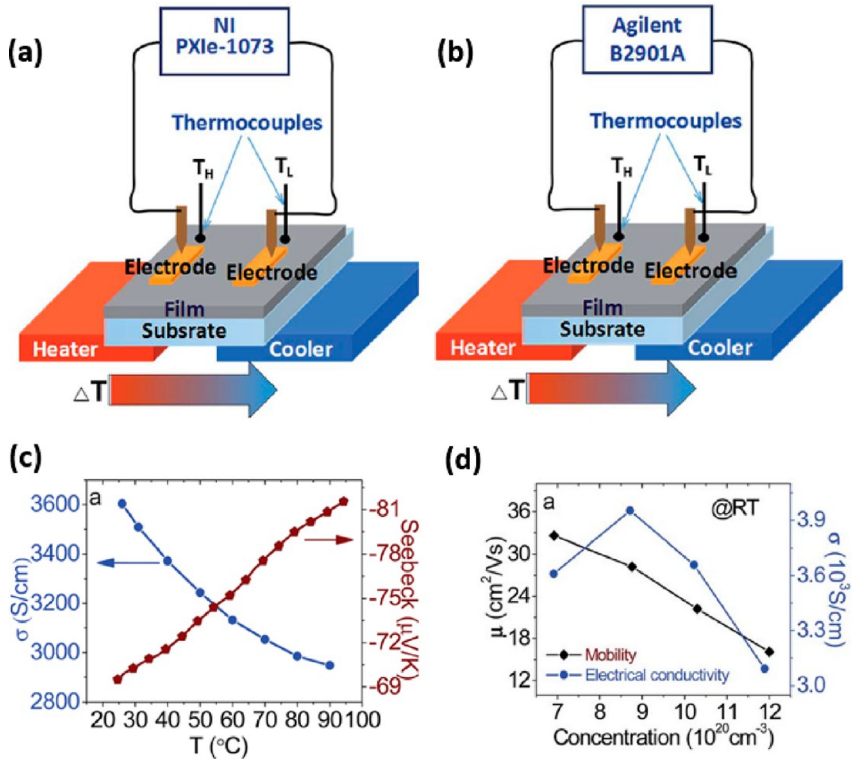

Figure 35. Schematic diagram of measurements for the Au/$C_6H_4NH_2CuBr_2I$/Au sample: (a) thermoelectric voltage (VTE) and (b) thermoelectric current (ITE) at different DT. (c) Temperature dependence of electrical conductivity and Seebeck coefficient. (d) Carrier concentration dependence of the mobility and electrical conductivity. Reproduced with permission from ref 190. Copyright 2017 Royal Society of Chemistry.

resulting in a wider range of spectral response. High EQEs (over 60% at 900 nm) in the NIR region has been demonstrated by Pb−Sn mixed perovskite PDs, which indicates that Pb−Sn mixed perovskites have huge potential in NIR PDs. However, significant efforts are still required for achieving commercialization of PDs. For example, the reduction of the number of interfacial trap states is crucial to achieve high response speed (the charge carriers would experience less-trap and detrap process if the trap states are suppressed). Thus, surface passivation between perovskite and charge transport layers, utilization of Lewis acid and/or Lewis base to passivate PbX^{3-} and/or Pb^{2+} antisite defects and synthesis of Pb−Sn mixed perovskite single crystals (no grain boundary effect) are crucial importance to reduce trap states. In addition, the ion-migration effect is also one of the most significant issues in Pb−Sn mixed perovskite PDs. The ion migration, such as iodine migration in Pb−Sn mixed perovskite PDs would induce an electric field with opposite direction to the built-in electric field, which results in a reduced collection of photogenerated charge carriers (the built-in electric field is partially screened). Therefore, introduction of hydrogen bonds with perovskite[9] or surface passivation[56] is suggested to reduce the ion-migration effect in Pb−Sn mixed perovskite PDs. In terms of detectivity, further reducing the dark current is important for improved detectivity of Pb-free perovskite PDs. To minimize the dark current in Pb−Sn mixed perovskite PDs, the general concepts are to prepare a blocking layer between charge carriers transporting layer and the electrode. It should be noted that avoiding the oxidation process by additives is also essential to suppress dark current in Pb−Sn mixed perovskite based PDs.

For LED applications, great efforts have been dedicated on lead-free PeLEDs, including Sn^{2+}, Sn^{4+}, Bi^{3+}, and Sb^{3+}-based perovskite materials.[152−162,167] Among them, halide perovskite nanocrystals exhibit unique optical properties as LEDs materials since the defect states of halide perovskite nanocrystals are formed within the conduction or valence band, resulting in trap states free within the bandgap.[52] Therefore, the PLQY of halide perovskite nanocrystal is relatively high without surface passivation. So far, the synthesis of lead-free perovskite nanocrystals has been explored significantly. The future effects should be focused on both theoretical and experimental studies on photophysical processes in lead-free perovskite nanocrystals. Specifically, the nature of the nonradiative recombination process in lead-free perovskite nanocrystals must be well studied. Moreover, the greatest challenge from moisture and light degradation of these materials has to be solved. Once these two stages are passed, the efforts of device engineers should be focused on increasing PLQY by metal ion doping and defect passivation with different ligands.

For thermoelectric applications, the suitable energy band gaps and impressively high carrier mobilities of $MASnI_3$ perovskite materials indicate Sn-based perovskite materials can be a promising candidate for TE application. In future research, chemical doping processes could provide an effective way to boost the charge carrier density of Sn-based perovskite. Band-engineering and nanoengineering can be applied to $MASnI_3$ perovskite materials to further improve TE properties. The serious challenge for $MASnI_3$ materials in thermoelectric applications is long-term stability, which comes from the competition between the enhanced charge carrier concentration from self-doping and degradation caused by air exposure. Therefore, achieving a favorable Goldschmidt

https://dx.doi.org/10.1021/acsami.0c02575
ACS Appl. Mater. Interfaces 2020, 12, 26776−26811

tolerance in $MASnI_3$ structure by adding reductant is highly recommended. In addition, the A site composition engineering (replacing MA^+ with Cs^+) is a promising strategy to improve the thermal stability of Sn-based perovskites.

AUTHOR INFORMATION

Corresponding Author

Xiong Gong − *Department of Polymer Engineering, College of Polymer Science and Polymer Engineering, The University of Akron, Akron, Ohio 44325, United States;* orcid.org/0000-0001-6525-3824; Email: xgong@uakron.edu; Fax: (330) 9723406

Authors

Tao Zhu − *Department of Polymer Engineering, College of Polymer Science and Polymer Engineering, The University of Akron, Akron, Ohio 44325, United States*

Yongrui Yang − *Department of Polymer Engineering, College of Polymer Science and Polymer Engineering, The University of Akron, Akron, Ohio 44325, United States*

Complete contact information is available at: https://pubs.acs.org/10.1021/acsami.0c02575

Notes

The authors declare no competing financial interest.

ACKNOWLEDGMENTS

The authors acknowledge the National Science Foundation (ECCS/EPMD1903303) and Air Force Office of Scientific Research (FA9550-15-1-0292) for financial support.

REFERENCES

(1) Wang, K.; Zheng, L.; Zhu, T.; Yao, X.; Yi, C.; Zhang, X.; Cao, Y.; Liu, L.; Hu, W.; Gong, X. Efficient Perovskite Solar Cells by Hybrid Perovskites Incorporated with Heterovalent Neodymium Cations. *Nano Energy* **2019**, *61*, 352−360.

(2) Yin, W.-J.; Yang, J.-H.; Kang, J.; Yan, Y.; Wei, S.-H. Halide Perovskite Materials for Solar Cells: A Theoretical Review. *J. Mater. Chem. A* **2015**, *3* (17), 8926−8942.

(3) Saski, M.; Prochowicz, D.; Marynowski, W.; Lewiński, J. Mechanosynthesis, Optical, and Morphological Properties of MA, FA, Cs-SnX_3 (X= I, Br) and Phase-Pure Mixed-Halide $MASnI_xBr_{3-x}$ Perovskites. *Eur. J. Inorg. Chem.* **2019**, *2019*, 2680−2684.

(4) Prochowicz, D.; Saski, M.; Yadav, P.; Grätzel, M.; Lewiński, J. Mechanoperovskites for Photovoltaic Applications: Preparation, Characterization, and Device Fabrication. *Acc. Chem. Res.* **2019**, *52*, 3233−3243.

(5) Park, N.-G. Perovskite Solar Cells: An Emerging Photovoltaic Technology. *Mater. Today* **2015**, *18*, 65−72.

(6) Xiang, W.; Tress, W. Review on Recent Progress of All-Inorganic Metal Halide Perovskites and Solar Cells. *Adv. Mater.* **2019**, *31*, 1902851.

(7) Kojima, A.; Teshima, K.; Shirai, Y.; Miyasaka, T. Organometal Halide Perovskites as Visible-Light Sensitizers for Photovoltaic Cells. *J. Am. Chem. Soc.* **2009**, *131*, 6050−6051.

(8) https://www.nrel.gov/pv/assets/pdfs/best-research-cell-efficiencies.20190802.pdf.

(9) Wang, K.; Zheng, L.; Zhu, T.; Liu, L.; Becker, M. L.; Gong, X. High Performance Perovskites Solar Cells by Hybrid Perovskites Co-Crystallized with Poly (ethylene oxide). *Nano Energy* **2020**, *67*, 104229.

(10) Sum, T. C.; Mathews, N. Advancements in Perovskite Solar Cells: Photophysics behind the Photovoltaics. *Energy Environ. Sci.* **2014**, *7*, 2518−2534.

(11) Stranks, S. D.; Eperon, G. E.; Grancini, G.; Menelaou, C.; Alcocer, M. J.; Leijtens, T.; Herz, L. M.; Petrozza, A.; Snaith, H. J. Electron-Hole Diffusion Lengths Exceeding 1 Micrometer in an Organometal Trihalide Perovskite Absorber. *Science* **2013**, *342*, 341−344.

(12) Liu, C.; Wang, K.; Yi, C.; Shi, X.; Smith, A. W.; Gong, X.; Heeger, A. J. Efficient Perovskite Hybrid Photovoltaics via Alcohol-Vapor Annealing Treatment. *Adv. Funct. Mater.* **2016**, *26*, 101−110.

(13) Xiao, Z.; Meng, W.; Wang, J.; Mitzi, D.; Yan, Y. Searching for Promising New Perovskite-Based Photovoltaic Absorbers: The Importance of Electronic Dimensionality. *Mater. Horiz.* **2017**, *4* (2), 206−216.

(14) Yin, W. J.; Shi, T.; Yan, Y. Superior Photovoltaic Properties of Lead Halide Perovskites: Insights from First-Principles Theory. *J. Phys. Chem. C* **2015**, *119* (10), 5253−5264.

(15) Xu, W.; Guo, Y.; Zhang, X.; Zheng, L.; Zhu, T.; Zhao, D.; Hu, W.; Gong, X. Room-Temperature-Operated Ultrasensitive Broadband Photodetectors by Perovskite Incorporated with Conjugated Polymer and Single-Wall Carbon Nanotubes. *Adv. Funct. Mater.* **2018**, *28* (7), 1705541.

(16) Zheng, L.; Wang, K.; Zhu, T.; Liu, L.; Zheng, J.; Gong, X. Solution-Processed Ultrahigh Detectivity Photodetectors by Hybrid Perovskite Incorporated with Heterovalent Neodymium Cations. *ACS Omega* **2019**, *4* (14), 15873−15878.

(17) Dong, R.; Fang, Y.; Chae, J.; Dai, J.; Xiao, Z.; Dong, Q.; Yuan, Y.; Centrone, A.; Zeng, X. C.; Huang, J. High-Gain and Low-Driving-Voltage Photodetectors Based on Organolead Triiodide Perovskites. *Adv. Mater.* **2015**, *27* (11), 1912−1918.

(18) Ye, T.; Wang, X.; Li, X.; Yan, A. Q.; Ramakrishna, S.; Xu, J. Ultra-High Seebeck Coefficient and Low Thermal Conductivity of a Centimeter-Sized Perovskite Single Crystal Acquired by a Modified Fast Growth Method. *J. Mater. Chem. C* **2017**, *5* (5), 1255−1260.

(19) Chiba, T.; Hayashi, Y.; Ebe, H.; Hoshi, K.; Sato, J.; Sato, S.; Pu, Y. J.; Ohisa, S.; Kido, J. Anion-Exchange Red Perovskite Quantum Dots with Ammonium Iodine Salts for Highly Efficient Light-Emitting Devices. *Nat. Photonics* **2018**, *12* (11), 681−687.

(20) Tan, Z. K.; Moghaddam, R. S.; Lai, M. L.; Docampo, P.; Higler, R.; Deschler, F.; Price, M.; Sadhanala, A.; Pazos, L. M.; Credgington, D.; Hanusch, F.; Bein, T.; Snaith, H. J.; Friend, R. H. Bright Light-Emitting Diodes Based on Organometal Halide Perovskite. *Nat. Nanotechnol.* **2014**, *9*, 687−692.

(21) Rong, Y.; Hu, Y.; Mei, A.; Tan, H.; Saidaminov, M. I.; Seok, S. I.; McGehee, M. D.; Sargent, E. H.; Han, H. Challenges for Commercializing Perovskite Solar Cells. *Science* **2018**, *361*, No. eaat8235.

(22) Yin, W. J.; Shi, T.; Yan, Y. Unique Properties of Halide Perovskites as Possible Origins of the Superior Solar Cell Performance. *Adv. Mater.* **2014**, *26*, 4653−4658.

(23) Yin, W.-J.; Shi, T.; Yan, Y. Unusual Defect Physics in $CH_3NH_3PbI_3$ Perovskite Solar Cell Absorber. *Appl. Phys. Lett.* **2014**, *104*, 063903.

(24) Shao, S. Y.; Dong, J. J.; Duim, H.; Ten Brink, G. H.; Blake, G. R.; Portale, G.; Loi, M. A. Enhancing the Crystallinity and Perfecting the Orientation of Formamidinium Tin Iodide for Highly Efficient Sn-based Perovskite Solar Cells. *Nano Energy* **2019**, *60*, 810−816.

(25) Tai, Q.; Guo, X.; Tang, G.; You, P.; Ng, T. W.; Shen, D.; Cao, J.; Liu, C. K.; Wang, N.; Zhu, Y.; et al. Antioxidant Grain Passivation for Air-Stable Tin-Based Perovskite Solar Cells. *Angew. Chem., Int. Ed.* **2019**, *58*, 806−810.

(26) Lee, S. J.; Shin, S. S.; Im, J.; Ahn, T. K.; Noh, J. H.; Jeon, N. J.; Seok, S. I.; Seo, J. Reducing Carrier Density in Formamidinium Tin Perovskites and Its Beneficial Effects on Stability and Efficiency of Perovskite Solar Cells. *ACS Energy Lett.* **2018**, *3*, 46−53.

(27) Liao, W.; Zhao, D.; Yu, Y.; Grice, C. R.; Wang, C.; Cimaroli, A. J.; Schulz, P.; Meng, W.; Zhu, K.; Xiong, R.-G.; Yan, Y. Lead-Free Inverted Planar Formamidinium Tin Triiodide Perovskite Solar Cells Achieving Power Conversion Efficiencies up to 6.22%. *Adv. Mater.* **2016**, *28* (42), 9333−9340.

(28) Zhou, C.; Tian, Y.; Wang, M.; Rose, A.; Besara, T.; Doyle, N. K.; Yuan, Z.; Wang, J. C.; Clark, R.; Hu, Y.; Siegrist, T.; Lin, S.; Ma, B. Low-Dimensional Organic Tin Bromide Perovskites and Their

Photoinduced Structural Transformation. *Angew. Chem., Int. Ed.* **2017**, *56* (31), 9018−9022.
(29) Shao, S.; Liu, J.; Portale, G.; Fang, H. H.; Blake, G. R.; Ten Brink, G. H.; Koster, L. J. A.; Loi, M. A. Highly Reproducible Sn-Based Hybrid Perovskite Solar Cells with 9% Efficiency. *Adv. Energy Mater.* **2018**, *8* (4), 1702019.
(30) Shi, E.; Gao, Y.; Finkenauer, B. P.; Akriti, A.; Coffey, A. H.; Dou, L. Two-Dimensional Halide Perovskite Nanomaterials and Heterostructures. *Chem. Soc. Rev.* **2018**, *47* (16), 6046−6072.
(31) Krishnamoorthy, T.; Ding, H.; Yan, C.; Leong, W. L.; Baikie, T.; Zhang, Z.; Sherburne, M.; Li, S.; Asta, M.; Mathews, N.; Mhaisalkar, S. G. Lead-Free Germanium Iodide Perovskite Materials for Photovoltaic Applications. *J. Mater. Chem. A* **2015**, *3* (47), 23829−23832.
(32) Pawlaczyk, C.; Jakubas, R.; Unruh, H.-G. On the Dynamic Dielectric Behaviour of $(CH_3NH_3)_3Sb_2I_9$ (MAIA) Single Crystals. *Solid State Commun.* **1998**, *108* (4), 247−250.
(33) Mitzi, D. B. Organic-Inorganic Perovskites Containing Trivalent Metal Halide Layers: The Templating Influence of the Organic Cation Layer. *Inorg. Chem.* **2000**, *39* (26), 6107−6113.
(34) Lee, M. M.; Teuscher, J.; Miyasaka, T.; Murakami, T. N.; Snaith, H. J. Efficient Hybrid Solar Cells Based on Meso-Superstructured Organometal Halide Perovskites. *Science* **2012**, *338* (6107), 643−647.
(35) Hebig, J.-C.; Kühn, I.; Flohre, J.; Kirchartz, T. Optoelectronic Properties of $(CH_3NH_3)_3Sb_2I_9$ Thin Films for Photovoltaic Applications. *ACS Energy Lett.* **2016**, *1* (1), 309−314.
(36) Chabot, B.; Parthe, E. $Cs_3Sb_2I_9$ and $Cs_3Bi_2I_9$ with the Hexagonal $Cs_3Cr_2Cl_9$ Structure Type. *Acta Crystallogr., Sect. B: Struct. Crystallogr. Cryst. Chem.* **1978**, *34* (2), 645−648.
(37) Volonakis, G.; Filip, M. R.; Haghighirad, A. A.; Sakai, N.; Wenger, B.; Snaith, H. J.; Giustino, F. Lead-Free Halide Double Perovskites via Heterovalent Substitution of Noble Metals. *J. Phys. Chem. Lett.* **2016**, *7* (7), 1254−1259.
(38) Saparov, B.; Mitzi, D. B. Organic-Inorganic Perovskites: Structural Versatility for Functional Materials Design. *Chem. Rev.* **2016**, *116* (7), 4558−4596.
(39) Lehner, A. J.; Fabini, D. H.; Evans, H. A.; Hébert, C.-A.; Smock, S. R.; Hu, J.; Wang, H.; Zwanziger, J. W.; Chabinyc, M. L.; Seshadri, R. Crystal and Electronic Structures of Complex Bismuth Iodides $A_3Bi_2I_9$ (A = K, Rb, Cs) Related to Perovskite: Aiding the Rational Design of Photovoltaics. *Chem. Mater.* **2015**, *27* (20), 7137−7148.
(40) Cortecchia, D.; Dewi, H.; Yin, J.; Bruno, A.; Chen, S.; Baikie, T.; Boix, P.; Grätzel, M.; Mhaisalkar, S.; Soci, C.; Mathews, N. Lead-Free $MA_2CuCl_xBr_{4-x}$ Hybrid Perovskites. *Inorg. Chem.* **2016**, *55* (3), 1044−1052.
(41) Elseman, A. M.; Shalan, A. E.; Sajid, S.; Rashad, M. M.; Hassan, A. M.; Li, M. Copper-Substituted Lead Perovskite Materials Constructed with Different Halides for Working $(CH_3NH_3)_2CuX_4$-Based Perovskite Solar Cells from Experimental and Theoretical View. *ACS Appl. Mater. Interfaces* **2018**, *10* (14), 11699−11707.
(42) Wang, W.; Zhao, D.; Zhang, F.; Li, L.; Du, M.; Wang, C.; Yu, Y.; Huang, Q.; Zhang, M. L. L.; Li, L.; et al. Highly Sensitive Low-Bandgap Perovskite Photodetectors with Response from Ultraviolet to the Near-Infrared Region. *Adv. Funct. Mater.* **2017**, *27* (42), 1703953.
(43) Xu, X.; Chueh, C. C.; Jing, P.; Yang, Z.; Shi, X.; Zhao, T.; Lin, L. Y.; Jen, A. K. Y. High-Performance Near-IR Photodetector Using Low-Bandgap $MA_{0.5}FA_{0.5}Pb_{0.5}Sn_{0.5}I_3$ Perovskite. *Adv. Funct. Mater.* **2017**, *27* (28), 1701053.
(44) Zhu, H. L.; Liang, Z.; Huo, Z.; Ng, W. K.; Mao, J.; Wong, K. S.; Yin, W. J.; Choy, W. C. Low-Bandgap Methylammonium-Rubidium Cation Sn-Rich Perovskites for Efficient Ultraviolet-Visible-Near Infrared Photodetectors. *Adv. Funct. Mater.* **2018**, *28* (16), 1706068.
(45) Waleed, A.; Tavakoli, M. M.; Gu, L.; Wang, Z.; Zhang, D.; Manikandan, A.; Zhang, Q.; Zhang, R.; Chueh, Y.-L.; Fan, Z. Lead-Free Perovskite Nanowire Array Photodetectors with Drastically Improved Stability in Nanoengineering Templates. *Nano Lett.* **2017**, *17* (1), 523−530.
(46) Snyder, G. J.; Ursell, T. S. Thermoelectric Efficiency and Compatibility. *Phys. Rev. Lett.* **2003**, *91* (14), 148301.
(47) Xuan, T.; Xie, R. Recent Processes on Light-Emitting Lead-Free Metal Halide Perovskites. *Chem. Eng. J.* **2020**, *393*, 124757.
(48) Sun, J.; Yang, J.; Lee, J. I.; Cho, J. H.; Kang, M. S. Lead-Free Perovskite Nanocrystals for Light-Emitting Devices. *J. Phys. Chem. Lett.* **2018**, *9*, 1573−1583.
(49) Leng, M.; Chen, Z.; Yang, Y.; Li, Z.; Zeng, K.; Li, K.; Niu, G.; He, Y.; Zhou, Q.; Tang, J. Lead-Free, Blue Emitting Bismuth Halide Perovskite Quantum Dots. *Angew. Chem., Int. Ed.* **2016**, *55*, 15012−15016.
(50) Liang, H.; Yuan, F.; Johnston, A.; Gao, C.; Choubisa, H.; Gao, Y.; Wang, Y.; Sagar, L.; Sun, B.; Li, P.; Bappi, G.; Chen, b.; Li, J.; Wang, Y.; Dong, Y.; Ma, D.; Gao, Y.; Liu, Y.; Yuan, M.; Saidaminov, M. I.; Hoogland, S.; Lu, Z.-H.; Sargent, E. H. High Color Purity Lead-Free Perovskite Light-Emitting Diodes via Sn Stabilization. *Adv. Sci.* **2020**, *7*, 1903213.
(51) Liang, J.; Wang, C.; Wang, Y.; Xu, Z.; Lu, Z.; Ma, Y.; Zhu, H.; Hu, Y.; Xiao, C.; Yi, X.; et al. All-Inorganic Perovskite Solar Cells. *J. Am. Chem. Soc.* **2016**, *138* (49), 15829−15832.
(52) Umari, P.; Mosconi, E.; De Angelis, F. Relativistic GW Calculations on $CH_3NH_3PbI_3$ and $CH_3NH_3SnI_3$ Perovskites for Solar Cell Applications. *Sci. Rep.* **2015**, *4*, 4467.
(53) Takahashi, Y.; Obara, R.; Lin, Z.-Z.; Takahashi, Y.; Naito, T.; Inabe, T.; Ishibashi, S.; Terakura, K. Charge-Transport in Tin-Iodide Perovskite $CH_3NH_3SnI_3$: Origin of High Conductivity. *Dalton Trans.* **2011**, *40* (20), 5563−5568.
(54) Hao, F.; Stoumpos, C. C.; Cao, D. H.; Chang, R. P.; Kanatzidis, M. G. Lead-Free Solid-State Organic-Inorganic Halide Perovskite Solar Cells. *Nat. Photonics* **2014**, *8* (6), 489−494.
(55) Noel, N. K.; Stranks, S. D.; Abate, A.; Wehrenfennig, C.; Guarnera, S.; Haghighirad, A.-A.; Sadhanala, A.; Eperon, G. E.; Pathak, S. K.; Johnston, M. B.; et al. Lead-Free Organic-Inorganic Tin Halide Perovskites for Photovoltaic Applications. *Energy Environ. Sci.* **2014**, *7* (9), 3061−3068.
(56) Jokar, E.; Chien, C.-H.; Fathi, A.; Rameez, M.; Chang, Y.-H.; Diau, E. W.-G. Slow Surface Passivation and Crystal Relaxation with Additives to Improve Device Performance and Durability for Tin-Based Perovskite Solar Cells. *Energy Environ. Sci.* **2018**, *11* (9), 2353−2362.
(57) Lee, J.-W.; Kim, H.-S.; Park, N.-G. Lewis Acid-Base Adduct Approach for High Efficiency Perovskite Solar Cells. *Acc. Chem. Res.* **2016**, *49* (2), 311−319.
(58) Noel, N. K.; Abate, A.; Stranks, S. D.; Parrott, E. S.; Burlakov, V. M.; Goriely, A.; Snaith, H. J. Enhanced Photoluminescence and Solar Cell Performance via Lewis Base Passivation of Organic-Inorganic Lead Halide Perovskites. *ACS Nano* **2014**, *8* (10), 9815−9821.
(59) Song, T.-B.; Yokoyama, T.; Stoumpos, C. C.; Logsdon, J.; Cao, D. H.; Wasielewski, M. R.; Aramaki, S.; Kanatzidis, M. G. Importance of Reducing Vapor Atmosphere in the Fabrication of Tin-Based Perovskite Solar Cells. *J. Am. Chem. Soc.* **2017**, *139* (2), 836−842.
(60) Birkhold, S. T.; Precht, J. T.; Liu, H.; Giridharagopal, R.; Eperon, G. E.; Schmidt-Mende, L.; Li, X.; Ginger, D. S. Interplay of Mobile Ions and Injected Carriers Creates Recombination Centers in Metal Halide Perovskites Under Bias. *ACS Energy Lett.* **2018**, *3* (6), 1279−1286.
(61) Lee, H.; Kim, A.; Kwon, H.-C.; Yang, W.; Oh, Y.; Lee, D.; Moon, J. Retarding Crystallization During Facile Single Coating of NaCl-Incorporated Precursor Solution for Efficient Large-Area Uniform Perovskite Solar Cells. *ACS Appl. Mater. Interfaces* **2016**, *8* (43), 29419−29426.
(62) Kayesh, M. E.; Chowdhury, T. H.; Matsuishi, K.; Kaneko, R.; Kazaoui, S.; Lee, J.-J.; Noda, T.; Islam, A. Enhanced Photovoltaic Performance of $FASnI_3$-Based Perovskite Solar Cells with Hydrazinium Chloride Coadditive. *ACS Energy Lett.* **2018**, *3* (7), 1584−1589.
(63) Song, T.-B.; Yokoyama, T.; Aramaki, S.; Kanatzidis, M. G. Performance Enhancement of Lead-Free Tin-Based Perovskite Solar

https://dx.doi.org/10.1021/acsami.0c02575
ACS Appl. Mater. Interfaces 2020, 12, 26776−26811

Cells with Reducing Atmosphere-Assisted Dispersible Additive. *ACS Energy Lett.* **2017**, *2* (4), 897−903.
(64) Gai, C.; Wang, J.; Wang, Y.; Li, J. The Low-Dimensional Three-Dimensional Tin Halide Perovskite: Film Characterization and Device Performance. *Energies* **2020**, *13* (1), 1−26.
(65) Mitzi, D. B.; Feild, C.; Harrison, W.; Guloy, A. Conducting Tin Halides with a Layered Organic-Based Perovskite Structure. *Nature* **1994**, *369* (6480), 467−469.
(66) Kagan, C.; Mitzi, D.; Dimitrakopoulos, C. Organic-Inorganic Hybrid Materials as Semiconducting Channels in Thin-Film Field-Effect Transistors. *Science* **1999**, *286* (5441), 945−947.
(67) Smith, I. C.; Hoke, E. T.; Solis-Ibarra, D.; McGehee, M. D.; Karunadasa, H. I. A Layered Hybrid Perovskite Solar-Cell Absorber with Enhanced Moisture Stability. *Angew. Chem., Int. Ed.* **2014**, *53* (42), 11232−11235.
(68) Liao, Y.; Liu, H.; Zhou, W.; Yang, D.; Shang, Y.; Shi, Z.; Li, B.; Jiang, X.; Zhang, L.; Quan, L. N.; et al. Highly Oriented Low-Dimensional Tin Halide Perovskites with Enhanced Stability and Photovoltaic Performance. *J. Am. Chem. Soc.* **2017**, *139* (19), 6693−6699.
(69) Xu, H.; Jiang, Y.; He, T.; Li, S.; Wang, H.; Chen, Y.; Yuan, M.; Chen, J. Orientation Regulation of Tin-Based Reduced-Dimensional Perovskites for Highly Efficient and Stable Photovoltaics. *Adv. Funct. Mater.* **2019**, *29*, 1807696.
(70) Wang, F.; Jiang, X.; Chen, H.; Shang, Y.; Liu, H.; Wei, J.; Zhou, W.; He, H.; Liu, W.; Ning, Z. 2D-Quasi-2D-3D Hierarchy Structure for Tin Perovskite Solar Cells with Enhanced Efficiency and Stability. *Joule* **2018**, *2* (12), 2732−2743.
(71) Ran, C.; Xi, J.; Gao, W.; Yuan, F.; Lei, T.; Jiao, B.; Hou, X.; Wu, Z. Bilateral Interface Engineering Toward Efficient 2D-3D Bulk Heterojunction Tin Halide Lead-Free Perovskite Solar Cells. *ACS Energy Lett.* **2018**, *3* (3), 713−721.
(72) Soe, C. M. M.; Nagabhushana, G.; Shivaramaiah, R.; Tsai, H.; Nie, W.; Blancon, J.-C.; Melkonyan, F.; Cao, D. H.; Traoré, B.; Pedesseau, L.; et al. Structural and Thermodynamic Limits of Layer Thickness in 2D Halide Perovskites. *Proc. Natl. Acad. Sci. U. S. A.* **2019**, *116* (1), 58−66.
(73) Jesper Jacobsson, T.; Correa-Baena, J.-P.; Pazoki, M.; Saliba, M.; Schenk, K.; Gratzel, M.; Hagfeldt, A. Exploration of the Compositional Space for Mixed Lead Halogen Perovskites for High Efficiency Solar Cells. *Energy Environ. Sci.* **2016**, *9* (5), 1706−1724.
(74) Mei, A.; Li, X.; Liu, L.; Ku, Z.; Liu, T.; Rong, Y.; Xu, M.; Hu, M.; Chen, J.; Yang, Y.; et al. A Hole-Conductor-Free, Fully Printable Mesoscopic Perovskite Solar Cell with High Stability. *Science* **2014**, *345* (6194), 295−298.
(75) Hu, M.; Liu, L.; Mei, A.; Yang, Y.; Liu, T.; Han, H. Efficient Hole-Conductor-Free, Fully Printable Mesoscopic Perovskite Solar Cells with a Broad Light Harvester $NH_2CH = NH_2PbI_3$. *J. Mater. Chem. A* **2014**, *2* (40), 17115−17121.
(76) Liao, W.; Zhao, D.; Yu, Y.; Shrestha, N.; Ghimire, K.; Grice, C. R.; Wang, C.; Xiao, Y.; Cimaroli, A. J.; Ellingson, R. J.; et al. Fabrication of Efficient Low-Bandgap Perovskite Solar Cells by Combining Formamidinium Tin Iodide with Methylammonium Lead Iodide. *J. Am. Chem. Soc.* **2016**, *138* (38), 12360−12363.
(77) Eperon, G. E.; Leijtens, T.; Bush, K. A.; Prasanna, R.; Green, T.; Wang, J. T. W.; McMeekin, D. P.; Volonakis, G.; Milot, R. L.; May, R. Perovskite-Perovskite Tandem Photovoltaics with Optimized Band Gaps. *Science* **2016**, *354* (6314), 861−865.
(78) Ferrara, C.; Patrini, M.; Pisanu, A.; Quadrelli, P.; Milanese, C.; Tealdi, C.; Malavasi, L. Wide Band-Gap Tuning in Sn-Based Hybrid Perovskites through Cation Replacement: The $FA_{1-x}MA_xSnBr_3$ Mixed System. *J. Mater. Chem. A* **2017**, *5* (19), 9391−9395.
(79) Ma, Z.-Q.; Pan, H.; Wong, P. K. A First-Principles Study on the Structural and Electronic Properties of Sn-Based Organic-Inorganic Halide Perovskites. *J. Electron. Mater.* **2016**, *45* (11), 5956−5966.
(80) Weber, O.; Charles, B.; Weller, M. Phase Behaviour and Composition in the Formamidinium-Methylammonium Hybrid Lead Iodide Perovskite Solid Solution. *J. Mater. Chem. A* **2016**, *4* (40), 15375−15383.
(81) Zhao, Z.; Gu, F.; Li, Y.; Sun, W.; Ye, S.; Rao, H.; Liu, Z.; Bian, Z.; Huang, C. Mixed-Organic-Cation Tin Iodide for Lead-Free Perovskite Solar Cells with an Efficiency of 8.12%. *Adv. Sci.* **2017**, *4* (11), 1700204.
(82) Yang, Z.; Rajagopal, A.; Chueh, C. C.; Jo, S. B.; Liu, B.; Zhao, T.; Jen, A. K. Y. Stable Low-Bandgap Pb-Sn Binary Perovskites for Tandem Solar Cells. *Adv. Mater.* **2016**, *28* (40), 8990−8997.
(83) Wang, Y.-Q.; Xu, S.-B.; Deng, J.-G.; Gao, L.-Z. Enhancing the Efficiency of Planar Heterojunction Perovskite Solar Cells via Interfacial Engineering with 3-Aminopropyl Trimethoxy Silane Hydrolysate. *R. Soc. Open Sci.* **2017**, *4* (12), 170980.
(84) Zhao, B.; Abdi-Jalebi, M.; Tabachnyk, M.; Glass, H.; Kamboj, V. S.; Nie, W.; Pearson, A. J.; Puttisong, Y.; Gödel, K. C.; Beere, H. E.; et al. High Open-Circuit Voltages in Tin-Rich Low-Bandgap Perovskite-Based Planar Heterojunction Photovoltaics. *Adv. Mater.* **2017**, *29* (2), 1604744.
(85) Li, M.; Wang, Z. K.; Zhuo, M. P.; Hu, Y.; Hu, K. H.; Ye, Q. Q.; Jain, S. M.; Yang, Y. G.; Gao, X. Y.; Liao, L. S. Pb-Sn-Cu Ternary Organometallic Halide Perovskite Solar Cells. *Adv. Mater.* **2018**, *30* (20), 1800258.
(86) Ito, N.; Kamarudin, M. A.; Hirotani, D.; Zhang, Y.; Shen, Q.; Ogomi, Y.; Iikubo, S.; Minemoto, T.; Yoshino, K.; Hayase, S. Mixed Sn-Ge Perovskite for Enhanced Perovskite Solar Cell Performance in Air. *J. Phys. Chem. Lett.* **2018**, *9* (7), 1682−1688.
(87) Zhao, J.; Deng, Y.; Wei, H.; Zheng, X.; Yu, Z.; Shao, Y.; Shield, J. E.; Huang, J. Strained Hybrid Perovskite Thin Films and Their Impact on the Intrinsic Stability of Perovskite Solar Cells. *Sci. Adv.* **2017**, *3* (11), No. eaao5616.
(88) Anaya, M.; Correa-Baena, J. P.; Lozano, G.; Saliba, M.; Anguita, P.; Roose, B.; Abate, A.; Steiner, U.; Grätzel, M.; Calvo, M. E.; et al. Optical Analysis of $CH_3NH_3Sn_xPb_{1-x}I_3$ Absorbers: A Roadmap for Perovskite-on-Perovskite Tandem Solar Cells. *J. Mater. Chem. A* **2016**, *4* (29), 11214−11221.
(89) Nie, W.; Tsai, H.; Asadpour, R.; Blancon, J.-C.; Neukirch, A. J.; Gupta, G.; Crochet, J. J.; Chhowalla, M.; Tretiak, S.; Alam, M. A.; et al. High-Efficiency Solution-Processed Perovskite Solar Cells with Millimeter-Scale Grains. *Science* **2015**, *347* (6221), 522−525.
(90) Ali, R.; Hou, G.-J.; Zhu, Z.-G.; Yan, Q.-B.; Zheng, Q.-R.; Su, G. Stable Mixed Group II (Ca, Sr) and XIV (Ge, Sn) Lead-Free Perovskite Solar Cells. *J. Mater. Chem. A* **2018**, *6* (19), 9220−9227.
(91) Li, L.; Zhang, F.; Hao, Y.; Sun, Q.; Li, Z.; Wang, H.; Cui, Y.; Zhu, F. High Efficiency Planar Sn−Pb Binary Perovskite Solar Cells: Controlled Growth of Large Grains via a One-Step Solution Fabrication Process. *J. Mater. Chem. C* **2017**, *5* (9), 2360−2311.
(92) Kumar, M. H.; Dharani, S.; Leong, W. L.; Boix, P. P.; Prabhakar, R. R.; Baikie, T.; Shi, C.; Ding, H.; Ramesh, R.; Asta, M.; et al. Lead-Free Halide Perovskite Solar Cells with High Photocurrents Realized through Vacancy Modulation. *Adv. Mater.* **2014**, *26* (41), 7122−7127.
(93) Huang, J.; Tan, S.; Lund, P. D.; Zhou, H. Impact of H_2O on Organic-Inorganic Hybrid Perovskite Solar Cells. *Energy Environ. Sci.* **2017**, *10* (11), 2284−2311.
(94) Yokoyama, T.; Cao, D. H.; Stoumpos, C. C.; Song, T.-B.; Sato, Y.; Aramaki, S.; Kanatzidis, M. G. Overcoming Short-Circuit in Lead-Free $CH_3NH_3SnI_3$ Perovskite Solar Cells via Kinetically Controlled Gas-Solid Reaction Film Fabrication Process. *J. Phys. Chem. Lett.* **2016**, *7* (5), 776−782.
(95) Zhu, Z.; Chueh, C. C.; Li, N.; Mao, C.; Jen, A. K. Y. Realizing Efficient Lead-Free Formamidinium Tin Triiodide Perovskite Solar Cells via a Sequential Deposition Route. *Adv. Mater.* **2018**, *30* (6), 1703800.
(96) Mosconi, E.; Umari, P.; De Angelis, F. Electronic and Optical Properties of Mixed Sn-Pb Organohalide Perovskites: A First Principles Investigation. *J. Mater. Chem. A* **2015**, *3* (17), 9208−9215.
(97) Chi, D.; Huang, S.; Zhang, M.; Mu, S.; Zhao, Y.; Chen, Y.; You, J. Composition and Interface Engineering for Efficient and Thermally Stable Pb-Sn Mixed Low-Bandgap Perovskite Solar Cells. *Adv. Funct. Mater.* **2018**, *28* (51), 1804603.

https://dx.doi.org/10.1021/acsami.0c02575
ACS Appl. Mater. Interfaces 2020, 12, 26776−26811

(98) Zhu, H. L.; Choy, W. C. Crystallization, Properties, and Challenges of Low-Bandgap Sn−Pb Binary Perovskites. *Solar RRL* **2018**, *2* (10), 1800146.
(99) Junda, M. M.; Zhao, D.; Subedi, B.; Wang, C.; Chen, C.; Yan, Y.; Podraza, N. J. Atmospherically Induced Defects in $(FAI_3)_{0.6}(MAPbI_{3-3x}Cl_{3x})_{0.4}$ Perovskites. *J. Phys. D: Appl. Phys.* **2019**, *52* (17), 175102.
(100) Zuo, F.; Williams, S. T.; Liang, P. W.; Chueh, C. C.; Liao, C. Y.; Jen, A. K. Y. Binary-Metal Perovskites toward High-Performance Planar-Heterojunction Hybrid Solar Cells. *Adv. Mater.* **2014**, *26* (37), 6454−6460.
(101) Li, Y.; Sun, W.; Yan, W.; Ye, S.; Rao, H.; Peng, H.; Zhao, Z.; Bian, Z.; Liu, Z.; Zhou, H.; Huang, C. 50% Sn-Based Planar Perovskite Solar Cell with Power Conversion Efficiency up to 13.6%. *Adv. Energy Mater.* **2016**, *6* (24), 1601353.
(102) Yang, Z.; Chueh, C.-C.; Liang, P.-W.; Crump, M.; Lin, F.; Zhu, Z.; Jen, A. K.-Y. Effects of Formamidinium and Bromide Ion Substitution in Methylammonium Lead Triiodide toward High-Performance Perovskite Solar Cells. *Nano Energy* **2016**, *22*, 328−337.
(103) Cao, C.; Zhang, C.; Yang, J.; Sun, J.; Pang, S.; Wu, H.; Wu, R.; Gao, Y.; Liu, C. Iodine and Chlorine Element Evolution in $CH_3NH_3PbI_{3-x}Cl_x$ Thin Films for Highly Efficient Planar Heterojunction Perovskite Solar Cells. *Chem. Mater.* **2016**, *28* (8), 2742−2749.
(104) Pellet, N.; Gao, P.; Gregori, G.; Yang, T. Y.; Nazeeruddin, M. K.; Maier, J.; Grätzel, M. Mixed-Organic-Cation Perovskite Photovoltaics for Enhanced Solar-Light Harvesting. *Angew. Chem., Int. Ed.* **2014**, *53* (12), 3151−3157.
(105) Dang, Y.; Zhou, Y.; Liu, X.; Ju, D.; Xia, S.; Xia, H.; Tao, X. Formation of Hybrid Perovskite Tin Iodide Single Crystals by Top-Seeded Solution Growth. *Angew. Chem., Int. Ed.* **2016**, *55* (10), 3447−3450.
(106) Diau, E. W.-G.; Jokar, E.; Rameez, M. Strategies to Improve Performance and Stability for Tin-Based Perovskite Solar Cells. *ACS Energy Lett.* **2019**, *4* (8), 1930−1937.
(107) Zhao, D.; Yu, Y.; Wang, C.; Liao, W.; Shrestha, N.; Grice, C. R.; Cimaroli, A. J.; Guan, L.; Ellingson, R. J.; Zhu, K.; et al. Low-Bandgap Mixed Tin-Lead Iodide Perovskite Absorbers with Long Carrier Lifetimes for All-Perovskite Tandem Solar Cells. *Nat. Energy.* **2017**, *2* (4), 17018.
(108) Ni, C.; Hedley, G.; Payne, J.; Svrcek, V.; McDonald, C.; Jagadamma, L. K.; Edwards, P.; Martin, R.; Jain, G.; Carolan, D.; et al. Charge Carrier Localised in Zero-Dimensional $(CH_3NH_3)_3Bi_2I_9$ Clusters. *Nat. Commun.* **2017**, *8* (1), 170.
(109) Kou, B.; Zhang, W.; Ji, C.; Wu, Z.; Zhang, S.; Liu, X.; Luo, J. Tunable Optical Absorption in Lead-Free Perovskite-Like Hybrids by Iodide Management. *Chem. Commun.* **2019**, *55* (94), 14174−14177.
(110) Marti, A.; Araújo, G. L. Limiting Efficiencies for Photovoltaic Energy Conversion in Multigap Systems. *Sol. Energy Mater. Sol. Cells* **1996**, *43* (2), 203−222.
(111) Zuo, C.; Bolink, H. J.; Han, H.; Huang, J.; Cahen, D.; Ding, L. Advances in Perovskite Solar Cells. *Adv. Sci.* **2016**, *3* (7), 1500324.
(112) Park, B. W.; Philippe, B.; Zhang, X.; Rensmo, H.; Boschloo, G.; Johansson, E. M. Bismuth Based Hybrid Perovskites $A_3Bi_2I_9$ (A: Methylammonium or Cesium) for Solar Cell Application. *Adv. Mater.* **2015**, *27* (43), 6806−6813.
(113) Eckhardt, K.; Bon, V.; Getzschmann, J.; Grothe, J.; Wisser, F. M.; Kaskel, S. Crystallographic Insights into $(CH_3NH_3)_3(Bi_2I_9)$: A New Lead-Free Hybrid Organic−Inorganic Material as a Potential Absorber for Photovoltaics. *Chem. Commun.* **2016**, *52* (14), 3058−3060.
(114) Okano, T.; Suzuki, Y. Gas-Assisted Coating of Bi-Based $(CH_3NH_3)_3Bi_2I_9$ Active Layer in Perovskite Solar Cells. *Mater. Lett.* **2017**, *191*, 77−79.
(115) Kulkarni, A.; Singh, T.; Ikegami, M.; Miyasaka, T. Photovoltaic Enhancement of Bismuth Halide Hybrid Perovskite by N-Methyl Pyrrolidone-Assisted Morphology Conversion. *RSC Adv.* **2017**, *7* (16), 9456−9460.
(116) Mali, S. S.; Kim, H.; Kim, D. H.; Kook Hong, C. Anti-Solvent Assisted Crystallization Processed Methylammonium Bismuth Iodide Cuboids towards Highly Stable Lead-Free Perovskite Solar Cells. *Chemistry Select* **2017**, *2* (4), 1578−1585.
(117) Ran, C.; Wu, Z.; Xi, J.; Yuan, F.; Dong, H.; Lei, T.; He, X.; Hou, X. Construction of Compact Methylammonium Bismuth Iodide Film Promoting Lead-Free Inverted Planar Heterojunction Organohalide Solar Cells with Open-Circuit Voltage Over 0.8 V. *J. Phys. Chem. Lett.* **2017**, *8* (2), 394−400.
(118) McClure, E. T.; Ball, M. R.; Windl, W.; Woodward, P. M. Cs_2AgBiX_6 (X= Br, Cl): New Visible Light Absorbing, Lead-Free Halide Perovskite Semiconductors. *Chem. Mater.* **2016**, *28* (5), 1348−1354.
(119) Greul, E.; Petrus, M. L.; Binek, A.; Docampo, P.; Bein, T. Highly Stable, Phase Pure $Cs_2AgBiBr_6$ Double Perovskite Thin Films for Optoelectronic Applications. *J. Mater. Chem. A* **2017**, *5* (37), 19972−19981.
(120) Slavney, A. H.; Hu, T.; Lindenberg, A. M.; Karunadasa, H. I. A Bismuth-Halide Double Perovskite with Long Carrier Recombination Lifetime for Photovoltaic Applications. *J. Am. Chem. Soc.* **2016**, *138* (7), 2138−2141.
(121) Savenije, T. J.; Ferguson, A. J.; Kopidakis, N.; Rumbles, G. Revealing the Dynamics of Charge Carriers in Polymer: Fullerene Blends Using Photoinduced Time-Resolved Microwave Conductivity. *J. Phys. Chem. C* **2013**, *117* (46), 24085−24103.
(122) Saparov, B.; Hong, F.; Sun, J.-P.; Duan, H.-S.; Meng, W.; Cameron, S.; Hill, I. G.; Yan, Y.; Mitzi, D. B. Thin-Film Preparation and Characterization of $Cs_3Sb_2I_9$: A Lead-Free Layered Perovskite Semiconductor. *Chem. Mater.* **2015**, *27* (16), 5622−5632.
(123) Bartesaghi, D.; Slavney, A. H.; Gélvez-Rueda, M. C.; Connor, B. A.; Grozema, F. C.; Karunadasa, H. I.; Savenije, T. J. Charge Carrier Dynamics in $Cs_2AgBiBr_6$ Double Perovskite. *J. Phys. Chem. C* **2018**, *122* (9), 4809−4816.
(124) Herz, L. M. Charge-Carrier Mobilities in Metal Halide Perovskites: Fundamental Mechanisms and Limits. *ACS Energy Lett.* **2017**, *2* (7), 1539−1548.
(125) Sun, P.-P.; Li, Q.-S.; Yang, L.-N.; Li, Z.-S. Theoretical Insights into a Potential Lead-Free Hybrid Perovskite: Substituting Pb^{2+} with Ge^{2+}. *Nanoscale* **2016**, *8* (3), 1503−1512.
(126) Kubetsky, L. USSR, Author's certificate #24040, Priority date 4 August 1930.
(127) Carli, B.; Melchiorri, F. Considerations about Far Infrared Detectors for Astronomical Purposes. *Infrared Phys.* **1973**, *13* (1), 49−60.
(128) Krotz, P.; Stupar, D.; Krieg, J.; Sonnabend, G.; Sornig, M.; Giorgetta, F.; Baumann, E.; Giovannini, M.; Hoyler, N.; Hofstetter, D.; Schieder, R. Applications for Quantum Cascade Lasers and Detectors in Mid-Infrared High-Resolution Heterodyne Astronomy. *Appl. Phys. B: Lasers Opt.* **2008**, *90* (2), 187−190.
(129) Rogalski, A.; Antoszewski, J.; Faraone, L. Third-Generation Infrared Photodetector Arrays. *J. Appl. Phys.* **2009**, *105* (9), 091101.
(130) Liu, C.; Peng, H.; Wang, K.; Wei, C.; Wang, Z.; Gong, X. PbS Quantum Dots-Induced Trap-Assisted Charge Injection in Perovskite Photodetectors. *Nano Energy* **2016**, *30*, 27−35.
(131) Liu, C.; Wang, K.; Du, P.; Wang, E.; Gong, X.; Heeger, A. J. Ultrasensitive Solution-Processed Broad-Band Photodetectors Using $CH_3NH_3PbI_3$ Perovskite Hybrids and PbS Quantum Dots as Light Harvesters. *Nanoscale* **2015**, *7* (39), 16460−16469.
(132) Hu, W.; Huang, W.; Yang, S.; Wang, X.; Jiang, Z.; Zhu, X.; Zhou, H.; Liu, H.; Zhang, Q.; Zhuang, X.; et al. High-Performance Flexible Photodetectors Based on High-Quality Perovskite Thin Films by a Vapor-Solution Method. *Adv. Mater.* **2017**, *29* (43), 1703256.
(133) Chen, S.; Teng, C.; Zhang, M.; Li, Y.; Xie, D.; Shi, G. A Flexible UV-Vis-NIR Photodetector Based on a Perovskite/Conjugated-Polymer Composite. *Adv. Mater.* **2016**, *28* (28), 5969−5974.
(134) Fang, Y.; Dong, Q.; Shao, Y.; Yuan, Y.; Huang, J. Highly Narrowband Perovskite Single-Crystal Photodetectors Enabled by Surface-Charge Recombination. *Nat. Photonics* **2015**, *9* (10), 679−686.

https://dx.doi.org/10.1021/acsami.0c02575
ACS Appl. Mater. Interfaces 2020, 12, 26776−26811

(135) Lee, Y.; Kwon, J.; Hwang, E.; Ra, C. H.; Yoo, W. J.; Ahn, J. H.; Park, J. H.; Cho, J. H. High-Performance Perovskite-Graphene Hybrid Photodetector. *Adv. Mater.* **2015**, *27* (1), 41−46.
(136) Lu, H.; Tian, W.; Cao, F.; Ma, Y.; Gu, B.; Li, L. A Self-Powered and Stable All-Perovskite Photodetector-Solar Cell Nanosystem. *Adv. Funct. Mater.* **2016**, *26* (8), 1296−1302.
(137) Ning, Z.; Gong, X.; Comin, R.; Walters, G.; Fan, F.; Voznyy, O.; Yassitepe, E.; Buin, A.; Hoogland, S.; Sargent, E. H. Quantum-Dot-in-Perovskite Solids. *Nature* **2015**, *523* (7560), 324−328.
(138) Ahmadi, M.; Wu, T.; Hu, B. A Review on Organic-Inorganic Halide Perovskite Photodetectors: Device Engineering and Fundamental Physics. *Adv. Mater.* **2017**, *29* (41), 1605242.
(139) Saidaminov, M. I.; Haque, M. A.; Savoie, M.; Abdelhady, A. L.; Cho, N.; Dursun, I.; Buttner, U.; Alarousu, E.; Wu, T.; Bakr, O. M. Perovskite Photodetectors Operating in Both Narrowband and Broadband Regimes. *Adv. Mater.* **2016**, *28* (37), 8144−8149.
(140) Xia, H.-R.; Li, J.; Sun, W.-T.; Peng, L.-M. Organohalide Lead Perovskite Based Photodetectors with Much Enhanced Performance. *Chem. Commun.* **2014**, *50* (89), 13695−13697.
(141) Dou, L.; Yang, Y. M.; You, J.; Hong, Z.; Chang, W.-H.; Li, G.; Yang, Y. Solution-Processed Hybrid Perovskite Photodetectors with High Detectivity. *Nat. Commun.* **2014**, *5*, 5404−5410.
(142) Zhu, T.; Yang, Y.; Zheng, L.; Liu, L.; Becker, M. L.; Gong, X. Solution-Processed Flexible Broadband Photodetectors with Solution-Processed Transparent Polymeric Electrode. *Adv. Funct. Mater.* **2020**, *30*, 1909487.
(143) Xu, X.; Yan, L.; Zou, T.; Qiu, R.; Liu, C.; Dai, Q.; Chen, J.; Zhang, S.; Zhou, H. Enhanced Detectivity and Suppressed Dark Current of Perovskite-InGaZnO Phototransistor via a PCBM Interlayer. *ACS Appl. Mater. Interfaces* **2018**, *10* (50), 44144−44151.
(144) Chen, H.-W.; Sakai, N.; Jena, A. K.; Sanehira, Y.; Ikegami, M.; Ho, K.-C.; Miyasaka, T. A Switchable High-Sensitivity Photodetecting and Photovoltaic Device with Perovskite Absorber. *J. Phys. Chem. Lett.* **2015**, *6* (9), 1773−1779.
(145) Li, F.; Ma, C.; Wang, H.; Hu, W.; Yu, W.; Sheikh, A. D.; Wu, T. Ambipolar Solution-Processed Hybrid Perovskite Phototransistors. *Nat. Commun.* **2015**, *6*, 8238.
(146) Hu, X.; Zhang, X.; Liang, L.; Bao, J.; Li, S.; Yang, W.; Xie, Y. High-Performance Flexible Broadband Photodetector Based on Organolead Halide Perovskite. *Adv. Funct. Mater.* **2014**, *24* (46), 7373−7380.
(147) Deng, W.; Zhang, X.; Huang, L.; Xu, X.; Wang, L.; Wang, J.; Shang, Q.; Lee, S. T.; Jie, J. Aligned Single-Crystalline Perovskite Microwire Arrays for High-Performance Flexible Image Sensors with Long-Term Stability. *Adv. Mater.* **2016**, *28* (11), 2201−2208.
(148) Im, J.; Stoumpos, C. C.; Jin, H.; Freeman, A. J.; Kanatzidis, M. G. Antagonism between Spin-Orbit Coupling and Steric Effects Causes Anomalous Band Gap Evolution in the Perovskite Photovoltaic Materials $CH_3NH_3Sn_{1-x}Pb_xI_3$. *J. Phys. Chem. Lett.* **2015**, *6* (17), 3503−3509.
(149) Liu, C. K.; Tai, Q.; Wang, N.; Tang, G.; Loi, H. L.; Yan, F. Sn-Based Perovskite for Highly Sensitive Photodetectors. *Adv. Sci.* **2019**, *6* (17), 1900751.
(150) Kneissl, M.; Seong, T. Y.; Han, J.; Amano, H. The Emergence and Prospects of Deep-Ultraviolet Light-Emitting Diode Technologies. *Nat. Photonics* **2019**, *13* (4), 233−244.
(151) Leng, M.; Yang, Y.; Zeng, K.; Chen, Z.; Tan, Z.; Li, S.; Li, J.; Xu, B.; Li, D.; Hautzinger, M. P.; et al. All-Inorganic Bismuth-Based Perovskite Quantum Dots with Bright Blue Photoluminescence and Excellent Stability. *Adv. Funct. Mater.* **2018**, *28* (1), 1704446.
(152) Maughan, A. E.; Ganose, A. M.; Bordelon, M. M.; Miller, E. M.; Scanlon, D. O.; Neilson, J. R. Defect Tolerance to Intolerance in the Vacancy-Ordered Double Perovskite Semiconductors Cs_2SnI_6 and Cs_2TeI_6. *J. Am. Chem. Soc.* **2016**, *138* (27), 8453−8464.
(153) Chen, J.; Luo, Z.; Fu, Y.; Wang, X.; Czech, K. J.; Shen, S.; Guo, L.; Wright, J. C.; Pan, A.; Jin, S. Tin (IV)-Tolerant Vapor-Phase Growth and Photophysical Properties of Aligned Cesium Tin Halide Perovskite ($CsSnX_3$; X= Br, I) Nanowires. *ACS Energy Lett.* **2019**, *4* (5), 1045−1052.
(154) Ravi, V. K.; Singhal, N.; Nag, A. Initiation and Future Prospects of Colloidal Metal Halide Double-Perovskite Nanocrystals: Cs_2AgBiX_6 (X= Cl, Br, I). *J. Mater. Chem. A* **2018**, *6* (44), 21666−21675.
(155) Huang Chen, S.-W.; Shen, C.-C.; Wu, T.; Liao, Z.-Y.; Chen, L.-F.; Zhou, J.-R.; Lee, C.-F.; Lin, C.-H.; Lin, C.-C.; Sher, C.-W.; et al. Full-Color Monolithic Hybrid Quantum Dot Nanoring Micro Light-Emitting Diodes with Improved Efficiency using Atomic Layer Deposition and Nonradiative Resonant Energy Transfer. *Photonics Res.* **2019**, *7* (4), 416−422.
(156) Tan, Z.; Li, J.; Zhang, C.; Li, Z.; Hu, Q.; Xiao, Z.; Kamiya, T.; Hosono, H.; Niu, G.; Lifshitz, E.; et al. Highly Efficient Blue-Emitting Bi-Doped Cs_2SnCl_6 Perovskite Variant: Photoluminescence Induced by Impurity Doping. *Adv. Funct. Mater.* **2018**, *28* (29), 1801131.
(157) Xiao, Z.; Song, Z.; Yan, Y. From Lead Halide Perovskites to Lead-Free Metal Halide Perovskites and Perovskite Derivatives. *Adv. Mater.* **2019**, *31* (47), 1803792.
(158) Dave, K.; Fang, M. H.; Bao, Z.; Fu, H. T.; Liu, R. S. Recent Developments in Lead-Free Double Perovskites: Structure, Doping, and Applications. *Chem. - Asian J.* **2020**, *15* (2), 242−252.
(159) Ushakova, E. V.; Cherevkov, S. A.; Kuznetsova, V. A.; Baranov, A. V. Lead-Free Perovskites for Lighting and Lasing Applications: A Minireview. *Materials* **2019**, *12* (23), 3845.
(160) Zhou, J.; Luo, J.; Rong, X.; Wei, P.; Molokeev, M. S.; Huang, Y.; Zhao, J.; Liu, Q.; Zhang, X.; Tang, J.; Xia, Z. Lead-Free Perovskite Derivative $Cs_2SnCl_{6-x}Br_x$ Single Crystals for Narrowband Photodetectors. *Adv. Opt. Mater.* **2019**, *7* (10), 1900139.
(161) Zhou, J.; Rong, X.; Molokeev, M. S.; Zhang, X.; Xia, Z. Exploring the Transposition Effects on the Electronic and Optical Properties of $Cs_2AgSbCl_6$ via a Combined Computational-Experimental Approach. *J. Mater. Chem. A* **2018**, *6* (5), 2346−2352.
(162) Luo, J.; Wang, X.; Li, S.; Liu, J.; Guo, Y.; Niu, G.; Yao, L.; Fu, Y.; Gao, L.; Dong, Q.; et al. Efficient and Stable Emission of Warm-White Light from Lead-Free Halide Double Perovskites. *Nature* **2018**, *563* (7732), 541−545.
(163) Xuan, T.; Yang, X.; Lou, S.; Huang, J.; Liu, Y.; Yu, J.; Li, H.; Wong, K. L.; Wang, C.; Wang, J. Highly Stable $CsPbBr_3$ Quantum Dots Coated with Alkyl Phosphate for White Light-Emitting Diodes. *Nanoscale* **2017**, *9* (40), 15286−15290.
(164) Hu, H.; Wu, L.; Tan, Y.; Zhong, Q.; Chen, M.; Qiu, Y.; Yang, D.; Sun, B.; Zhang, Q.; Yin, Y. Interfacial synthesis of highly stable $CsPbX_3$/Oxide Janus Nanoparticles. *J. Am. Chem. Soc.* **2018**, *140* (1), 406−412.
(165) Lin, K.; Xing, J.; Quan, L. N.; de Arquer, F. P. G.; Gong, X.; Lu, J.; Xie, L.; Zhao, W.; Zhang, D.; Yan, C.; et al. Perovskite Light-Emitting Diodes with External Quantum Efficiency Exceeding 20 Per Cent. *Nature* **2018**, *562* (7726), 245−248.
(166) Wei, F.; Deng, Z.; Sun, S.; Zhang, F.; Evans, D. M.; Kieslich, G.; Tominaka, S.; Carpenter, M. A.; Zhang, J.; Bristowe, P. D.; Cheetham, A. K. Synthesis and Properties of a Lead-Free Hybrid Double Perovskite: $(CH_3NH_3)_2AgBiBr_6$. *Chem. Mater.* **2017**, *29* (3), 1089−1094.
(167) Yuan, F.; Xi, J.; Dong, H.; Xi, K.; Zhang, W.; Ran, C.; Jiao, B.; Hou, X.; Jen, A. K. Y.; Wu, Z. All-Inorganic Hetero-Structured Cesium Tin Halide Perovskite Light-Emitting Diodes With Current Density Over 900 A cm^{-2} and Its Amplified Spontaneous Emission Behaviors. *Phys. Status Solidi RRL* **2018**, *12*, 1800090.
(168) Wang, Z.; Wang, F.; Zhao, B.; Qu, S.; Hayat, T.; Alsaedi, A.; Sui, L.; Yuan, K.; Zhang, J.; Wei, Z.; Tan, Z. A. Efficient Two-Dimensional Tin Halide Perovskite Light-Emitting Diodes via a Spacer Cation Substitution Strategy. *J. Phys. Chem. Lett.* **2020**, *11* (3), 1120−1127.
(169) Wang, A.; Guo, Y.; Zhou, Z.; Niu, X.; Wang, Y.; Muhammad, F.; Li, H.; Zhang, T.; Wang, J.; Nie, S.; Deng, Z. Aqueous Acid-Based Synthesis of Lead-Free Tin Halide Perovskites with Near-Unity Photoluminescence Quantum Efficiency. *Chem. Sci.* **2019**, *10* (17), 4573−4579.
(170) Hong, W. L.; Huang, Y. C.; Chang, C. Y.; Zhang, Z. C.; Tsai, H. R.; Chang, N. Y.; Chao, Y. C. Efficient Low-Temperature Solution-

Processed Lead-Free Perovskite Infrared Light-Emitting Diodes. *Adv. Mater.* **2016**, *28* (36), 8029−8036.
(171) Lai, M. L.; Tay, T. Y.; Sadhanala, A.; Dutton, S. E.; Li, G.; Friend, R. H.; Tan, Z. K. Tunable Near-Infrared Luminescence in Tin Halide Perovskite Devices. *J. Phys. Chem. Lett.* **2016**, *7* (14), 2653−2658.
(172) Ma, Z. Z.; Shi, Z. F.; Wang, L. T.; Zhang, F.; Wu, D.; Yang, D. W.; Chen, X.; Zhang, Y.; Shan, C.; Li, X. Water-Induced Fluorescence Enhancement of Lead-Free Cesium Bismuth Halide Quantum Dots by 130% for Stable White Light-Emitting Devices. *Nanoscale* **2020**, *12*, 3637−3645.
(173) Singh, A.; Chiu, N. C.; Boopathi, K. M.; Lu, Y. J.; Mohapatra, A.; Li, G.; Chen, Y. F.; Guo, T. F.; Chu, C. W. Lead-Free Antimony-Based Light-Emitting Diodes through the Vapor-Anion-Exchange Method. *ACS Appl. Mater. Interfaces* **2019**, *11* (38), 35088−35094.
(174) Liu, Y.; Jing, Y.; Zhao, J.; Liu, Q.; Xia, Z. Design Optimization of Lead-Free Perovskite $Cs_2AgInCl_6$:Bi Nanocrystals with 11.4% Photoluminescence Quantum Yield. *Chem. Mater.* **2019**, *31* (9), 3333−3339.
(175) Xie, J. L.; Huang, Z. Q.; Wang, B.; Chen, W. J.; Lu, W. X.; Liu, X.; Song, J. L. New Lead-Free Perovskite $Rb_7Bi_3Cl_{16}$ Nanocrystals with Blue Luminescence and Excellent Moisture-Stability. *Nanoscale* **2019**, *11* (14), 6719−6726.
(176) Fan, Q.; Biesold-McGee, G. V.; Ma, J.; Xu, Q.; Pan, S.; Peng, J.; Lin, Z. Lead-Free Halide Perovskite Nanocrystals: Crystal Structures, Synthesis, Stabilities, and Optical Properties. *Angew. Chem., Int. Ed.* **2020**, *59* (3), 1030−1046.
(177) Ghosh, S.; Pradhan, B. Lead-Free Metal Halide Perovskite Nanocrystals: Challenges, Applications, and Future Aspects. *ChemNanoMat* **2019**, *5* (3), 300−312.
(178) Yang, B.; Mao, X.; Hong, F.; Meng, W.; Tang, Y.; Xia, X.; Yang, S.; Deng, W.; Han, K. Lead-Free Direct Band Gap Double-Perovskite Nanocrystals with Bright Dual-Color Emission. *J. Am. Chem. Soc.* **2018**, *140* (49), 17001−17006.
(179) Saparov, B.; Hong, F.; Sun, J. P.; Duan, H. S.; Meng, W.; Cameron, S.; Hill, I. G.; Yan, Y.; Mitzi, D. B. Thin-Film Preparation and Characterization of $Cs_3Sb_2I_9$: A Lead-Free Layered Perovskite Semiconductor. *Chem. Mater.* **2015**, *27* (16), 5622−5632.
(180) Zhang, J.; Yang, Y.; Deng, H.; Farooq, U.; Yang, X.; Khan, J.; Tang, J.; Song, H. High Quantum Yield Blue Emission from Lead-Free Inorganic Antimony Halide Perovskite Colloidal Quantum Dots. *ACS Nano* **2017**, *11* (9), 9294−9302.
(181) Ma, Z.; Shi, Z.; Yang, D.; Zhang, F.; Li, S.; Wang, L.; Wu, D.; Zhang, Y.; Na, G.; Zhang, L.; et al. Electrically-Driven Violet Light-Emitting Devices Based on Highly Stable Lead-Free Perovskite $Cs_3Sb_2Br_9$ Quantum Dots. *ACS Energy Lett.* **2020**, *5*, 385−394.
(182) He, J.; Tritt, T. M. Advances in Thermoelectric Materials Research: Looking Back and Moving Forward. *Science* **2017**, *357* (6358), No. eaak9997.
(183) Wu, T.; Gao, P. Development of Perovskite-Type Materials for Thermoelectric Application. *Materials* **2018**, *11* (6), 999.
(184) Bell, L. E. Cooling, Heating, Generating Power, and Recovering Waste Heat with Thermoelectric Systems. *Science* **2008**, *321* (5895), 1457−1461.
(185) Dusastre, V. *Materials for Sustainable Energy: A Collection of Peer-Reviewed Research and Review Articles from Nature Publishing Group*; World Scientific: 2011.
(186) Zebarjadi, M.; Esfarjani, K.; Dresselhaus, M.; Ren, Z.; Chen, G. Perspectives on Thermoelectrics: from Fundamentals to Device Applications. *Energy Environ. Sci.* **2012**, *5* (1), 5147−5162.
(187) Stoumpos, C. C.; Malliakas, C. D.; Kanatzidis, M. G. Semiconducting Tin and Lead Iodide Perovskites with Organic Cations: Phase Transitions, High Mobilities, and Near-Infrared Photoluminescent Properties. *Inorg. Chem.* **2013**, *52* (15), 9019−9038.
(188) Mettan, X.; Pisoni, R.; Matus, P.; Pisoni, A.; Jaćimović, J. i.; Náfrádi, B.; Spina, M.; Pavuna, D.; Forró, L.; Horváth, E. Tuning of the Thermoelectric Figure of Merit of $CH_3NH_3MI_3$ (M = Pb, Sn) Photovoltaic Perovskites. *J. Phys. Chem. C* **2015**, *119* (21), 11506−11510.
(189) Zheng, L.; Li, Y.; Zhu, T.; Zhu, J.; Yi, C.; Gong, X. Enhanced Thermoelectric Performance of Doped Sn-Based Perovskite Materials. *Adv. Mater.* **2020**, submitted.
(190) Liu, Y.; Li, X.; Wang, J.; Xu, L.; Hu, B. An Extremely High Power Factor in Seebeck Effects Based on a New N-Type Copper-Based Organic/Inorganic Hybrid $C_6H_4NH_2CuBr_2I$ Film with Metal-Like Conductivity. *J. Mater. Chem. A* **2017**, *5* (26), 13834−13841.
(191) Ogomi, Y.; Morita, A.; Tsukamoto, S.; Saitho, T.; Fujikawa, N.; Shen, Q.; Toyoda, T.; Yoshino, K.; Pandey, S. S.; Ma, T.; Hayase, S. $CH_3NH_3Sn_xPb_{(1-x)}I_3$ Perovskite Solar Cells Covering up to 1060 nm. *J. Phys. Chem. Lett.* **2014**, *5* (6), 1004−1011.
(192) Liu, G.; Liu, C.; Lin, Z.; Yang, J.; Huang, Z.; Tan, L.; Chen, Y. Regulated Crystallization of Efficient and Stable Tin-based Perovskite Solar Cells via Self-sealing Polymer. *ACS Appl. Mater. Interfaces* **2020**, *12* (12), 14049−14056.
(193) Chen, Z.; Liu, M.; Li, Z.; Shi, T.; Yang, Y.; Yip, H.; Cao, Y. Stable Sn/Pb-Based Perovskite Solar Cells with a Coherent 2D/3D Interface. *iScience* **2018**, *9*, 337−346.

https://dx.doi.org/10.1021/acsami.0c02575
ACS Appl. Mater. Interfaces 2020, 12, 26776−26811